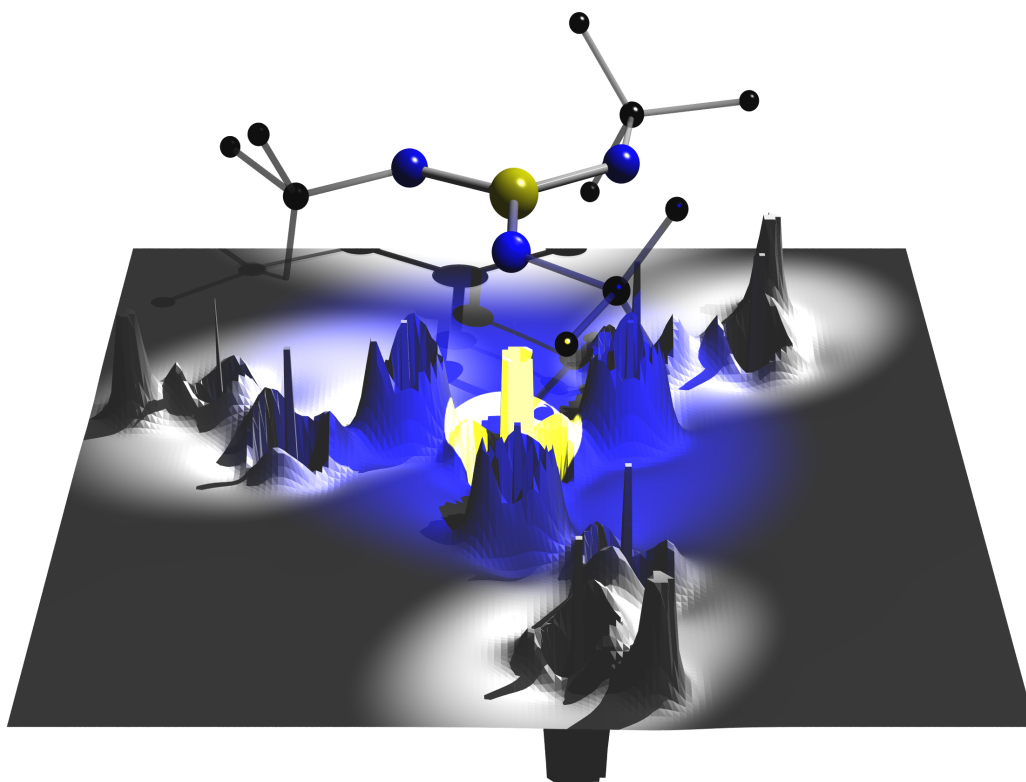


S=N versus S⁺-N⁻

An Experimental Charge Density Study

Dissertation zu Erlangung
des naturwissenschaftlichen Doktorgrades
der Bayerischen Julius-Maximilians-Universität Würzburg



vorgelegt von
Dirk Leußer
aus Würzburg

Würzburg 2002

S=N versus S⁺-N⁻
An Experimental Charge Density Study

Dissertation zur Erlangung des
naturwissenschaftlichen Doktorgrades
der Bayerischen Julius-Maximilians-Universität Würzburg

vorgelegt von
Dirk Leußner
aus Würzburg

Würzburg 2002

Eingereicht am: _____

bei der Fakultät für Chemie und Pharmazie

1. Gutachter: _____

2. Gutachter: _____

der Dissertation

1. Prüfer: _____

2. Prüfer: _____

der mündlichen Prüfung

Tag der mündlichen Prüfung: _____

Doktorurkunde ausgehändigt am: _____

für Friederike

Danksagung

Die vorliegende Arbeit wurde in der Zeit von Januar 1998 bis August 2002 im Arbeitskreis von Prof. Dr. D. Stalke am Institut für Anorganische Chemie der Universität Würzburg angefertigt.

An dieser Stelle soll allen Dank ausgesprochen werden, die zum Gelingen dieser Arbeit beigetragen haben.

Mein besonderer Dank gilt Herrn Prof. Dr. Dietmar Stalke für die interessante Themenstellung, seine stetige Diskussionsbereitschaft in ausgesprochen freundschaftlicher Atmosphäre und die Unterstützung in allen Belangen. Hervorzuheben sind hierbei die große wissenschaftliche Freiheit und die Ermöglichung einer Vielzahl von Forschungsreisen im In- und Ausland, die den Grundstock der hervorragenden Arbeitsbedingungen bildeten.

Allen gegenwärtigen und ehemaligen Arbeitskreismitgliedern danke ich für die Unterstützung und den Spaß während, als auch außerhalb der Arbeit. Namentlich danke ich:

Dr. Matthias (Babba) Pfeiffer für eine Freundschaft auf höchstem intellektuellen Niveau, die zu wiederholtem Gewinn des ChemCup, ausführlichem Studium des französischen Studienwesens, dicken Backen, fast vollen Panini-Alben und zu unglaublich peinlichen Momenten führte.

Nikolaus Kocher, der es verstand, die Pfeiffer'sche Lücke zu füllen und mit seinem Interesse und Engagement an unserem gemeinsamen Forschungsgebiet wesentlichen Beitrag zum Fortschritt der Arbeit leistete. Ganz besonders danke ich ihm für die keineswegs selbstverständliche Entlastung während meines Rückzugs vom Tagesgeschäft und das sorgfältige Korrekturlesen.

Dipl. Chem. Lutz Lameyer für seine Geduld bei meinen ersten Schritten unter Linux, die Programmierhilfe und kritische Hinterfragung der anfänglichen Ergebnisse.

Den Synthetikern unserer Gruppe, Carola Selinka, Dr. Bernhard Walfort, Thomas Stey und Dipl. Chem. Alex Murso für die spaßigen Momente im Unialltag und den beiden Erstgenannten für das Überlassen der 'perfekt unperfekten' Einkristalle, ohne die diese Arbeit nicht möglich gewesen wäre.

Dipl. Chem. Dagmar Ilge für das Überlassen ihrer theoretischen Untersuchungen, die für die nötige Sicherheit bei der Interpretation meiner Ergebnisse sorgten.

Meiner F-Praktikantin, Steffi Gräfe, für die fast schon unerträglich gute Laune, die sie in unserem Labor verbreitete, obwohl die Betreuung sicher intensiver hätte ausfallen können.

Besonderer Dank gilt Dr. Heinz Gornitzka, der dafür sorgte, dass die Aufenthalte am CNRS und Institut Paul Sabatier in Toulouse äußerst lehrreich und von hohem Unterhaltungswert waren. Die ausgiebigen Unterweisungen am SMART System und späteren Diskussionen waren unerlässlich für das Gelingen der experimentellen Arbeiten.

Den Angestellten unserer Werkstatt bin ich zu besonderem Dank verpflichtet. Die Herren Manfred Reinhart (Feinmechanik), Alois Ruf (Schlosserei) und Wolfgang Obert (Elektronik) haben mit großem Engagement für die Realisierung der Idee zum Bau einer Lufttrocknungseinrichtung für Einkristalldiffraktometer gesorgt. Hervorzuheben ist hierbei, dass sie sich keineswegs auf den Bau der Apparatur beschränkten, sondern über die gesamte Entwicklungsdauer mit Verbesserungsvorschlägen zum Fortschritt der Arbeiten beitrugen.

In diesem Zusammenhang danke ich der Hoppe AG, Laas (It), namentlich Herrn Dipl. Ing. (FH) Oliver Schuberth, für die Bereitstellung der Konstruktionssoftware und seine tatkräftige Unterstützung bei der Erstellung der Konstruktionszeichnungen.

Mein ganz herzlicher Dank gilt meiner Mutter und meinem Vater, sowie allen anderen Beteiligten aus meinem privaten Umfeld, die mir wie Theodor, Bertha, Horst und Fritz, jeder auf seine Weise, Unterstützung zuteil werden ließen.

Abschließend sei der wichtigsten Begleiterin dieser Arbeit, meiner langjährigen Freundin Friederike gedankt. Ihr ist es zu verdanken, dass auch die erfolglosen Zeiten überstanden wurden und wir trotz aller Verlockungen unsere wahren Ziele nicht aus den Augen verloren.

Contents

1 General Introduction	1
2 Construction of an Air Drying Device	9
2.1 Introduction	9
2.2 Specification and Function	11
2.3 Details of the Construction	15
2.4 Conclusion	17
3 Charge Density Study of S-N Compounds	18
3.1 Principles	18
3.1.1 Structure Refinement	19
3.1.1.1 Independent Atom Model (IAM)	20
3.1.1.2 Multipole Model	21
3.1.2 Charge Density Distributions and Topology	22
3.1.2.1 Charge Density Distributions	22
3.1.2.2 The Laplacian	23
3.1.2.3 Critical Points in the Charge Density Distribution	24
3.1.2.4 Classification of Bonds	26
3.2 Data Collection	27
3.3 Data Processing	30
3.4 Conventional (IAM) Refinements	32
3.5 Structural Comparison	36
3.6 Multipole Refinements	45
3.7 Charge Density Distributions	53

3.8 Topological Analyses	56
3.8.1 Quantification of Bond Polarisation	56
3.8.2 Critical Points in the Charge Density Distributions	57
3.8.3 Bond Orders from the Topology	71
3.8.4 The Laplacian Distributions	73
3.8.4.1 The Laplacian Distribution in I	74
3.8.4.2 The Laplacian Distribution in II	78
3.8.4.3 The Laplacian Distribution in III	81
3.8.4.4 The Laplacian Distribution in IV	84
3.8.4.5 Comparison of the Laplacian Distributions	88
3.9 Resonance Structures from the Topology	90
4 Conclusion and Prospects	97
5 Zusammenfassung	104
6 References	113

Abbreviations

ADP	anisotropic displacement parameter
AIM	atoms in molecules
at	atomic
BCP	bond critical point
BTDMTTF- TCNQ	bis(thiodimethylene)-tetrathiafulvalene tetracyanoquinodimethane
calc	calculated
CC	charge concentration
CCD	charge coupled device
CD	charge density
CP	critical point
CSD	Cambridge structural database
DFT	density functional theory
ED	electron density
eq	equation
esd	estimated standard deviation
GoF	goodness of fit
IAM	independent atom model
int	internal
iso	isotropic
IUCr	international union for crystallography
kin	kinetic
LP	lone-pair
max	maximum
Me	methyl

min	minimum
MO	molecular orbital
MSDA	mean square displacement amplitude
mul	multipole
no.	number
NRT	natural resonance theory
obs	observed
param	parameters
Ph	phenyl
pot	potential
R	residue
RCP	ring critical point
refl	reflections
res	residual
SF	scaling factor
^t Bu	<i>tert.</i> -butyl
VSCC	valence shell charge concentration

List of compounds

no.	compound		Lewis diagram
I	$S(N^tBu)_2$	sulfurdiimide	
II	$S(N^tBu)_3$	sulfurtriimide	
III	$H(N^tBu)_2SMe$	methyl(diimido) sulfonic acid	
IV	$CH_2\{S(N^tBu)_2(NH^tBu)\}_2$	methylene-bis(triimido) sulfonic acid	

1 General Introduction

For the understanding of bonding, the arrangement of entities in the solid state, and the chemical reactivity, the knowledge of the electron density distribution in the bonding and non-bonding regions is of fundamental importance. An experimental approach to evaluate the electron density is given by single crystal high-resolution X-ray diffraction at low temperatures. The development of new techniques like area detectors, automation of data collection, and fast computers to accelerate data collection on one hand, as well as low temperature devices and numerical methods for data processing to gain high-quality experimental data on the other hand, led to a breakthrough of the method in the last decade.^[1-3]

Until the 1980s for almost all groups that worked in the field of structure determination from single crystal X-ray diffraction, the method was exclusively used as an analytical tool for the identification of the atomic assembly and the determination of bond lengths and angles in routine structures.^[4,5] The restrictions on the accessibility of information from the diffraction experiments were mainly caused by the use of a simple spherical atom model,^[6] which allowed structure solution and refinement even with the limited experimental and computational resources of that time.

However, already in the 1960s and 70s Stewart^[7], Hirshfeld,^[8] and Dawson^[9] discussed the application of aspherical atom models in their pioneering works. Those principal considerations led to several complex formalisms for the description of the atomic density, like the expansion over cosini functions^[10] and the atom-centred finite multipole expansion,^[11] which were implemented in several refinement programs for the automated use in structure refinement procedures.^[12-14] All these approaches differ in the atomic models for the description of the atomic density and the features deduced from the molecular density distribution, but share a most important advantage - a flexible model, suitable to describe bonding, lone-pair density, and any kind of aspherical distribution derived directly from the modelled density.

The technique of multipole refinement on the basis of high-resolution data was excessively tested in the oxalic acid project of the IUCr.^[15] Furthermore, the suitability of modern area detectors was recently confirmed by Pinkerton *et*

*a*l.^[16] as well as by Lecomte and Howard.^[17] Since then a wide range concerning multipole refinement applications in the booming field of charge density determination was opened.

While in the beginning research focused on small organic compounds,^[18,19] and bent bonds or multiple bonding characteristics in C–C bonds on the basis of deformation density distributions were investigated,^[20] the application now is wide open to any chemical system.

Once the experimental density has been refined, it can be described by the topological analysis according to Bader's theory of 'Atoms in Molecules' (AIM).^[21] This allows direct comparison of experimental densities with quantum mechanically determined densities, which led to a raised acceptance of the theoretically verified refinement results. These topological analyses are widely used in recent density studies.^[22-24] They facilitate differentiation of bonding characteristics like shared *versus* closed shell interaction,^[25] presence or absence of multiple bonds and aromaticity,^[26] or verification of controversial bonds.^[27] Biologically active molecules like amino-acids are in the focus of attention since the determination of density related properties like the electrostatic potential^[28] and reactive surfaces^[24] allows forecasts about their biological activities. An application at the limit of the method is the use of characterised amino-acids and oligopeptides as building blocks for the aspherical refinement of proteins.^[29]

Concerning inorganic chemistry, the bonding density in transition-metal complexes is of interest,^[23,30] which allows to judge on bonding models^[31] and the calculation of net atomic charges^[32] with the corresponding formal oxidation states. In optically active materials the dipole^[33] and higher order moments,^[34,35] which can be derived from the solid state density distribution, are the key feature to understand non-linear optical effects.^[36]

It is obvious that the charge density studies from high-resolution X-ray data provide wide access to density dependent chemical and physical properties, although the method is young and the number of groups working in that area is limited. Due to the enormous potential of the method it was a major aim to establish charge density investigations in the group. It was only in late 2000 when two CCD-diffractometers were purchased and the 'Graduiertenkolleg Elektronendichte' was established in Würzburg. The preparatively working

group could supply interesting chemical problems in the sulfur-nitrogen chemistry.

Currently a major interest of our group is the full or partial replacement of the oxygen atom in sulfur oxoanions isoelectronically by $\text{NR}^{[37]}$ or CR_2 groups,^[38] respectively. Those compounds may lead to functional materials with specific applications like imid transfer reagents or oxygen sensors, since the presence of an organic substituent at the nitrogen atom gives rise to severe changes in the physical and chemical properties compared to the parent oxoanions.

The interest in sulfur-nitrogen compounds raised dramatically during the 1970s and 80s, when superconducting properties of $(\text{SN})_x$ below 0.33 K were detected.^[39] This gave a fresh impetus to SN-chemistry and led to a great variety of sulfur-nitrogen compounds.

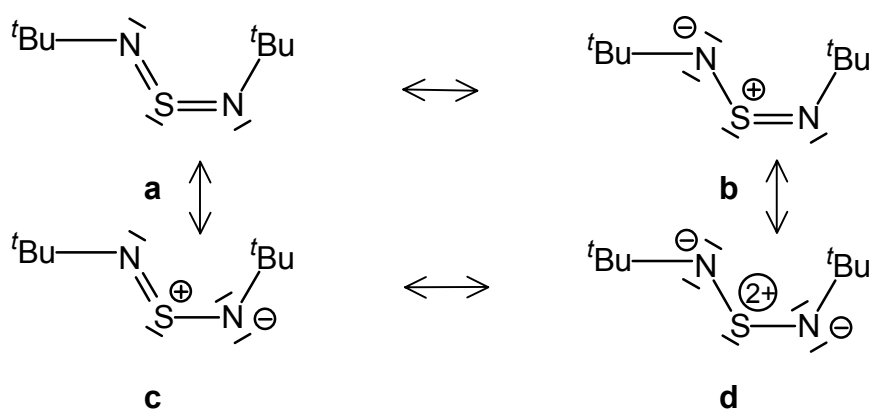
Table 1-1: Isoelectronic $\text{S-O}_x/\text{S-(NR}_x)/\text{S-(NR)}_x(\text{CR}_2)_y$ compounds. Compounds investigated in this thesis in bold letters. Highlighted compounds have not been reported previously.

S-O	S-N	mixed S-N / S-C	
SO_2	S(NR)_2	$\text{S(CR}_2)(\text{NR})$	$\text{S(CR}_2)_2$
SO_3^{2-}	S(NR)_3^{2-}	$\text{S(CR}_2)(\text{NR)}_2^{2-}$	$\text{S(CR}_2)_2(\text{NR)}_2^{2-}$
RSO_2^{2-}	RS(NR)_2^-		
R_2SO	R_2SNR		
SO_3	S(NR)_3	$\text{S(CR}_2)(\text{NR)}_2$	$\text{S(CR}_2)_2(\text{NR})$
SO_4^{2-}	S(NR)_4^{2-}	$\text{S(CR}_2)(\text{NR)}_3^{2-}$	$\text{S(CR}_2)_2(\text{NR)}_2^{2-}$
RSO_3^-	RS(NR)_3^-		
R_2SO_2	$\text{R}_2\text{S(NR)}_2$		
SO_4	S(NR)_4		
$\text{E(SO}_2)_2^{4-}$	$(\text{NR})[\text{S(NR)}_2]_2^{4-}$	$\text{E[S(NR)}_2]_2^{4-}$	
$\text{E(SO}_3)_2^{4-}$	$(\text{NR})[\text{S(NR)}_3]_2^{4-}$	$\text{E[S(NR)}_3]_2^{4-}$	

E = alkyl

Apart from investigations concerning the synthetic routes to the SNR analoga^[37,40,41] and their reactivity,^[42] our research group soon focused on the structural properties of those compounds.^[43,44]

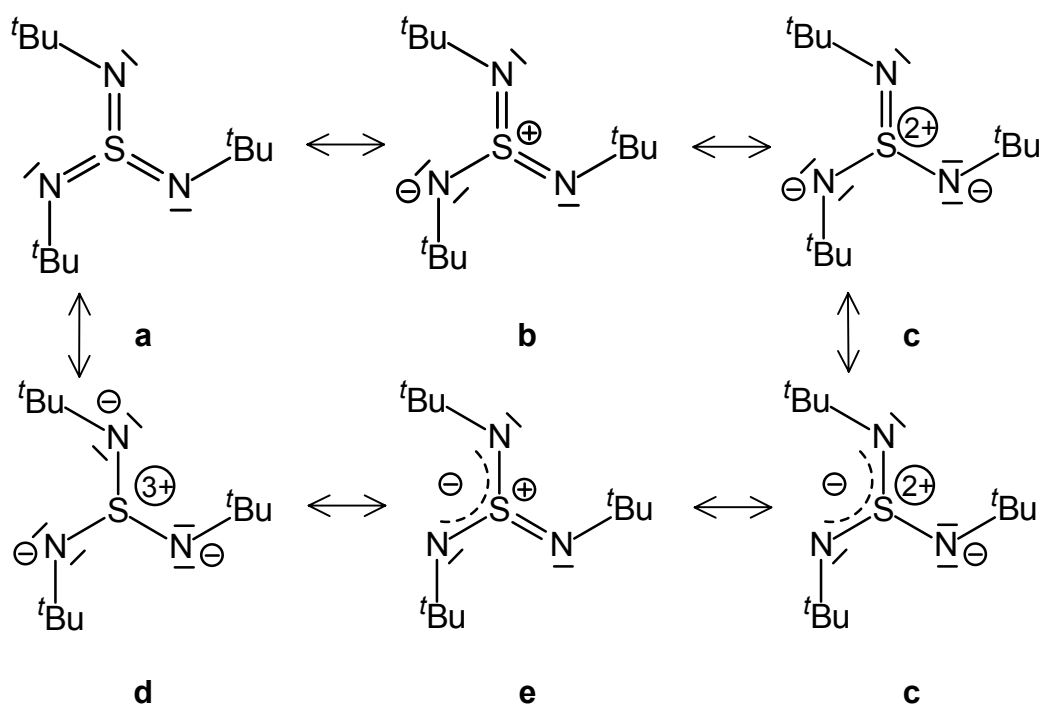
Since the landmark synthesis of the first sulfurdiimide $S(NR)_2$ 1956 by Goehring and Weis^[45] and the first sulfurtriiimide $S(NR)_3$ fourteen years later by Glemser and Wegener,^[46] the description of the bonding situation has attracted attention. These compounds are the nitrogen analogues of SO_2 and SO_3 and originally were celebrated examples of valence expansion at sulfur not following the eight-electron-rule. For both compounds several resonance structures can be formulated.



Scheme 1-1: Selection of resonance structures of $S(N^tBu)_2$ (I).

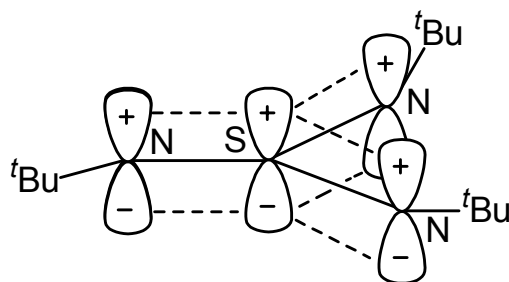
The structural characterisation of $S(N^tBu)_2$ ^[47] and $S(N^tBu)_3$ ^[48] revealed very short distances for the sulfur-nitrogen bonds of approximately 1.5 Å, which led to the formulation of S=N double bonds in those compounds.^[49]

The formulation of the resonance structures (scheme 1–1a and scheme 1–2a) avoids formal charges (Pauling's verdict), but implies valence expansion and d-orbital participation at the central sulfur atom. Theoretical investigations from the mid 80s verified, that no d-orbitals are required for the formation of those short bonds, since the energy differences between the p- and d-orbitals of the sulfur atom are much too large.^[50] Furthermore, MO-calculations on second-row atoms in 'hypervalent' molecules showed, that the d-orbitals are mainly needed as polarisation functions rather than as bonding orbitals.^[51-53]



Scheme 1-2: Selection of resonance structures of $S(N^tBu)_3$ (II).

The planarity of the SN_x units allows another bonding mode. If the nitrogen as well as the sulfur atoms were found to be sp^2 hybridised, the non-hybridised p-orbitals could be used for a delocalised π -electron system in a m-centres-n-electrons model first propagated by Rundle^[54] and later modified by Kutzelnigg.^[50a]



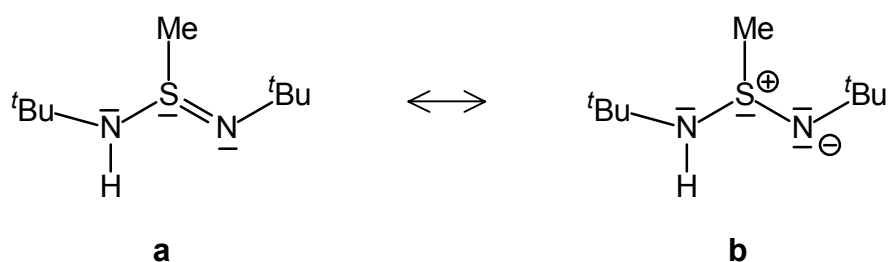
Scheme 1-3: Schematic representation of a m-centres-n-electrons model for II.

The need of an alternative bonding model became obvious as we increasingly observed a reactivity of sulfur polyimido species, which would not suite the idea of a classical $S=N$ double bond, like facile transimidation,^[37d] formation of the diimide,^[43] and $S-N$ insertion into a $M-C$ bond.^[44] All these reactions require easy $S-N$ bond cleavage. Moreover, the SN librations have to be assigned to much lower wavenumbers (640 and 920 cm^{-1}) in the Raman spectroscopic experiment than it was believed earlier (1200 cm^{-1}).^[43] These features indirectly

fuel the insight that S–N bond shortening is due to electrostatic contribution rather than to p_{π} - d_{π} double bonding. This was already clear from computational investigations, however, direct experimental evidence was lacking until now.

Since the question about bonding properties is on principle an electronic one, it can be answered best by direct investigation of the electron density distribution. Therefore the multipole refinement is the key experiment to understand the complex bonding situation. As the quality requirements lead to highly time consuming experiments and refinement procedures, a selection of sulfur-nitrogen compounds had to be identified, which allows the classification of S–N bonds for S^{IV} as well as S^{VI} containing molecules by as little as possible diffraction experiments. This was even more difficult, since almost nothing was reported in the literature about sulfur-nitrogen compounds in terms of experimental charge density investigations. The only known example based on experimental data is S_4N_4 , which was subject to topological analyses by Scherer *et al.*,^[27] while they concentrated on the description of the transannular S...S interaction rather than the density distributions in the S–N bonds. The same compound and related binary S–N rings were described in great detail by Bader,^[55] but their investigations were exclusively of theoretical nature.

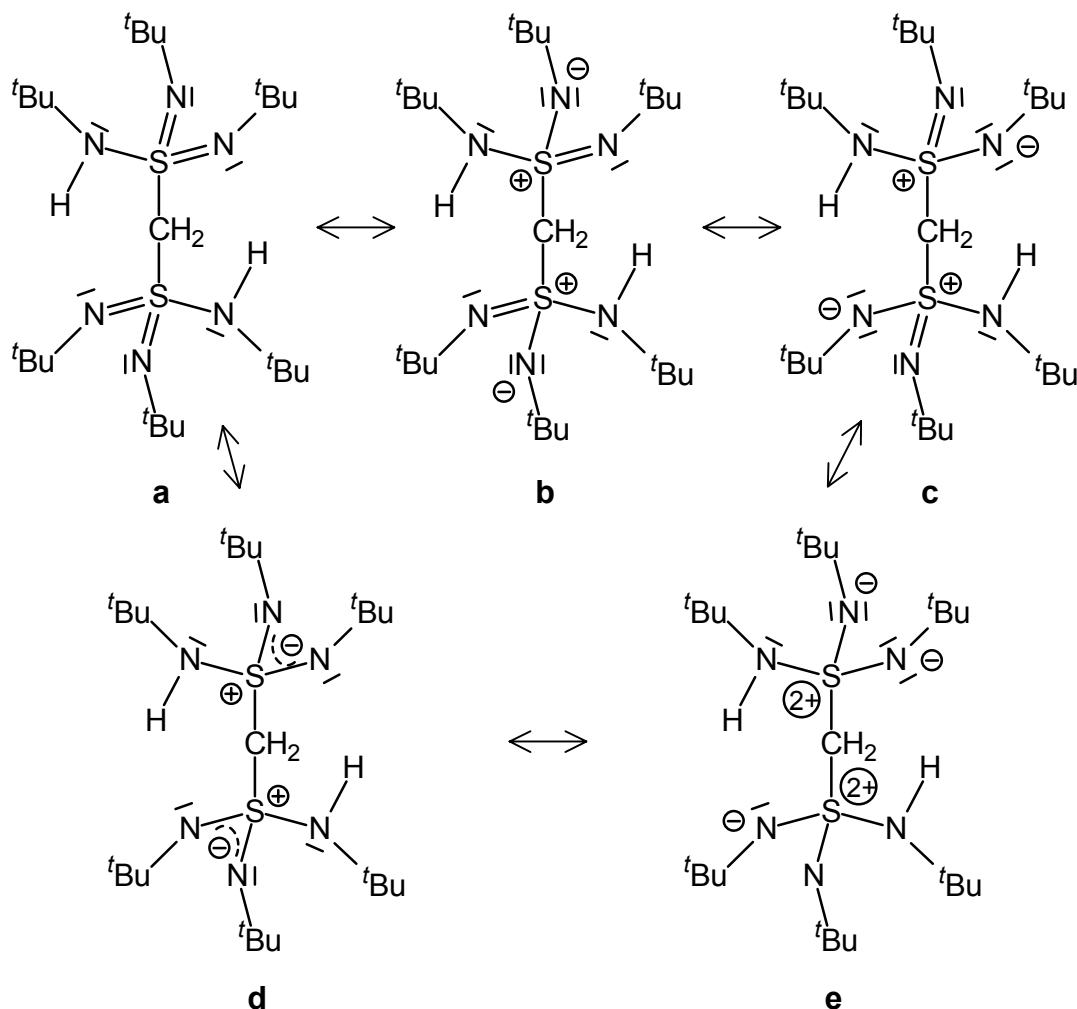
Due to the limitations mentioned above, the experiments and subsequent refinements along with the topological analysis were restricted to four compounds. Sulfurdiimide $S(N^tBu)_2$ (**I**) and sulfurtriimide $S(N^tBu)_3$ (**II**) were selected because of their fundamental importance and historical role as basis compounds. In addition $H(N^tBu)_2SMe$ (**III**), synthesised by Fleischer^[40,43] and $CH_2\{S(N^tBu)_2(HN^tBu)\}_2$ (**IV**), synthesised by Walfort,^[56] both from our group, were investigated.



Scheme 1-4: Selection of resonance structures of $H(N^tBu)_2SMe$ (**III**).

The suitability of **III** and **IV** is obvious from scheme 1–4 and scheme 1–5. Apart from formal S=N double bonds both reveal a pure S–N(H) single bond, which can serve as internal standard for the classification of SN interactions with participation of formal S^{IV} as well as S^{VI} sulfur atoms. Both compounds show

hydrogen bonds in the solid state, intermolecular in **III** and intramolecular in **IV**, respectively. Therefore it seems to be possible to cover the most relevant SN interactions with four exemplary compounds. They are important benchmark systems containing various S–N bonding modes to be revealed in the same experiment.



Scheme 1-5: Selection of resonance structures of $\text{CH}_2\{\text{S}(\text{N}^t\text{Bu})_2(\text{HN}^t\text{Bu})\}_2$ (**IV**).

Since little was known in our research group about charge density distribution from high-resolution X-ray diffraction experiments at low temperatures and even less about the technique of multipole refinement and topological analysis of the density distribution, one major aim of this thesis was to elaborate the requirements reaching from the hardware, data collection strategies, data preparation, and the electron density determination to the topological analysis. This sequence determined the structure of this thesis: the various topics are discussed as they arise in the course of the experiment. In the chapters concerning the investigations of the refined density distributions, the aim was to

reflect the historical as well as the actual progress during this thesis – refinement, discussion of geometrical parameters, calculation of density distributions such as Fourier and deformation densities, topological analysis, determination of the Laplacian distribution and finally chemical and physical conclusions based on the features discussed before. Therefore all four compounds were compared at every step, using exclusively that information which was accessible at this stage of the refinements or density analyses, respectively.

2 Construction of an Air Drying Device

2.1 Introduction

Over the last decade low temperature devices advanced as standard equipment in crystallographic laboratories world-wide. Crystal cooling devices^[57-59] at diffractometers work mainly with evaporated nitrogen^[60,61] or helium^[62] in open flow arrangements. Closed circle cryostats with liquid helium as coolant^[63] are likewise commercially available. Since the development of easy-to-handle portable devices for crystal manipulation at low temperatures,^[64] it is possible to work continuously at low temperatures from synthesis, crystallisation, crystal selection, and preparation to data collection on the diffractometer. This led to the extension of routine X-ray structure determination to thermolabile compounds,^[60] reaction intermediates,^[65,66] or even radicals,^[67] respectively.

While in the beginning crystallographers focused on the problem how to handle and transfer crystals at low temperatures to the diffractometer, the concern changed recently to difficulties with the data collection itself. The commercial low temperature devices offer the possibility to collect data of extremely good quality up to resolutions of 0.3 to 0.4 Å.^[68-70] However, the more the quality of the data is given priority one easily extends the data collection time to several days or weeks, even if a charge coupled device (CCD) detection system is used. Due to the considerable decrease of the intensities of the Bragg maxima at increasing diffraction angles,^[4] the exposure time has to be adjusted to ensure data of sufficient $I/\sigma(I)$ ratio and acceptable quality at high resolution (i. e. high diffraction angle). The longer the experiment lasts the higher is the risk of icing up the crystal and hence to vary the experimental conditions. Problems are e. g. the risk to loose the crystal by thermal damage or breakage as the snowball coating the crystal hits the collimator or detector, changes in $I/\sigma(I)$ due to ice rings in the detector image, changes in the orientation matrix and lattice dimensions due to a thermal gradient, etcetera. Consequently top priority was given to the aim to guarantee ice-free experimental conditions even over weeks. A typical experimental approach is the oil drop mounting technique.^[60] The crystal is positioned at the tip of a thin glass fibre of approximately 0.01mm in

diameter covered by an inert oil.^[71,72] Crystal and oil are then shock cooled in the open flow gas stream. Since measurements are performed in the ϕ - or ω -scan mode in thousands of steps - each of them exposed for approximately 10 to 60s at a stepwidth of typically 0.2° - the glass fibre remains very long in a nearly unchanged position. This causes icing at the glass fibre in the transition area between the cold gas stream and the outer warmer coating stream, as the humidity in the surrounding air condenses at the fibre and freezes due to turbulences.

Once an ice nucleus is formed, the icing progresses rapidly up to ice crystal sizes of several millimetres, as the laminar gas stream supplied by the cooling device is more disturbed. Those ice crystals lead to a diffraction pattern, which is superimposed on the single crystal pattern and therefore contaminates the experiment. Some progress can be made if the glass fibre is forced to rotate from time to time (typically every 10 frames), but this extends the measurement time significantly and can only postpone the problem of icing, but not avoid it.

Therefore one scope of this thesis was to find a solution for the icing problem at long measurement times. The aim was not to cure the symptoms but to find a solution to the basic problem: reduction of the high humidity around the crystal should avoid the icing.

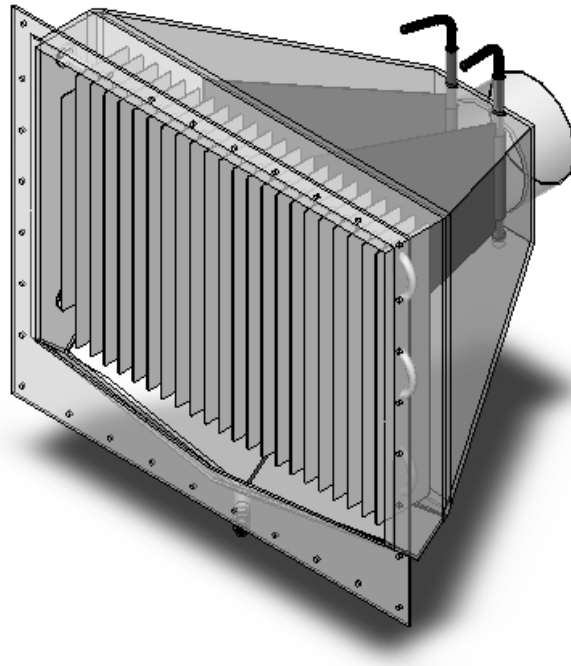


Figure 2-1: Scheme of the central unit of the cabin air drying device at the diffractometer.

As the diffractometer is covered by a lead glass / steel X-ray tight cabin, it seemed to be practicable to construct an air drying device for the diffractometer cabin. Since the gas in the cabin can not be dried like in a glove box (the cabin has to be opened occasionally to change the crystal), no continuously working system can be used. The high costs of commercially available chemically air drying systems with appreciable specifications forced us to develop a new device. The basic idea was to construct the diffractometer cabin air-tight and then to freeze out the humidity on cooling fins kept at low temperatures by a cryogenic cooling agent.

2.2 Specification and Function

The principal concept of the drying unit is to condense the humidity at a cooler. A ventilator at the outlet on the top of the cabin (**a**) delivers the air *via* the supply tubing (**b**) to the drying unit. The supply tubing is connected air-tight to the flange (**c**) of the dryer. The dryer chassis (**i**) consists of 2 mm high-grade steel, which is screwed to the cabin (**j**) and sealed with lead to protect the outside from scattered radiation. The stream of humid air can be directed by two adjustable gills (**d**), which can be positioned by Teflon[®] sealed handles (**e**), to ensure the whole cooler surface to be employed. The cooler consists mainly of 23 nickel-plated copper fins (**f**). Those fins are soldered to a copper coil (**g**), which is connected to the cooling circuit by two flanges (**h**). As cooling agent methanol is used, which can easily be kept at -78°C by a commercially available cryostat.^[73] The inlet of the cold methanol into the cooler is mechanically controlled by a valve. In use the humidity condenses on the fins and builds an ice coverage. The higher the humidity is, the sooner the fins are completely covered with a layer of ice, which blocks further air stream through the device. Then the coolant flux has to be stopped for thawing. While melting, the water is collected in the thawing groove (**k**) and removed from the chassis through the dripping valve (**l**).

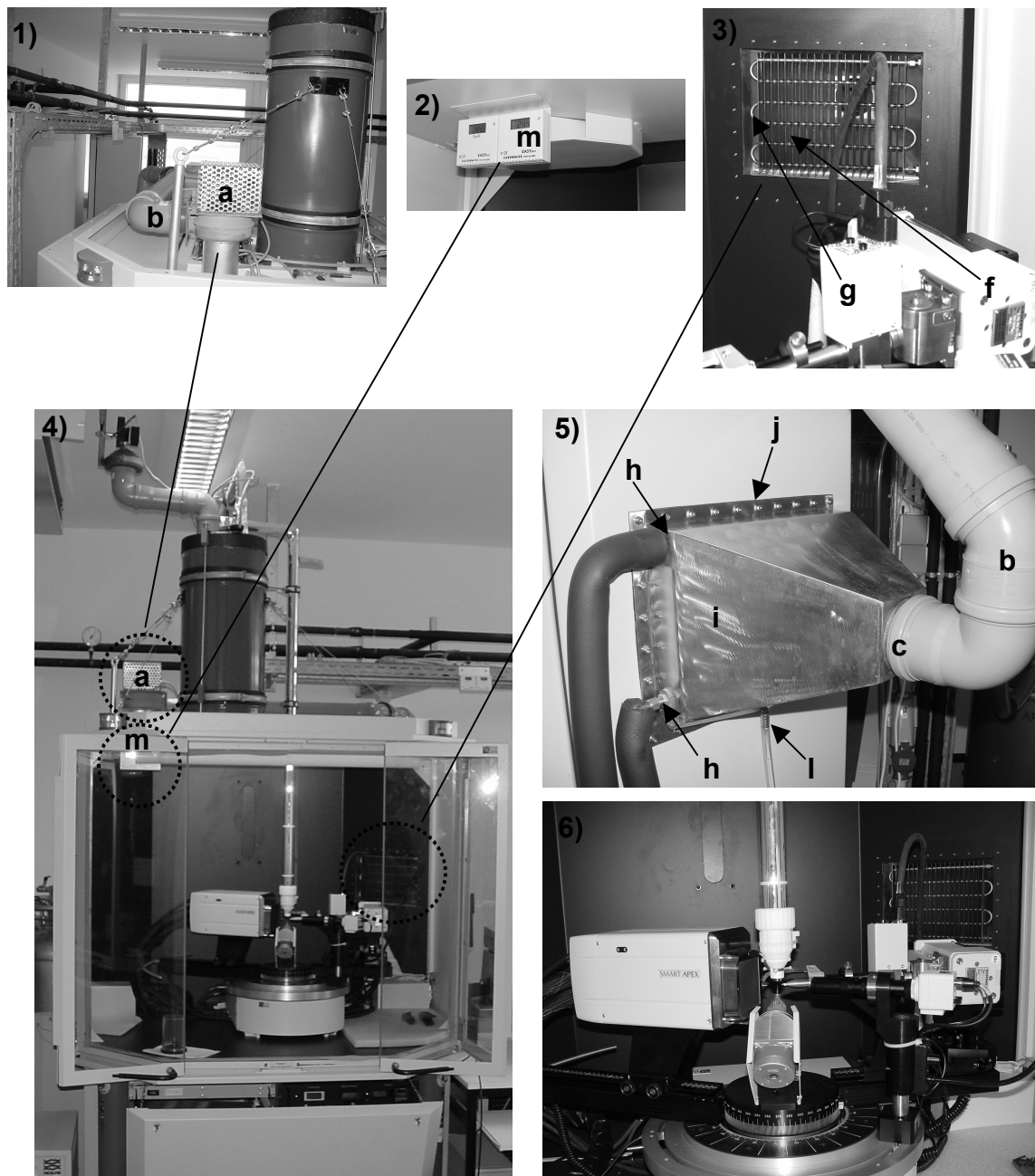


Figure 2-2: Arrangement of the air drying device at the Bruker D8 APEX diffractometer:
 1) ventilator and supply tubing; 2) sensor unit for humidity and temperature measurement; 3) coil and cooling fins; 4) diffractometer with open flow nitrogen cooling and integrated drying unit; 5) dryer chassis; 6) three-circle D8 goniometer.

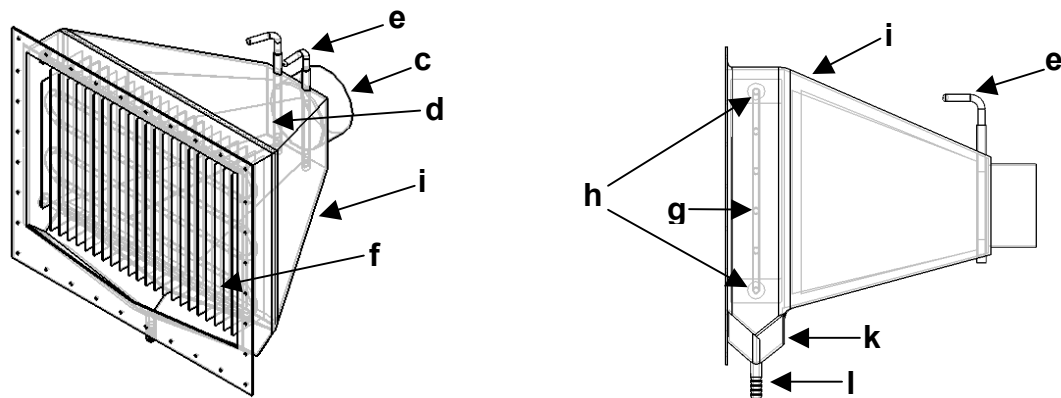


Figure 2-3: Components of the air drying device.

Since the diffractometer cabin has to be opened for changing the crystal at the goniometer, no continuously working drying device can be used. Approximately once a day the cabin has to be opened as a typical measurement for standard X-ray experiments lasts about 10 to 30 hours.

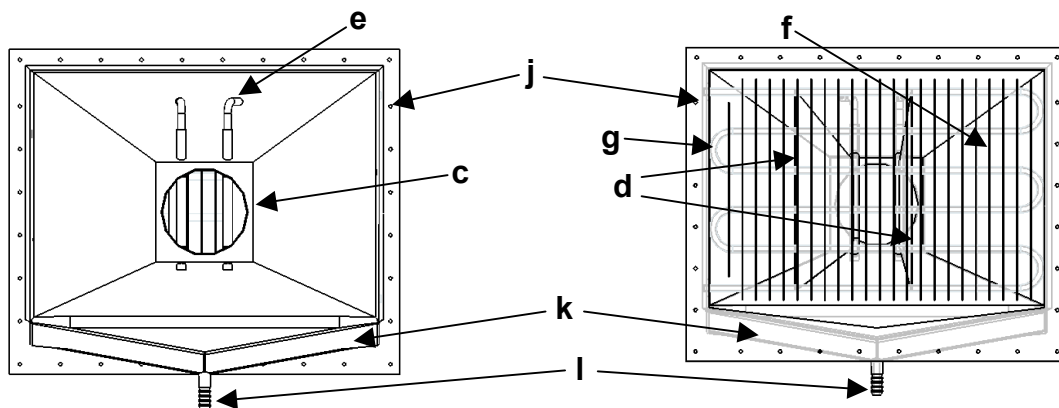


Figure 2-4: Components of the air drying device.

Therefore on one hand the device has to be regenerated quickly and without extra costs (thawing) and on the other hand it has to reach the minimum humidity as soon as possible to avoid ice nucleation at the crystal fibre.

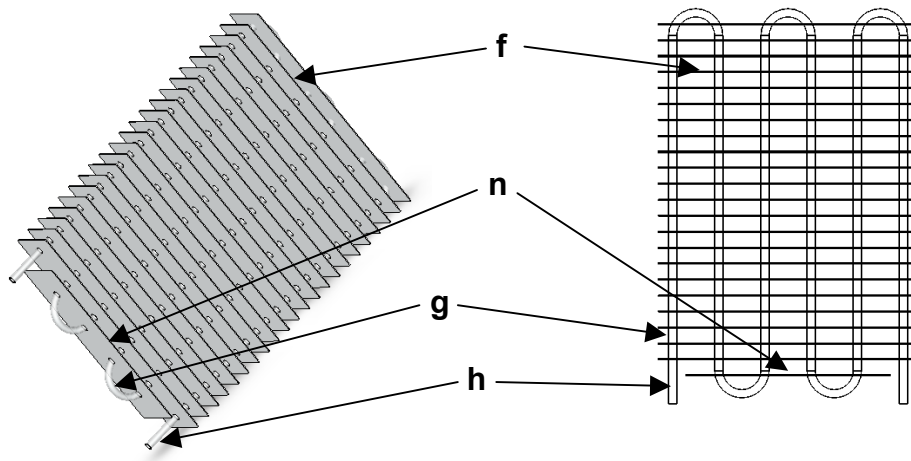


Figure 2-5: Scheme of the cooler of the drying device.

For high-resolution experiments as they were performed in this thesis, the requirements to the drying device were different. Since those experiments can last weeks, rapid drying and constant low humidity are required. For this reason the period until the drying unit is covered by ice has to be maximised, or the regeneration has to be a short time process, respectively.

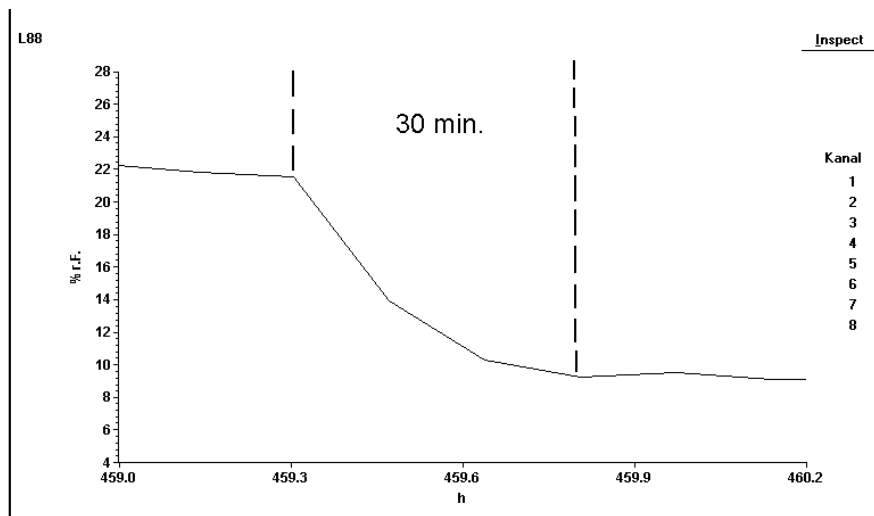


Figure 2-6: Course of the in-box humidity vs. time.

Figure 2-6 shows a typical course of the in-box humidity vs. time. The minimal humidity depends on the starting value. It was found that for standard conditions (atmospheric humidity between 10 to 60%) about 30% of the outside humidity could be reached.

2.3 Details of the Construction

All coverage parts of the air drying device are constructed from 2 mm high-grade steel due to radiation protection. This material is of the same quality as the commercially available parts for the diffractometer cabin. The device is fixed to the cabin with 32 high-grade steel bolts (M4) (j), in approximately 4 cm distance from each other. For sealing lead paper is used.

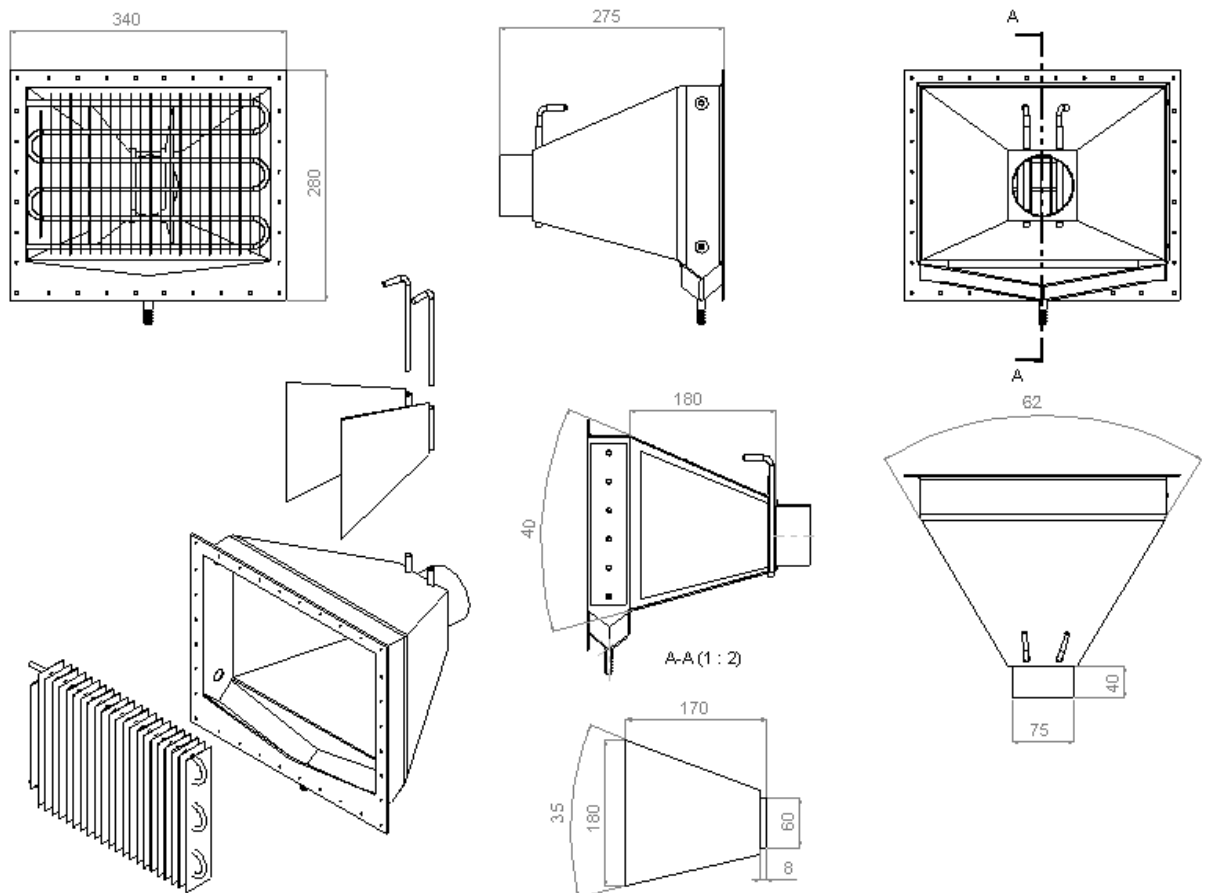


Figure 2-7: Details of the air drying device. All distances are given in mm, the angles in [°].

The coil (g) of the cooling unit is buckled from a 6 mm o. d. copper tubing (4 mm i. d.) in slopes of approximately 35 mm distance. 23 copper fins, 22 of them 45 to 197 mm (f) and one of them 45 to 155 mm in size (n) are soldered at 6 positions each to the coil and - as the coil itself - are nickel-plated to avoid corrosion.

The adjustable gills (d) to direct the air stream are stamped from a 0.75 mm steel plate. Each of them is soldered to an 8 mm steel tube, fixed to a 6 mm inner tube placed in a Teflon[®] sealed brass flange (e) outside the chassis (i). This guarantees that no condensation from outside due to cold-leakage can

occur. The inner tube allows to adjust the gills to direct the humid air stream while keeping the device closed.

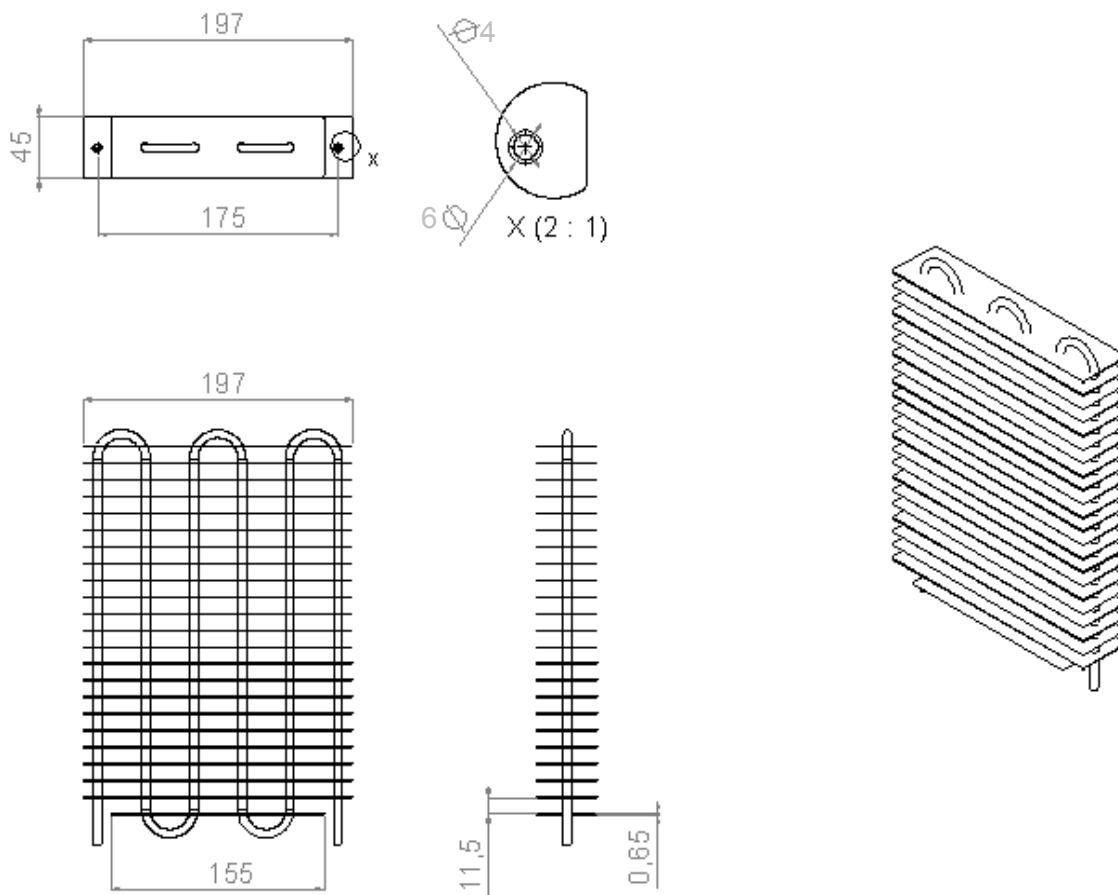


Figure 2-8: Details of the coil and cooling fins. All distances are given in mm, the angles in [°].

The original axial ventilator of the diffractometer cabin was replaced by a powerful tangential ventilator **(a)** to increase the throughput of air. The ventilator and the main drying unit **(c)** are connected air-tight by standard HT 70 polyvinylchloride tubing **(b)**.

The course of the humidity vs. time is monitored by an EASYBUS sensor unit **(m)**. The data is transmitted by a serial bus (com-port) to a computer, where the measurements are stored. For displaying the humidity measurements the data acquisition software EBS9M is used. The program package includes two functional modules, i.e. EBS9M-recorder and EBS9M-data display. A selection of graphical output by the monitoring software is presented in figure 2–9.

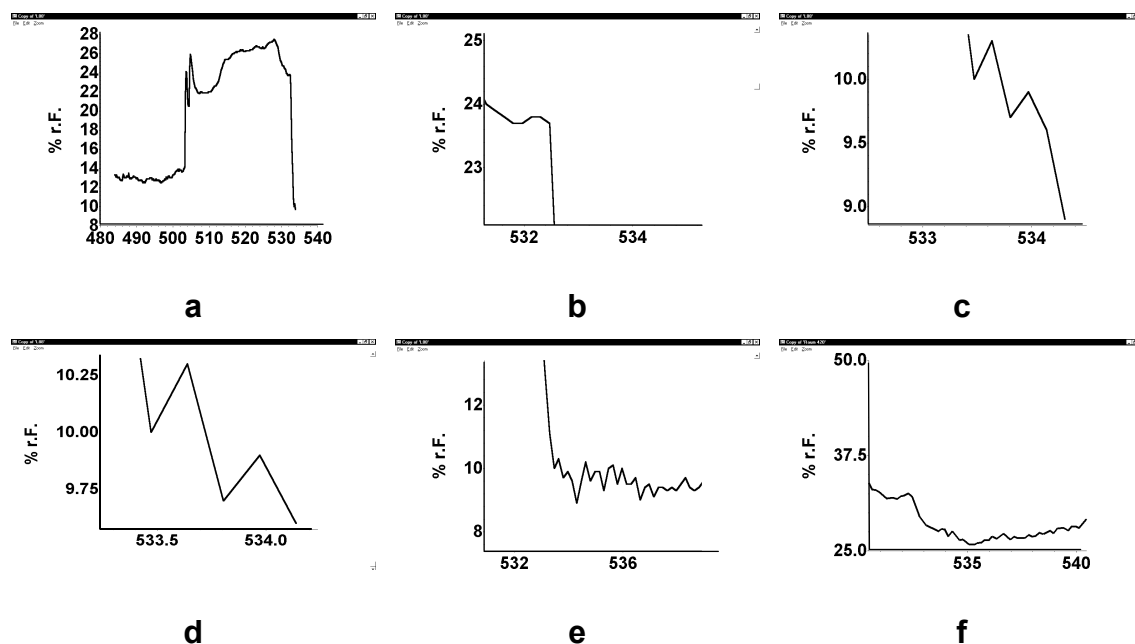


Figure 2-9: Courses of the humidity [% rel. humidity] vs. time [h]; displayed time: 2 days (**a**); course after start of the drying unit (**b**); course at the minimum value (**c**, **d**); course during the X-ray experiment (**e**); outside humidity (**f**).

From the examples given in figure 2–9 it is obvious that the drying process is quite fast. The starting value of approximately 27% relative humidity was reduced within an hour to approximately 10% and kept in an interval between 10% to 9% during the measurement.

2.4 Conclusion

The air drying device presented here is built up from easy-to-obtain material, which should be processable in every workshop associated to an university or a commercial X-ray laboratory. Compared to commercially available products, the device is a low-budget alternative at comparable specifications.

The device can be connected to every cryostat and operated with any coolant, depending only on the desired level of minimal temperature. The process of air drying and the regenerating of iced fins is quite fast and therefore prevents the crystal from icing even during long-term experiments. The developed air drying device is an easy-to-handle and affordable tool for remarkable stabilisation of experimental conditions especially during long time data collections.

3 Charge Density Study of S-N Compounds

3.1 Principles

According to the kinematical theory of scattering,^[74] the scattering amplitudes are related to the observed X-ray intensities:

$$I \sim |F(\mathbf{H})|^2, \quad (3-1)$$

where the diffraction vector \mathbf{H} is given by $\mathbf{H} = h\mathbf{a}^* + k\mathbf{b}^* + l\mathbf{c}^*$ with integral components with respect to the reciprocal axes. The structure factor itself is the Fourier transform of the static electron density distribution in the crystal given as

$$F(\mathbf{H}) = \int_V \rho(\mathbf{r}) \exp(2\pi i \mathbf{H} \mathbf{r}) d\mathbf{r}, \quad (3-2)$$

where the integration can be replaced by a Fourier summation for a three-dimensional periodic arrangement of atoms:

$$\rho(\mathbf{r}) = V^{-1} \sum_{\mathbf{H}} F(\mathbf{H}) \exp(-2\pi i \mathbf{H} \mathbf{r}). \quad (3-3)$$

$\rho(\mathbf{r})$ is also referred to as the electron density (ED) or as the electronic charge density (CD), respectively. Equation (3-3) implies the opportunity of a direct evaluation of $\rho(\mathbf{r})$ to a desired level of resolution from the experimentally received structure factors. This approach is subject to several restrictions:

Only a finite number of intensities, which are affected by experimental errors can be collected and, which is the most important limitation, the phase information is lost during detection (phase problem). These restrictions require modelling of the ED for the interpretation of the X-ray data. The parameterised models are refined by a least squares routine, which leads to an adjustment of the calculated to the measured structure factors.

Within the convolution approximation^[75] the ED is given as a sum over atomic fragments $\rho_q^{\text{at}}(\mathbf{r}_q)$ centred at \mathbf{r}_q :

$$\rho(\mathbf{r}) = \sum_q \rho_q^{\text{at}}(\mathbf{r}_q), \quad (3-4)$$

which leads *via* Fourier transformation to:

$$F(\mathbf{H}) = \sum_q f_q(\mathbf{H}) t_q(\mathbf{H}) \exp(2\pi i \mathbf{H} \mathbf{r}_q), \quad (3-5)$$

where $f_q(\mathbf{H})$ is the scattering factor and $t_q(\mathbf{H})$ denotes the temperature factor, respectively. These are the functions modified in the different diffraction models. In the harmonic approximation the thermal motion is described by a probability distribution function:

$$P_0(\mathbf{u}) = (2\pi)^{-3/2} (\det \mathbf{U})^{-1/2} \exp(-1/2 \mathbf{u}' \mathbf{U}^{-1} \mathbf{u}) \quad (3-6)$$

with the nuclear displacement vector \mathbf{u} and the mean square displacement amplitude \mathbf{U} (MSDA). Via Fourier transformation the atomic anisotropic temperature factor is given by:

$$t_0(\mathbf{H}) = \exp(-2\pi^2 \mathbf{H}' \mathbf{U} \mathbf{H}). \quad (3-7)$$

As a practicable extension of the harmonic motion model the Gram-Charlier expansion^[76] can be used for small anharmonicities. In this approach the anharmonic motion is described by an expansion in zero and higher derivatives of the normal distribution given in (3-6):

$$P(\mathbf{u}) = \left(1 + \frac{1}{3!} C_{jkl} H_{jkl} + \frac{1}{4!} C_{jklm} H_{jklm} + \dots \right) P_0, \quad (3-8)$$

where the $H_{jkl(m)}$ are the three-dimensional Hermite polynomials, which are functions of \mathbf{U} and \mathbf{u} . The expansion coefficients $C_{jkl(m)}$ denote the refined moments in the least squares procedure. Therefore the Fourier transform is reduced to a power series expansion about the temperature factor of the harmonic approximation $T_0(H)$:

$$T(H) = T_0(H) \left(1 - \frac{4}{3} \pi^3 i C_{jkl} h_j h_k h_l + \frac{2}{3} \pi^4 C_{jklm} h_j h_k h_l h_m + \dots \right). \quad (3-9)$$

3.1.1 Structure Refinement

During structure refinement on F^2 data the function $M(p_i, k)$ is minimised

$$M(p_i, k) = \sum_{\mathbf{H}} w_{\mathbf{H}} \left[k |F_{\text{obs}}(\mathbf{H})|^2 - |F_{\text{calc}}(\mathbf{H})|^2 \right]^2 = \min \quad (3-10)$$

with the refinement parameters p_i and the scaling factor k , which scales the observed amplitudes of the structure factors $F_{\text{obs}}(\mathbf{H})$ to the model related calculated structure factors $F_{\text{calc}}(\mathbf{H})$. $w_{\mathbf{H}}$ are the individual weights, which are in the case of multipole refinements selected as:

$$w_{\mathbf{H}} = 1/\sigma_{\mathbf{H}}^2 \quad (3-11)$$

with the estimated standard deviations $\sigma_{\mathbf{H}}$ of the $F_{\text{obs}}(\mathbf{H})$.

The refinements are tested to give several figures of merit, which represent the agreement of observed and calculated structure factors, respectively. Commonly used criteria are $R1$, $wR2$ and the GoF:

$$R1 = \frac{\sum_{\mathbf{H}} w_{\mathbf{H}} (|F_{\text{obs}}| - |F_{\text{calc}}|)}{\sum_{\mathbf{H}} w_{\mathbf{H}} |F_{\text{obs}}|}, \quad (3-12)$$

$$wR2 = \frac{\sum_{\mathbf{H}} w_{\mathbf{H}} (|F_{\text{obs}}|^2 - |F_{\text{calc}}|^2)^2}{\sum_{\mathbf{H}} w_{\mathbf{H}} |F_{\text{obs}}|^4}, \quad (3-13)$$

$$\text{GoF} = \sqrt{\frac{\sum_{\mathbf{H}} w_{\mathbf{H}} (|F_{\text{obs}}| - |F_{\text{calc}}|)^2}{N - n}}, \quad (3-14)$$

where N is the number of used reflections and n the number of refined parameters, respectively.

The different approaches for the structure factors lead to two atomic models used in the refinement procedures - a simple spherical independent atom model (IAM) and a more flexible multipole model.

3.1.1.1 Independent Atom Model (IAM)

Within the IAM the atomic fragments of equation (3-4) are taken as spherical atomic densities, which are in harmonic approximation thermally averaged. This description does not take into account any deformations of the ED, neither due to interactions between atoms in the bonding region nor due to lone-pair densities and therefore leads to refinement parameters biased by inadequacies in the atomic model. The ED composed like that is widely referred to as the promolecule density:

$$\rho_{\text{pro}}(\mathbf{r}) = \sum_q \rho_q^{\text{at}}(r'). \quad (3-15)$$

This approach gives the spherical scattering factor

$$f_q(\mathbf{H}) = \int_{V_q} \rho_q^{\text{at}}(r') \exp(2\pi i \mathbf{H} \mathbf{r}') dV_q, \quad (3-16)$$

which is calculated by integration over the atomic volume V_q of the q^{th} fragment and tabulated in the *International Tables for Crystallography*.^[76]

The model parameters of the IAM are:

- 3 fractional coordinates x, y, z
- and
- 6 anisotropic displacement parameters U_{ij} for the non-hydrogen atoms
- or
- 1 isotropic displacement parameter U_{iso} for the hydrogen atoms, respectively.

The mentioned shortcomings in the IAM can at least partially be overcome by the exclusive use of the high-order reflections during the refinement procedure. The concentrated atomic core densities contribute most to the reflections at high Bragg angles, where the participation of the more diffuse bonding densities is less important. With application of high-order refinement (i. e. $\sin\theta/\lambda \geq 1.0 \text{ \AA}^{-1}$), the promolecule density is a useful approximation leading to model parameters, which are in good agreement with the values found by other methods e.g. neutron diffraction.^[77,78]

3.1.1.2 Multipole Model

Further progress in accuracy of the refined parameters is made by implementing an aspherical model for the description of the atomic densities. A widely applied formalism in this respect is the nucleus centred finite multipole expansion, first developed by Stewart^[7] and modified by Hansen and Coppens.^[11] This atom model is implemented in the program package XD,^[14] which was used in this thesis. Within this formalism the atomic ED is formulated as sum over three components:

$$\rho_q^{\text{at}}(\mathbf{r}) = \rho_c(r) + P_v \rho_v(\kappa r) + \rho_d(\kappa' \mathbf{r}), \quad (3-17)$$

where ρ_c and ρ_v denote the spherical core and spherical valence densities, respectively. The deformation density term ρ_d is given by:

$$\rho_d(\kappa' \mathbf{r}) = \sum_l R_l(\kappa' r) \sum_{m=-l}^l P_{lm} Y_{lm}(\mathbf{r}/r). \quad (3-18)$$

The radial functions R_l are of the Slater type:

$$R_l(r) = \frac{\alpha_l^{n(l)+3}}{(n(l)+2)!} r^{n(l)} \exp(-\alpha_l r) \quad (3-19)$$

with $n(l) > l$ to obey Poisson's equation^[79] and α_l calculated from single-zeta wave functions. The angular dependence is given by the Y_{lm} term, which describes the density normalised real spherical harmonics:

$$\int_{\phi=0}^{2\pi} \int_{\theta=0}^{\pi} |Y_{lm}| d\Omega = 2 \text{ for } l > 0 \quad (3-20)$$

$$= 1 \text{ for } l = 0.$$

Integration is performed over the solid angle $d\Omega = \sin\theta d\theta d\phi$.

In addition to the standard positional and thermal parameters, the radial contraction/expansion parameters κ and κ' , the populations P_v (spherical valence density), and P_{lm} (aspherical deformation density) are refined in the multipole model. Following the multipole expansion, the corresponding atomic form factor is given by

$$f_q(\mathbf{H}) = f_c(H) + P_v f_v(H/\kappa) + \sum_l \langle J(H/\kappa') \rangle_l \sum_{m=-l}^l P_{lm} Y_{lm}(\mathbf{H}/H), \quad (3-21)$$

where $\langle J \rangle$ is the l^{th} order Fourier-Bessel transform of R_l .

The multipole model is a highly flexible attempt to describe atomic densities, which are deformed due to bonding or existence of non-bonding densities (lone-pairs). For each non-hydrogen atom - hydrogen atoms have to be handled with special care - the formalism allows to refine up to 25 population parameters and two contraction/expansion parameters for the description of the valence densities. This makes the multipole refinement a powerful tool for the experimental determination of atomic and molecular charge density distributions.

3.1.2 Charge Density Distributions and Topology

Once the ED distribution has been determined, several chemical and physical properties can be calculated. Besides $\rho(\mathbf{r})$ itself, first and higher order derivatives can be used to evaluate density related functions.

3.1.2.1 Charge Density Distributions

While the total ED holds information about the spatial distribution of atoms, the so called deformation densities are used to visualise valence density effects. In

principle there are two options to depict the density in Fourier or direct space representation. All Fourier densities are calculated by summing over differences in observed and calculated structure factors and differ only in assignment of model phases to the $F(\mathbf{H})$. All of them are model dependent and affected by errors due to finite summation. Therefore in this thesis exclusively the residual Fourier density is used:

$$\delta\rho_{\text{res}}(\mathbf{r}) = \frac{1}{V} \sum_{\mathbf{H}} [|F_{\text{obs}}(\mathbf{H})| - |F_{\text{calc,mul}}(\mathbf{H})|] \exp(i\Phi_{\text{mul}}) \exp(-2\pi i\mathbf{Hr}), \quad (3-22)$$

where $F_{\text{calc,mul}}(\mathbf{H})$ are the structure factors and Φ_{mul} the phases from the multipole model, respectively. This density distribution has to result in flat, featureless maps for good data and successful description of all densities by the model. For this reason the residual density is used as an important figure of merit to check the quality of the refinement.

To visualise the bonding densities, the static deformation density is widely used:

$$\Delta\rho_{\text{static}}(\mathbf{r}) = \rho(\mathbf{r}) - \sum_q \rho_q^{\text{at}}(\mathbf{r}), \quad (3-23)$$

where the reference density $\rho_q^{\text{at}}(\mathbf{r})$ is often chosen as the promolecule density, defined in equation (3-15). In contrast to the Fourier densities, the static deformation density is a direct space property on 'infinite resolution', which is deconvoluted from thermal smearing due to its direct calculation from the refined model parameters and leads therefore to density maps, that show in most cases very well defined densities in the bonding and lone-pair regions. Nevertheless, due to the model dependency, which stems from the preconceptions of the promolecule, density maps calculated in that way have to be inspected with special care. Static deformation densities may not show all expected features if atoms with a degenerate ground state are involved.^[80] This limitation can be overcome by calculating density related properties directly from the model density, without the use of any reference state, following Bader's theory of 'Atoms in Molecules' (AIM).^[21]

3.1.2.2 The Laplacian

The Laplacian of $\rho(\mathbf{r})$, defined as the trace of the Hessian matrix:

$$\nabla^2\rho(\mathbf{r}) = \frac{\partial^2\rho}{\partial x^2} + \frac{\partial^2\rho}{\partial y^2} + \frac{\partial^2\rho}{\partial z^2} \quad (3-24)$$

represents charge concentrations where it is negative and charge depletions relative to the mean value where it is positive, respectively. Due to its calculation from the second derivative of the ED, small changes in $\rho(\mathbf{r})$ are very much emphasised in the spatial distribution of the Laplacian and it is therefore a very sensitive tool to visualise the shell structure of atoms and preferred orientations within the valence shell, resulting from bonding or non-bonding charge concentrations.

$\nabla^2\rho(\mathbf{r})$ is related to the electronic energy density $E(\mathbf{r})$, which is defined as

$$E(\mathbf{r}) = G(\mathbf{r}) + V(\mathbf{r}) \quad (3-25)$$

with the potential energy $V(\mathbf{r})$ and the kinetic energy density $G(\mathbf{r})$, respectively, by

$$-L(\mathbf{r}) \equiv \left(\frac{\hbar^2}{4m}\right)\nabla^2\rho(\mathbf{r}) = 2G(\mathbf{r}) + V(\mathbf{r}). \quad (3-26)$$

The Laplacian as a property of the electronic charge density can therefore be related to the local components of the total energy.^[21] Together with the virial theorem

$$2 E_{\text{kin}} = - E_{\text{pot}}, \quad (3-27)$$

the sign of the Laplacian is an indicator whether the kinetic or potential energy dominates the local contribution to the virial theorem. If $L(\mathbf{r})$ is positive (negative Laplacian) the potential energy dominates, while with negative $L(\mathbf{r})$ the kinetic energy dominates. The sign of the Laplacian can therefore lead to criteria for bond classification, as in the internuclear regions of shared interactions (covalent bonds) density accumulations ($\nabla^2\rho(\mathbf{r}) < 0$) are expected, while for closed shell interactions (ionic bonds) relative depletion occurs ($\nabla^2\rho(\mathbf{r}) > 0$).

3.1.2.3 Critical Points in the Charge Density Distribution

Following Bader's concept, the molecular structure (atomic positions, bonding, etc.) can be extracted from a topological analysis of $\rho(\mathbf{r})$. Of great importance in that context are the points in space, where the first derivative of the ED equals zero - the critical points (CPs):

$$\nabla\rho(\mathbf{r}_c) = \mathbf{i}\frac{\partial\rho}{\partial x} + \mathbf{j}\frac{\partial\rho}{\partial y} + \mathbf{k}\frac{\partial\rho}{\partial z} = 0, \quad (3-28)$$

where \mathbf{i} , \mathbf{j} , \mathbf{k} are the unit vectors in the Cartesian frame. To classify those CPs and to verify whether they assign a local maximum, minimum, or a saddle point in the ED distribution, the second derivatives at the CPs have to be determined.

The Hessian matrix $\mathbf{H}(\mathbf{r})$ is defined as the symmetric matrix of the nine second order derivatives of $\rho(\mathbf{r})$. At the critical point \mathbf{r}_c this leads to:

$$\mathbf{H}(\mathbf{r}_c) = \left(\begin{array}{ccc} \frac{\partial^2 \rho}{\partial x^2} & \frac{\partial^2 \rho}{\partial x \partial y} & \frac{\partial^2 \rho}{\partial x \partial z} \\ \frac{\partial^2 \rho}{\partial y \partial x} & \frac{\partial^2 \rho}{\partial y^2} & \frac{\partial^2 \rho}{\partial y \partial z} \\ \frac{\partial^2 \rho}{\partial z \partial x} & \frac{\partial^2 \rho}{\partial z \partial y} & \frac{\partial^2 \rho}{\partial z^2} \end{array} \right)_{\mathbf{r}=\mathbf{r}_c} \quad (3-29)$$

After diagonalisation of the Hessian matrix, the type of a (m,n) CP can be determined from the eigenvalues λ_i , the principal axes of the curvature at \mathbf{r}_c :

$$\mathbf{D}(\mathbf{r}_c) = \left(\begin{array}{ccc} \frac{\partial^2 \rho}{\partial x^2} & 0 & 0 \\ 0 & \frac{\partial^2 \rho}{\partial y^2} & 0 \\ 0 & 0 & \frac{\partial^2 \rho}{\partial z^2} \end{array} \right)_{\mathbf{r}=\mathbf{r}_c} = \left(\begin{array}{ccc} \lambda_1 & 0 & 0 \\ 0 & \lambda_2 & 0 \\ 0 & 0 & \lambda_3 \end{array} \right) \quad (3-30)$$

Characterisation of the CP is carried out *via* m and n :

m : number of non-zero eigenvalues λ_i (rank of $\mathbf{D}(\mathbf{r}_c)$)

n : algebraic sum of the signs of the eigenvalues (signature of $\mathbf{D}(\mathbf{r}_c)$).

In three-dimensional space four possible types of CPs in $\rho(\mathbf{r})$ can be deduced:

(3,-3): all $\lambda_i < 0$; $\rho(\mathbf{r}_c)$ is a local maximum. (3,-3) CPs are found at the atomic positions.

(3,-1): two $\lambda_i < 0$; $\rho(\mathbf{r}_c)$ is a maximum in the plane defined by these axes and a minimum along the third axis (saddle point). (3,-1) CPs are characteristic for chemical bonds and referred to as bond critical points (BCPs).

(3,+1): two $\lambda_i > 0$; $\rho(\mathbf{r}_c)$ is a minimum in the plane defined by these axes and a maximum along the third axis. (3,+1) CPs are found in the centre of rings of connected atoms and referred to as ring critical points (RCPs).

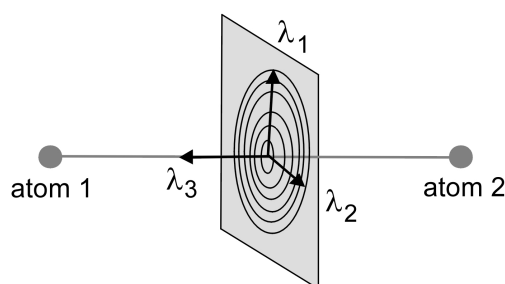
(3,+3): all $\lambda_i > 0$; $\rho(\mathbf{r}_c)$ is a local minimum.

Besides the topological properties of $\rho(\mathbf{r})$, the existence of CPs in the Laplacian is of interest, as (3,-3) CPs in $-\nabla^2 \rho(\mathbf{r})$ indicate non-bonding charge concentrations (lone-pairs).^[55] Such a search in the spatial distribution of the

Laplacian is not straightforward, as the function $\nabla^2\rho(\mathbf{r})$ changes rapidly and therefore the numerical algorithms have to be very sensitive. Apart from the oxalic acid project^[15] of the IUCr only few examples are known for experimentally derived CPs in the Laplacian for characterisation of an atomic state.^[23,56,81]

3.1.2.4 Classification of Bonds

The existence of a (3,-1) CP in $\rho(\mathbf{r})$ is an essential requirement for the formulation of a bond. $\rho(\mathbf{r}_c)$, the Laplacian, and the values of the λ_i at this BCP facilitate the characterisation of atomic interaction.



Scheme 3-1: Spatial orientation of the eigenvalues λ_i .

Besides these topological parameters, the position of the BCP contains additional information, as it indicates bending or polarisation effects, respectively.

(i) shared interactions: $\nabla^2\rho(\mathbf{r}) < 0$; the charge density is contracted along the bond path, which leads to a negative Laplacian and increased $\rho(\mathbf{r}_c)$, respectively.

(ii) closed shell interactions: $\nabla^2\rho(\mathbf{r}) > 0$; internuclear depletion of the charge density and accumulation in the regions of the valence densities are observed, which leads to a positive Laplacian (positive eigenvalue λ_3 dominates) and low values of $\rho(\mathbf{r}_c)$ at the BCP, respectively.

(iii) bond order: the bond order is related to the amount of charge density at the BCP. For a specific bond type the bond order n can be calculated from

$$n = \exp[A(\rho(\mathbf{r}_c) - B)], \quad (3-31)$$

where A and B have to be adjusted empirically by values determined from bonds of known bond order.

(iv) ratio $|\lambda_1|/\lambda_3$: while λ_1 is the largest contraction of density perpendicular to the bond path and λ_3 denotes the concentration parallel to the bond towards the

nuclei, respectively, the ratio $|\lambda_1/\lambda_3|$ is < 1 for closed shell interactions. It increases with bond strength and decreases with ionic contribution in shared interactions.

(v) ellipticity: $\varepsilon = \lambda_1/\lambda_2 - 1$; the ellipticity at the BCP quantifies the deviation from rotational symmetry for a given bond density distribution. For pure σ -bonding ε equals zero, while π -contribution in double bonds leads to ellipticities > 0 .

It has to be pointed out that the above mentioned criteria are not always strictly decisive. They are tested for first-row elements excessively,^[82] but it is well documented that for second-row or heavier elements several exceptions are observed. Polar covalent bonds (e.g. Si–O in silicates) reveal a positive Laplacian at the BCP as the positive eigenvalue λ_3 dominates there.^[83,84] The values of ellipticities, which indicate multiple bonding can only be compared for bonds between specific elements. Therefore none of the topological criteria should be judged on his own nor on an absolute scale.

3.2 Data Collection

All compounds discussed in this thesis were measured at the same temperature (100 K) on a Bruker Apex-CCD diffractometer, equipped with a D8 three-circle goniometer, using comparable strategies for the data collection. Since in our group no experience in the collection of high-resolution X-ray data existed, the development of a practicable strategy for the experimental proceeding had top priority. Therefore a compromise between the requirement of outstanding quality of the data needed for multipole refinements and the limited measurement time had to be found. The use of an empirical absorption correction, which is discussed in detail later, requires high redundancy of the data. As a limit an average redundancy of three is demanded for standard experiments,^[85] which should be raised considerably if multipole refinement is attempted.

Since our interest lies in the modelling of diffuse bonding densities, special care has to be taken on the collection of the data at low Bragg angle, as there the relative contribution caused by the diffuse densities is appreciable high. Therefore redundancies of at least ten are demanded for monoclinic or higher symmetry and five in the case of triclinic lattices.

For the high-order data this is not practicable, as the exposure time at high-angles can easily reach ten times the value at low-angles. For high-order data long exposure times are necessary, since the intensity decreases remarkably with increasing diffraction angle.^[4] Nevertheless, high quality of the high-order data is needed, because these reflections comprise information about the core densities and can therefore lead to reliable atomic coordinates and thermal parameters, which are an essential requirement for successful multipole refinements. To fulfil these high demands a redundancy of at least five for the high-order data was endeavoured.

Table 3-1: Conversion table for widely used physical quantities for the description of experimental resolution in diffraction experiments with MoK $_{\alpha}$ radiation.

$\sin\theta/\lambda$ [\AA^{-1}]	0.50	0.54	0.80	0.90	1.00	1.08	1.11	1.14
d [\AA]	1.0	0.93	0.63	0.56	0.50	0.46	0.45	0.44
2θ [$^{\circ}$]	41.63	55.00	69.30	79.53	90.59	100.00	104.17	108.24

Assuming a detector-to-sample distance of 5 cm, the detection cone-angle of the CCD is approximately 55° in 2θ if MoK $_{\alpha}$ radiation is used. This leads to at least two different detector positions if a data collection up to a resolution of $\sin\theta/\lambda \geq 1.0 \text{ \AA}^{-1}$ is attempted, as it is recommended for subsequent multipole refinement.^[1] Therefore two principally different ways of data collection are practicable:

A first possibility consists in the collection of independent data sets at different 2θ -positions, with as much overlap in the detection cone-angle of the CCD as possible, to detect identical reflections in all batches. During integration these data batches are scaled together. The scaling procedure is based on the comparison of the multiple measured identical reflections of the individual batches. The combined data are handled as one data set in further steps of processing and refinement. This strategy leads to at least three batches: a low-angle, a mid-angle and a high-angle batch, respectively, to fulfil the requirements concerning the resolution limit and the desired maximised overlap.

Besides the problem of measurement time, the empirical absorption correction is crucial if data of a wide 2θ -range is used. Since this correction roots in one function used for all intensities, no 2θ -dependent effects are included.

Therefore the data collected for this thesis were handled in a different manner. Two independent batches were collected, a low-angle ($2\theta_{\text{detector}} = -31^{\circ}$) and a

high-angle batch ($2\theta_{\text{detector}} = -80^\circ$), respectively. Both data sets were assigned an individual scaling factor and were treated independently during all steps of data processing. The small overlap region was not employed to scale both batches. This strategy allows a maximum resolution limit of up to $\sin\theta/\lambda = 1.14 \text{ \AA}^{-1}$ from only two batches of data. In table 3–2 the different data collections for compounds **I-IV** are compared.

Table 3-2: Crystallographic data of the data collections of compounds **I-IV**. All data collections were performed at a measurement temperature of 100 K with MoK_α radiation (0.71073 Å) and a detector-to-sample-distance of 5.0 cm. All reflections were collected in the ω -scan mode with detector positions of -31.0° for the low-angle and -80.0° for the high-angle batch, respectively.

compound	I	II	III	IV
identification code	diimid	stern	sulfin	sulfon
formula	$\text{S}(\text{N}^t\text{Bu})_2$	$\text{S}(\text{N}^t\text{Bu})_3$	$\text{H}(\text{N}^t\text{Bu})_2\text{SMe}$	$\text{CH}_2\{\text{S}(\text{N}^t\text{Bu})_2(\text{NH}^t\text{Bu})\}_2$
crystal size [mm]	0.40x0.40x0.40	0.48x0.45x0.30	0.35x0.30x0.25	0.28x0.18x0.17
φ -positions (low-angle) [°]	0, 45, 90, 135, 180, 225, 270, 315	0, 45, 90, 135, 180, 225, 270, 315	0, 45, 90, 135, 180, 225, 270, 315, (2 times each)	0, 45, 90, 135, 180, 225, 270, (2 times each), 315
no. frames per run / $\Delta\omega$ [°] / time [s]	901 / -0.2 / 4	901 / -0.2 / 4	901 / -0.2 / 5	906 / -0.2 / 15
φ -positions (high-angle) [°]	45, 90, 135, 180, 225, 270, 315	0, 45, 90, 135, 180, 225, 270, 315	0, 45, 90, 135, 180, 225	0, 45, 90, 135, 180, 225, 270, 315
no. frames per run / $\Delta\omega$ [°] / exposure time [s]	901 / -0.2 / 40	901 / -0.2 / 90	901 / -0.2 / 90	606 / -0.3 / 200
$\sin\theta/\lambda_{\text{max}}$ [Å ⁻¹]	1.11	1.14	1.14	1.14
reflections collected (low-angle batch)	12299	17996	54868	136761
R_{int} (low-angle)	0.0546	0.0324	0.0605	0.0482
reflections collected (high-angle batch)	25532	44864	42875	225974
R_{int} (high-angle)	0.0666	0.0346	0.0308	0.0677

3.3 Data Processing

Like during data collection, all compounds were treated equally in the subsequent data processing.

In a first step the intensities were integrated with the program SAINT,^[86] using the 3d-profiling method described by Kabsch.^[87] For the integration a starting orientation matrix had to be determined within the program SMART,^[88] which was also used for controlling the diffractometer during data collection. For each run a specific matrix has been determined, thresholding reflections with $I > 20\sigma(I)$ from a subset of 200 frames. Using these matrices, the low- and high-angle batches were integrated separately. During the integration routine, the matrices were automatically adjusted every 100 frames. The box sizes for the spot integration were determined from a least squares fit, which based on the first 100 frames of each run.

After this first integration step a mean matrix and the corresponding mean unit cell were determined by the program as well as a symmetry constrained unit cell, which was assigned meaningful estimated standard deviations (esds). This constrained unit cell, which was calculated from the low-angle reflections was used during all subsequent structure refinements.

Then the refined box sizes were compared and a mean integration box was calculated from these least squares values. Together with the mean matrix calculated by the integration software, this mean box was used to perform a second integration, where the box size and matrix refinement routines were suppressed. This procedure was necessary, since it guarantees that the direction cosine of all reflections in one batch base on the same matrix information. This is essentially for a successful absorption correction, where this information concerning the diffraction lattice planes is used.

After integration of the intensities the raw data of all compounds were processed in the same manner. In a first step intensity statistics were checked and the high-angle batches were cut at a high-resolution limit if the data quality decreased remarkably (only necessary for compound **IV**).^[89] The low-angle batches were cut at $\sin\theta/\lambda_{\max} = 0.625 \text{ \AA}^{-1}$, which was used as low-resolution limit for the high-angle batches, anyway. This procedure guarantees that no overlap in the batches occurs.

Table 3-3: Crystallographic data of the data processing of compounds I-IV.

compound	I	II	III	IV
formula	S(N ^t Bu) ₂	S(N ^t Bu) ₃	H(N ^t Bu) ₂ SMe	CH ₂ {S(N ^t Bu) ₂ (NH ^t Bu)} ₂
crystal system	triclinic	triclinic	monoclinic	monoclinic
space group	P $\bar{1}$	P $\bar{1}$	P 2 ₁ /c	C 2/c
a [Å]	5.9699(4)	9.3228(3)	8.8832(3)	29.8239(8)
b [Å]	9.2877(4)	9.3455(3)	14.7504(5)	11.4206(3)
c [Å]	9.9338(4)	10.6675(3)	9.3656(3)	18.0801(4)
α [°]	72.505(1)	70.515(1)	90	90
β [°]	88.338(1)	77.571(1)	110.851(1)	91.041(1)
γ [°]	84.661(1)	60.554(1)	90	90
V [Å ³], Z	523.04(7), 2	761.52(7), 2	1146.81(11), 4	6157.18(47), 8
no. of refl. for the unit cell determination	8646	7829	7321	9210
2 θ -range [°] for the unit cell determination	4.6 < 2 θ < 52.9	5.0 < 2 θ < 52.8	4.9 < 2 θ < 52.7	4.4 < 2 θ < 52.7
μ [mm ⁻¹]	0.26	0.20	0.24	0.20
T _{min} / T _{max} (low-angle)	0.83 / 0.99	0.90 / 0.98	0.92 / 0.99	0.92 / 0.99
T _{min} / T _{max} (high-angle)	0.79 / 0.93	0.91 / 0.98	0.94 / 0.96	0.94 / 0.98
used refl. after cut-off	37831	62860	97743	354381
sin θ / $\lambda_{\max, \text{cut}}$ [Å ⁻¹]	1.11	1.14	1.14	1.11
no. of unique reflections (low-angle batch) / R _{int}	2156 / 0.0461	3135 / 0.0287	2447 / 0.0567	6629 / 0.0435
no. of unique reflections (high-angle batch) / R _{int}	9652 / 0.0540	15135 / 0.0307	11553 / 0.0300	29791 / 0.0646
limiting indices	-13 ≤ h ≤ 13, -19 ≤ k ≤ 20, 0 ≤ l ≤ 22	-20 ≤ h ≤ 21, -19 ≤ k ≤ 21, 0 ≤ l ≤ 24	-20 ≤ h ≤ 16, 0 ≤ k ≤ 33, 0 ≤ l ≤ 21	-66 ≤ h ≤ 66, 0 ≤ k ≤ 25, 0 ≤ l ≤ 40

The raw data batches were independently corrected for absorption with the program MULABS implemented in PLATON,^[90] using an empirical approach. This program is based on the excellent algorithm developed by Blessing.^[91] The success of the absorption correction depends on the number of symmetry equivalents and multiple measured reflections. During determination of the correction function, these identical reflections are compared. The function which equals all multiplets most satisfactory is used. Obviously this works best, if a very high redundancy is given, since then the absorption-affected differences in the intensities can be separated from statistical variations.

The absorption corrected data files - still two independent batches - were then merged within the program XPREP,^[92] which was also used for space group determination. The merged data were assigned an individual batch number within the program BATCH^[93] and in a final step combined to one data set, which was the input for all subsequent calculations during structure solution and refinement. In table 3–3 the information concerning the data processing of compounds **I–IV** are compared.

3.4 Conventional (IAM) Refinements

Structure solution was performed with the program SHELXS-97^[94] using direct methods for all compounds.

Before the multipole model can be applied, a starting model based on the IAM has to be refined. This model is affected by principal errors, which have been discussed in chapter 3.1.1.1. To reduce the bias of shortcomings in the atomic model, a combination of high-order and low-order refinement (SHELXL-97^[95]) was performed to receive the best estimate of coordinates and thermal motion starting values.

Again, the refinements were carried out in the same manner for all compounds. In a first step the coordinates and the anisotropic parameters of the non-hydrogen atoms were refined, using exclusively the high-order reflections with $\sin\theta/\lambda \geq 1.00 \text{ \AA}^{-1}$. This relatively large value was feasible, as the high resolution of all data sets still yielded a reflection-to-parameter ratio of better than 10:1 after cut-off. Although $\sin\theta/\lambda \geq 1.00 \text{ \AA}^{-1}$ seems to be quite an extreme value, it was found to be sensible, as the atoms, which bear most information about the S–N bonding situation in all compounds are the two-coordinated nitrogen atoms

which should be affected without exception by the aspherical shift due to lone-pair densities.^[96] After convergence was reached, the parameters of the non-hydrogen atoms were fixed at the high-order values.

In a second step a difference Fourier synthesis was performed to localise the hydrogen atoms. For the calculation of the difference Fourier maps and the subsequent refinement of the hydrogen parameters exclusively reflections with $\sin\theta/\lambda \leq 0.5 \text{ \AA}^{-1}$ were used, since for those low-order reflections the relative contribution of diffuse densities is significant. The coordinates of the hydrogen atoms were refined without any distance constraints. The isotropic thermal motion of the hydrogen atoms was restrained by a riding model to 1.5 times the U_{eq} value of the parent sp^3 carbon atoms or 1.2 times the U_{eq} value of the bonded nitrogen atoms, respectively. After convergence was reached, the hydrogen atoms were shifted along the H–C and H–N bond vector to recommended distances found in neutron diffraction experiments: 1.085 Å for C(cp^3)–H and 1.032 Å for N–H, respectively.^[97] The results of the refinements of the starting models are presented in figure 3–1 and table 3–4.

Table 3-4: Crystallographic data after high-order refinements of compounds I-IV.

compound	I	II	III	IV
formula	$\text{S}(\text{N}^t\text{Bu})_2$	$\text{S}(\text{N}^t\text{Bu})_3$	$\text{H}(\text{N}^t\text{Bu})_2\text{SMe}$	$\text{CH}_2\{\text{S}(\text{N}^t\text{Bu})_2(\text{NH}^t\text{Bu})\}_2$
$\sin\theta/\lambda_{\text{min, cut}} [\text{Å}^{-1}]$	1.00	1.00	1.00	1.00
no. of refl. ($I > 4\sigma(I)$)	1463	3916	2706	5536
no. of parameters	101	146	110	298
$R1$ ($I > 4\sigma$)	0.0438	0.0246	0.0302	0.0427
$wR2$ (all data)	0.0982	0.0446	0.0544	0.0915
GoF	0.538	0.621	0.588	0.763

The low GoF-value ($1/\sigma^2$ weights) shows, that the esds of the integrated intensities of the high-angle batch are slightly underestimated. The esds of the calculated bond lengths and angles given in table 3–5 should therefore equally be underestimated. This should be considered in the discussion of the geometrical features. Therefore a significance threshold of three esds seems to be appropriate.

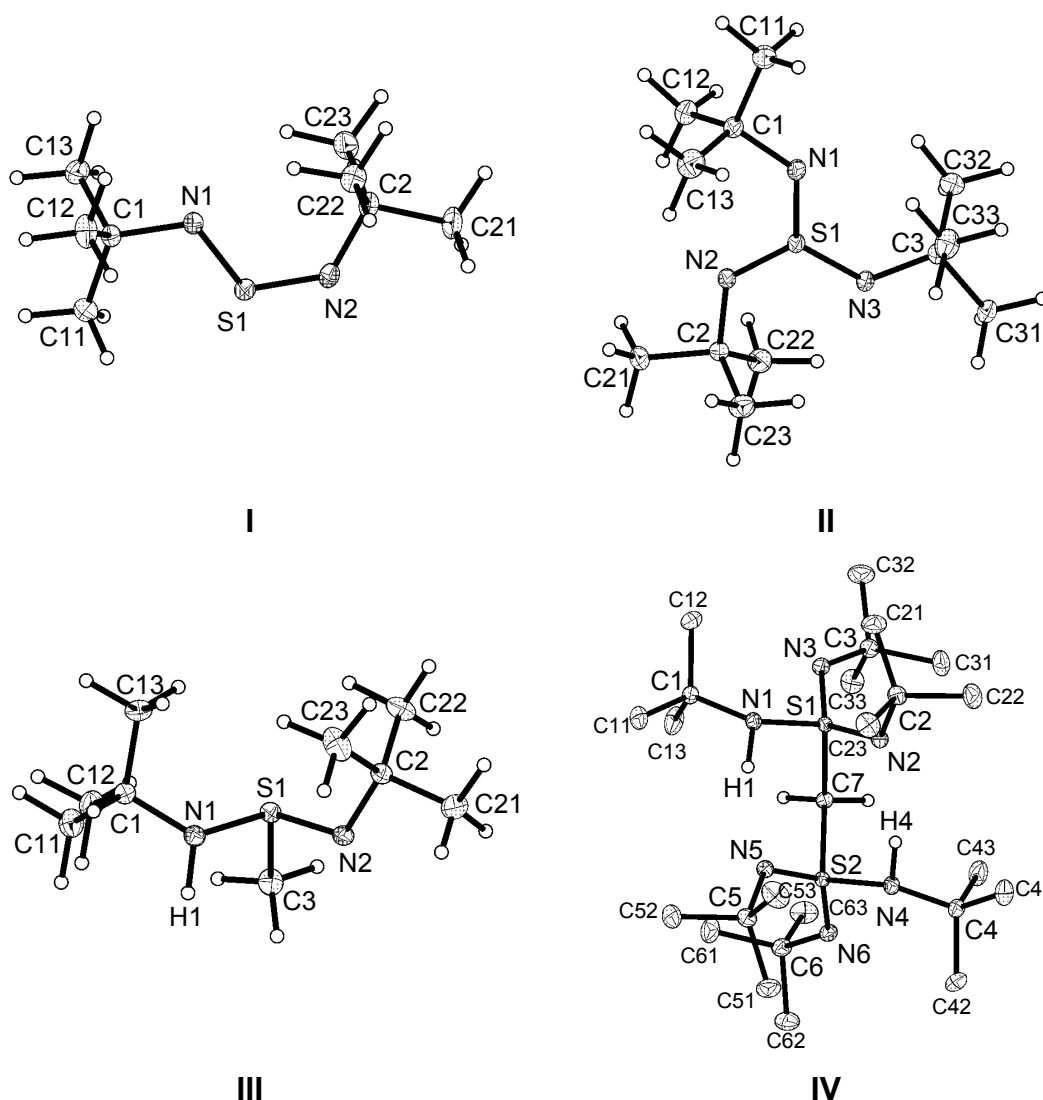


Figure 3-1: Asymmetric units of compounds **I-IV** after high-order refinement. The hydrogen atoms of the methyl groups of **IV** are omitted for clarity. The anisotropic displacement parameters are depicted at the 50% probability level.

Figure 3-2 shows a comparison of the difference Fourier synthesis after high-order IAM refinement. The density peaks can be related to residual densities which are not described by the model. Obviously the residual densities are mostly located in the interatomic and lone-pair regions, respectively, as it is expected for a spherical atom model.

The distribution is unusual in the sulfur diimide (**I**). The residual density distribution is extremely distorted in the SN_2 region. This distortion could be assigned to a non-adequate thermal motion model for the sulfur atom. The program package XD^[14] allows the application of an anharmonic motion model by a Gram-Charlier expansion described in chapter 3.1. For the anharmonic

refinement the high-order cut-off had to be reduced to $\sin\theta/\lambda \geq 0.80 \text{ \AA}^{-1}$, as an expansion to fourth order leads to 25 extra parameters: 10 for the third order and 15 for the fourth order coefficients. The success of the approach can be seen from the resulting residual map presented in figure 3–3.

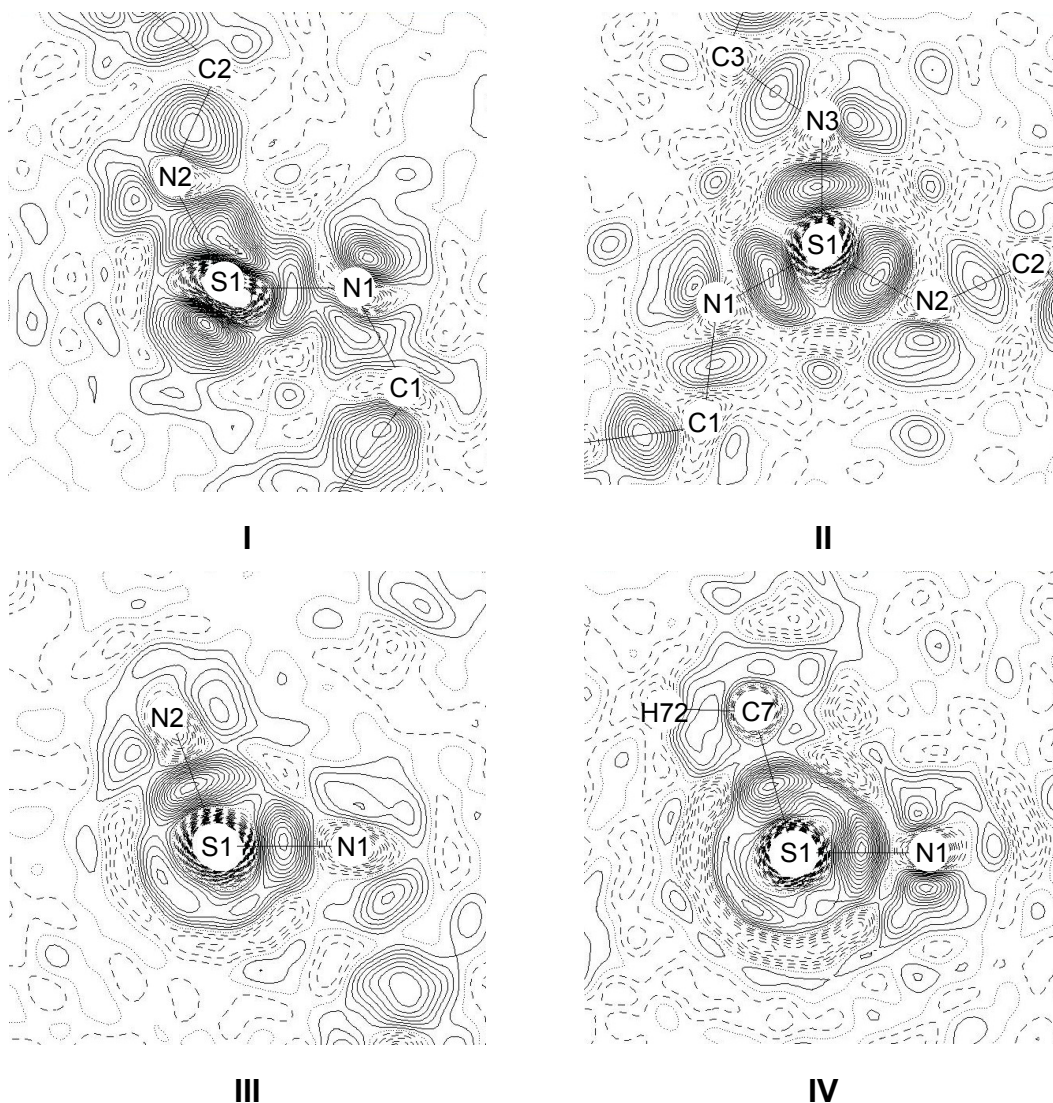


Figure 3-2: Residual densities in representative planes after high-order IAM refinement.

Stepwidth is 0.05 e\AA^{-3} , $\sin\theta/\lambda_{\text{max}} = 1.0 \text{ \AA}^{-1}$. Positive values solid lines, negative values dashed, zero value dotted. N(1)–S(1)–N(2) plane in I, SN_3 plane in II, N(1)–S(1)–N(2) plane in III and N(1)–S(1)–C(7) plane in IV, respectively.

The residual densities are much less distorted and are now located in the interatomic and lone-pair regions, respectively, as they are in the other compounds investigated in this thesis. As a further indicator for the model progress may serve, that 21 of the 25 anharmonic coefficients were refined to values larger than the associated esds.

It has to be mentioned that an anharmonic motion was tested for all other sulfur atoms in the studied compounds, but was only advantageous in **I**, as the difference Fourier maps of **II-VI** did not change significantly. Most of the anharmonic coefficients did not refine to significant values.

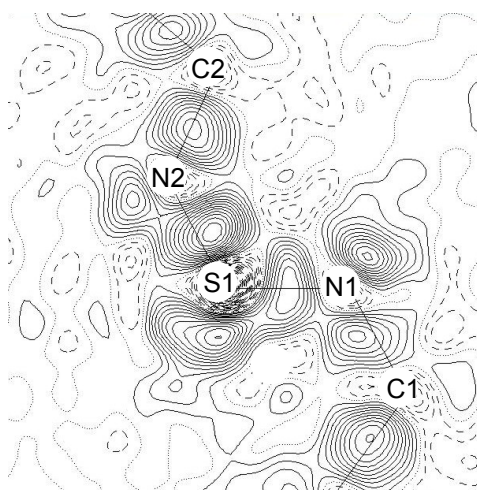


Figure 3-3: Residual density in the N(1)–S(1)–N(2) plane of **I** after anharmonic motion model refinement. Stepwidth is $0.05 \text{ e}\text{\AA}^{-3}$, $\sin\theta/\lambda_{\text{max}} = 1.0 \text{ \AA}^{-1}$. Positive values solid lines, negative values dashed, zero value dotted.

3.5 Structural Comparison

Since the main difference between the refinements, which are based on high-order IAM on one hand and the multipole model on the other hand, concerns the description of the diffuse densities, the standard structural features as bond lengths and angles do not change dramatically. Therefore the geometrical properties of compounds **I-IV** are discussed here, based on values determined from the high-order refinements. Selected bond lengths and angles calculated from the high-order IAM are compared in table 3–5.

In the solid state $\text{S}(\text{N}^t\text{Bu})_2$ (**I**) adopts a non- C_s symmetrical *E/Z* conformation. All atoms of the SN_2C_2 backbone are almost located in a plane with an average deviation from the mean plane of only 0.005 \AA . Within the *Z*- ^tBu group one of the methyl carbon atoms (C21) is also in the plane of the SN_2C_2 backbone (deviation 0.024 \AA), while its equivalent C11 of the *E*- ^tBu group is 0.276 \AA out of plane. The formal S=N bonds differ slightly in length with $1.5417(7) \text{ \AA}$ (S1–N1) and $1.5272(9) \text{ \AA}$ (S1–N2), respectively, but both are in the range quoted for a double bond.^[98,99]

Table 3-5: Selected bond lengths [Å] and angles [°] after high-order refinement (anharmonic model for sulfur in I). For IV averaged values of the S(N^tBu)₂(NH^tBu) units are presented, as no severe differences occur between the two moieties. The given esds are calculated as upper limits.

compound	I	II	III	IV
formula	S(N ^t Bu) ₂	S(N ^t Bu) ₃	H(N ^t Bu) ₂ SMe	CH ₂ {S(N ^t Bu) ₂ (NH ^t Bu)} ₂
S1,2–N1,4:	1.5417(7)	1.5087(3)	1.6823(4)	1.6487(16)
S1,2–N2,5:	1.5272(9)	1.5104(3)	1.5842(4)	1.5258(7)
S1,2–N3,6:		1.5110(3)		1.5157(13)
S1,2–C_{methyl(ene)}:			1.7928(4)	1.8163(7)
N1,4–C1,4:	1.4884(5)	1.4813(4)	1.4821(6)	1.4969(11)
N2,5–C2,5:	1.4745(6)	1.4838(4)	1.4863(5)	1.4901(31)
N3,6–C3,6:		1.4822(4)		1.4736(18)
N1,4–S1,2–N2,4:	117.5(1)	120.17(1)	110.09(2)	110.21(24)
N1,4–S1,2–N3,6:		119.92(1)		102.49(26)
N2,5–S1,2–N3,6:		119.91(1)		126.71(9)
N1,4–S1,2–C_{methyl(ene)}:			101.77(2)	105.77(5)
N2,5–S1,2–C_{methyl(ene)}:			100.01(2)	100.15(23)
N3,6–S1,2–C_{methylene}:				110.13(33)
S1–C–S2:				122.23(4)
S1,2–N1,4–C1,4:	118.5(1)	126.30(2)	119.56(3)	127.45(29)
S1,2–N2,5–C2,5:	128.1(1)	125.59(2)	115.02(3)	123.10(42)
S1,2–N3,6–C3,6:		126.06(2)		126.60(8)
N1,4–C1,4–C11,41:	115.1(1)	104.05(3)	105.43(5)	104.04(18)
N1,4–C1,4–C12,42:	106.6(1)	111.86(3)	112.31(4)	110.67(24)
N1,4–C1,4–C13,43:	106.0(1)	110.80(4)	110.34(4)	112.99(13)
N2,5–C2,5–C21,51:	105.5(1)	104.02(2)	104.94(4)	115.69(14)
N2,5–C2,5–C22,52:	110.7(1)	112.32(3)	112.46(4)	106.20(18)
N2,5–C2,5–C23,53:	110.3(1)	110.28(3)	112.61(5)	107.64(23)
N3,6–C3,6–C31,61:		104.11(2)		115.34(35)
N3,6–C3,6–C32,62:		111.52(3)		105.12(35)
N3,6–C3,6–C33,63:		111.21(4)		109.39(53)

Compared to other SN_2 units both formal $\text{S}=\text{N}$ double bonds are in the range of short interactions as can be seen from figure 3–4 depicting the results of a CSD search.^[99]

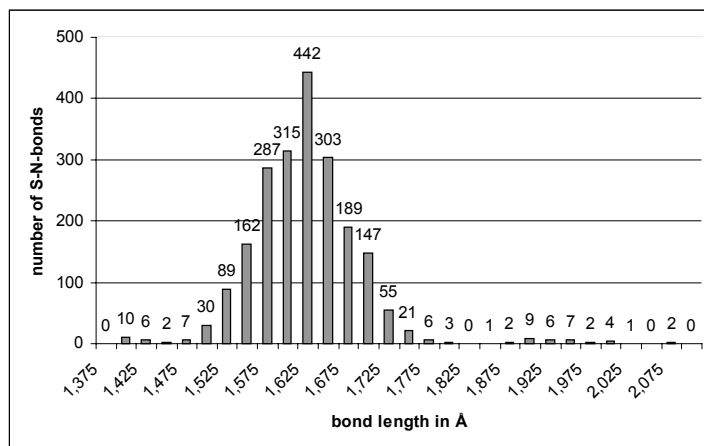


Figure 3-4: Statistical distribution of bond lengths in SN_2 -containing compounds obtained by a search for SN_2 units within the Cambridge Structural Database.^[99]

The same slight asymmetry is observed for the $\text{N}-\text{C}$ bonds. $\text{N1}-\text{C1}$ (E , 1.4884(5) Å) is slightly elongated compared to $\text{N2}-\text{C2}$ with 1.4745(6) Å (Z). With av. 1.532(2) Å (E) and av. 1.528(2) Å (Z), respectively, all $\text{C}-\text{C}$ bonds are in the expected range and do not differ significantly. Although the differences in the bond lengths between both $t\text{Bu}$ groups are insignificant, they are more noteworthy by means of the bond angles. The $\text{S}-\text{N}-\text{C}$ angles differ remarkably ($118.5(1)^\circ$ (E) vs. $128.1(1)^\circ$ (Z)), where the angle of the Z -group is that of a widened sp^2 nitrogen atom, while that of the E -group can be interpreted as contracted sp^2 or widened sp^3 angle, respectively.

This asymmetry is even more pronounced in the $\text{N}-\text{C}-\text{C}$ angles. While in the E -group the in-plane methyl carbon atom C11 forms a severely widened angle of $115.1(1)^\circ$, the corresponding angles of the out-of-plane carbon atoms are contracted and almost equal with $106.6(1)^\circ$ ($\text{N1}-\text{C1}-\text{C12}$) and $106.0(1)^\circ$ ($\text{N1}-\text{C1}-\text{C13}$). In the Z -group the opposite was found: while the angle of the almost in-plane carbon atom C21 is contracted to $105.5(1)^\circ$, those of the two other out-of-plane methyl carbon atoms are wider, almost equal ($\text{N2}-\text{C2}-\text{C22} = 110.7(1)^\circ$, $\text{N2}-\text{C2}-\text{C23} = 110.3(1)^\circ$), and in the expected range for a $\text{C}(\text{sp}^3)$. Obviously, the orientation of the methyl groups relative to the nitrogen lone-pairs is responsible for the angle deformation rather than the in-plane arrangement. The angle of the methyl groups C21 , C12 , and C13 pointing towards the nitrogen lone-pair is contracted, while that one of the methyl groups

pointing to the opposite direction is either widened or in the expected range for a sp^3 carbon atom.

As shown in figure 3–5, the crystal packing exhibits short S...S distances of 3.5663 (5) Å in the solid state, which are about 0.13 Å shorter than the sum of the van der Waals radii.^[100] An analogous arrangement has previously been observed in $\text{Te}\{\text{N}(\text{SiMe}_3)_2\}_2$.^[101] The nature of the assumed interaction between adjacent sulfur atoms in **I** will be discussed in chapter 3.8.2 in more detail.

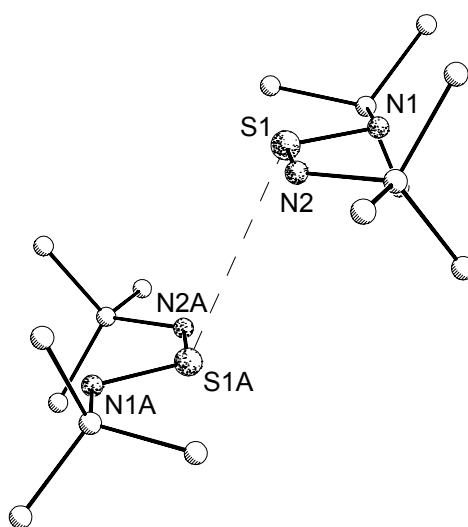


Figure 3-5: S...S linkage in the solid state structure of $\text{S}(\text{N}^t\text{Bu})_2$. Symmetry operation for the generation of the second molecule: centre of inversion at (0.5, 0.5, 0.5) followed by (1, 1, 1) translation.

The solid state structure of $\text{S}(\text{N}^t\text{Bu})_3$ (**II**) reveals no intermolecular interactions. The molecule shows almost exactly C_{3h} symmetry (av. $\text{N-S-N} = 120.0(2)^\circ$). The formal S=N bond lengths of av. 1.510(2) Å are slightly shorter compared to **I**. This shorter distances can be attributed to the higher oxidation state of the central sulfur atom (S^{IV} in **I** and S^{VI} in **II**).^[37b] However, the formal S=N bond lengths in the sulfurtriamide **II** fall at the short end of the range observed for SN_3 units with only seven hits in the Cambridge Crystallographic Database (see figure 3–6).

The N–C (av. 1.483(2) Å) as well as the C–C bonds (av. 1.528(4) Å) are in the normal range. For the in-plane methyl carbon atoms a slight bond elongation is observed, although those differences are at the limit of significance (mean difference: 0.0025 Å).

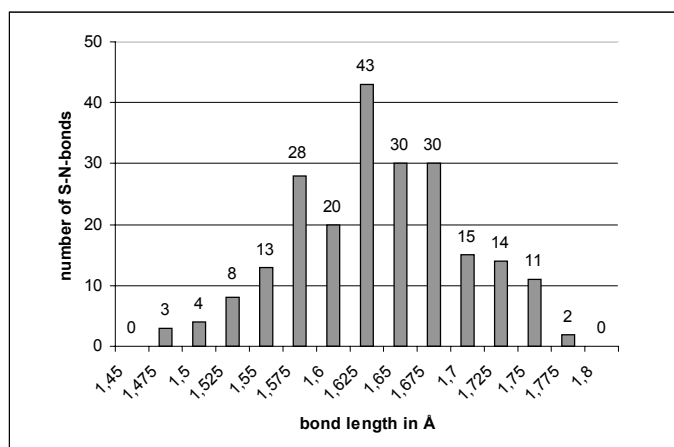


Figure 3-6: Statistical distribution of bond lengths in SN₃-containing compounds obtained by a search for SN₃ units within the Cambridge Structural Database.^[99]

The atoms of the SN₃C₃ core are located in a plane with an averaged deviation from the mean plane of only 0.021 Å. As already discussed by Pohl and coworkers,^[48] a slightly trigonal pyramidal arrangement for the SN₃ unit is not to exclude. Relative to the N₃ plane, the central sulfur and the tertiary carbon atoms are shifted towards the same direction, while the in-plane methyl carbon atoms are oriented about the same amount (some hundredth of an Ångström) in the opposite direction. Pohl and coworkers concluded that this finding can be verified by the extended out-of-plane thermal motion components. Although the preferred out-of-plane motion perpendicular to atomic bonds is expected from the rigid bond postulate,^[102] a comparison of the principal mean square atomic displacements supports their assumption.

Table 3-6: Principal mean square displacement amplitudes [10^{-2} Å²] of the sulfur and nitrogen atoms of compounds I and II.

	I	II
S1:	1.83 / 1.45 / 1.35	2.25 / 1.03 / 0.98
N1:	1.84 / 1.41 / 1.23	3.06 / 1.19 / 1.04
N2:	1.89 / 1.75 / 1.64	2.89 / 1.13 / 1.08
N3:		2.98 / 1.20 / 1.04

Table 3-6 shows that the out-of-plane components in II are at least two times the values of the in-plane motion which is not the case for I. This feature can be attributed to a slight disorder of the SN₃ units in II with respect to their mean plane. Due to the relatively low temperature of 100 K this disorder is assumed to be of static rather than of dynamic nature.

The slightly widened S–N–C angles of av. $126.0(4)^\circ$ are in agreement with sp^2 hybridised nitrogen atoms. In each t Bu group one methyl carbon atom is located almost in the mean plane (deviations: C11: 0.071 Å, C21: 0.107 Å, C31: 0.042 Å). Like C21 in the sulfur diimide (I), the in-plane methyl groups point towards the nitrogen lone-pairs and form contracted angles of av. $104.1(1)^\circ$, while the angles of the out-of-plane located methyl groups vary from $110.28(3)^\circ$ (N2–C2–C23) to $112.32(3)^\circ$ (N2–C2–C22).

$H(N^tBu)_2SMe$ (III) adopts a dimeric twisted boat conformation of a $S_2N_4H_2$ eight-membered ring (see figure 3–7) due to intermolecular hydrogen bonding of H1 to the opposite formally double bonded N2A. The N1...N2A distance is 3.044(3) Å, while the H1...N2A distance is 2.028(2) Å. The angle N1–H1...N2A is $167.3(2)^\circ$.

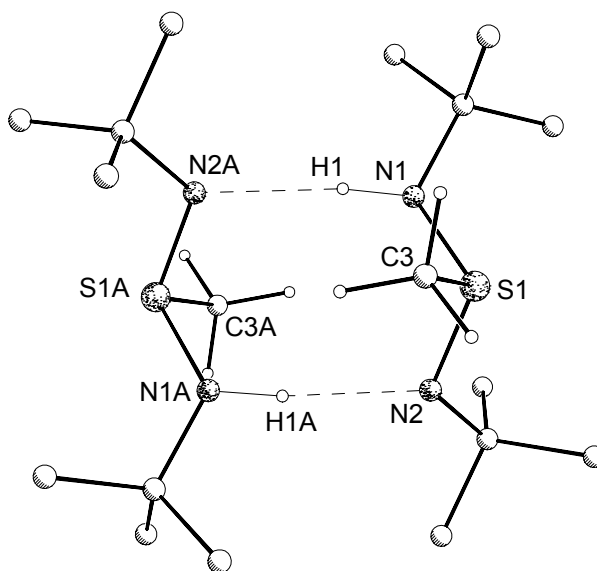


Figure 3-7: Dimeric solid state structure of $H(N^tBu)_2SMe$ (III). Symmetry operation for the generation of the dimer: centre of inversion at (0.5, 0, 0) followed by (1, 0, 0) translation.

The N–H...N hydrogen bonds in III have to be regarded as strong ones. In the literature A–H...B hydrogen bonds are often classified along the A–B non-hydrogen atom distances. If the A–B distances exceed the sum of the van der Waals radii^[100] only slightly a weak hydrogen bond results.^[103] Since the sum of the van der Waals radii in a N–H...N hydrogen bond is 3.10 Å, the current hydrogen bond in III is quite strong as the N1...N2A distance of 3.044(3) Å is considerably shorter. Therefore the hydrogen bond formation in the dimerisation of III is an important energetic contribution to the solid state lattice energy.

Threefold substitution of the nitrogen atom in the S–N(H)^tBu moiety gives rise to an unambiguous S–N1 single bond (1.6823(4) Å) and a formal S=N^tBu double bond (1.5842(4) Å). S1=N2 is on average 0.05 Å longer than the formal double bonds found in the sulfur diimide (**I**). At first sight this bond elongation might be attributed to the hydrogen bond in which N2 acts as the acceptor.

However, the intramolecular hydrogen bonds in CH₂{S(N^tBu)₂(NH^tBu)}₂ (**IV**) do not support this conclusion. The averaged H···N distance in **IV** is 2.153(3) Å with a mean N–H···N angle of 142.0(8)°. The short N···N distances of av. 3.033(9) Å also support the assumption of a strong hydrogen bond. But in contrast to the situation in **III**, the formal S=N(acceptor) bonds in **IV** are not that much elongated (av. S=N: 1.520(6) Å) and match almost exactly the averaged distance in **II** of 1.510(3) Å.

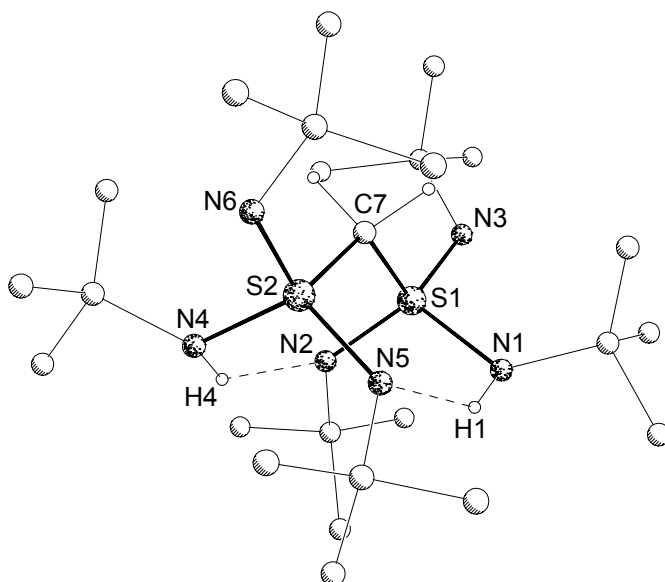


Figure 3-8: Hydrogen bonds in CH₂{S(N^tBu)₂(NH^tBu)}₂ (**IV**).

The S1–N1–H1–N5–S2–N4–H4–N2 moiety in **IV** forms a boat conformation, bow and stern connected by the CH₂ bridge, where the N–H···N angles are much smaller than those found for the intermolecular bridge in **III** (figure 3–8).

The sulfur atom in **III** is coordinated trigonal pyramidal indicating sp³ hybridisation. The S–C bond of 1.7928(4) Å in **III** is comparable to bond lengths quoted in literature for S–C bonds.^[38,104] The S–C bond of 1.8163(7) Å in **IV** is slightly longer, which is expected from the oxidation state of the formal S^{VI} sulfur atom.

The arrangement of the ^tBu groups in **III** differs from those in **I** and **II**. No in-plane orientation of one of the methyl carbon atoms with the SN₂-moiety is

found and relatively high deviations from the S–N–C planes are observed (0.165 Å (C11) and 0.211 Å (C21)). The N–C bonds are almost equal, while the S–N–C angles differ less than expected ($S1-N1-C1 = 119.56(3)^\circ$, $S1-N2-C2 = 115.02(3)^\circ$). It is remarkable that the formally sp^3 hybridised N1 shows the wider angle compared to the formally sp^2 hybridised N2. The relatively narrow angle at N2 might be taken as the first hint that a single in-plane lone-pair at N2 is not present.

The C–C bonds within the t Bu groups differ slightly in length, while only the mean elongation of 0.0095 Å for C2–C22 is significant.

The N–C–C angles reveal the same features observed in the other compounds: the angles formed with participation of the methyl carbon atoms located closest to the nitrogen lone-pairs are contracted ($N1,2-C1,2-C11,21$: av. $105.2(3)^\circ$), while the other N–C–C angles are with averaged $112.4(2)^\circ$ slightly widened. An exception is found for the carbon atom C13 ($N1-C1-C13 = 110.34(4)^\circ$). This methyl group is slightly inclined towards the N1–C1 bonding region and the anticipated lone-pair at N1.

Like in **III** different S–N bonding modes are observed in $CH_2\{S(N^tBu)_2(NH^tBu)\}_2$ (**IV**): two S–N(H) single bonds ($S1,2-N1,4$: av. $1.6487(16)$ Å) and four formal S=N double bonds. Two are slightly elongated, as the related nitrogen atoms are acceptors in the hydrogen bonding ($S1,2-N2,5$: av. $1.5258(7)$ Å) and two are unaffected ($S1,2-N3,6$: av. $1.5157(13)$ Å).

The molecule consists of two $S(N^tBu)_2(NH^tBu)$ moieties linked by CH_2 and two intramolecular hydrogen bonds, which have already been discussed above. According to the Cahn-Ingold-Prelog rules, the structure of $CH_2\{S(N^tBu)_2(NH^tBu)\}_2$ is S/S chiral. Both moieties are almost equal concerning bond lengths and angles, giving rise to a non-crystallographic twofold axis through C7 and the centre of the S1–C7–S2 unit. The wide S1–C7–S2 angle of $122.23(4)^\circ$ reflects considerable steric strain between the two bulky methylene substituents. The angle opening is less pronounced than in $[(thf)_2Li_2\{N^tBu\}_3SCH_2S(N^tBu)_3]$ ($S-C-S = 126.7(2)^\circ$),^[56] where the additional widening is caused by chelating metal coordination.

In each moiety the central sulfur atom is tetrahedrally coordinated by three nitrogen atoms and the carbon atom of the bridging CH_2 unit. The tetrahedral coordination polyhedron is considerably distorted, indicated by the angles variation of more than 26° ($N1,4-S1,2-N2,5 = 110.21(24)^\circ$, $N1,4-S1,2-N3,6 =$

102.49(26)°, N2,5–S1,2–N3,6 = 126.71(9)°, N1,4–S1,2–C7 = 105.77(5)°, N2,5–S1,2–C7 = 100.15(23)°, N3,6–S1,2–C7 = 110.13(33)°.

The C–N bond lengths differ only slightly and are in the expected range from 1.4736(18) Å (N3,6–C3,6) to 1.4969(11) Å (N1,4–C1,4). The S–N–C angles of S1,2–N1,4–C1,4 = 127.45(31)°, S1,2–N2,5–C2,5 = 123.10(42)°, and S1,2–N3,6–C3,6 = 126.60(8)° are all wider than the expected 120° for the formally sp² hybridised nitrogen atoms N2,5 and N3,6. At first sight the greater angles might be attributed to steric strain imposed by the bulky ^tBu groups.

All C–C bonds are almost identical in lengths with 1.533(7) Å on average. The angles show a wide variation due to steric hindrance between adjacent ^tBu groups and attractive interactions from hydrogen bonds. The angles in the ^tBu groups of both S(N^tBu)₂(NH^tBu) moieties are almost identical. As already observed before are some of the N–C–C angles contracted, while others are slightly widened.

In the formally double bonded N^tBu groups two methyl carbon atoms are oriented towards the nitrogen lone-pair densities. The corresponding N–C–C angles are contracted (N2,5–C2,5–C22,52 = 106.20(18)°, N2,5–C2,5–C23,53 = 107.64(23)°, N3,6–C3,6–C32,62 = 105.12(35)°, N3,6–C3,6–C33,63 = 109.39(53)°). The methyl carbon atoms, which point away from the lone-pair density of the formal double bonded nitrogen atoms, make up largest N–C–C angles found (N2,5–C2,5–C21,51: 115.69(14)°, N3,6–C3,6–C31,61: 115.34(35)°).

For the single bonded N^tBu groups the findings are even more striking. The N1,4–C1,4–C11,41 angles are with 104.04(15)° in the range of the smallest angles found in all investigated compounds, while N1,4–C1,4–C12,42 and N1,4–C1,4–C13,43 are widened with 110.67(24)° and 112.99(13)°, respectively. Again the angle contractions can be attributed to the almost parallel orientation of the C–C bonds to the expected lone-pair-atom vector of the single bonded sp³ nitrogen atoms.

In summary it can be stated, that in all compounds the methyl carbon atoms of the N^tBu groups, which are oriented towards the lone-pair densities of the nitrogen atoms form contracted N–C–C angles, independent from their positions relative to the corresponding S–N–C planes. Unequivocally this must be indicative to an attractive interaction between the lone-pairs and the C–C bonding densities. Since predominantly bending of methyl groups towards

nitrogen lone-pair regions and no significant and consistent changes in the C–C bond lengths were observed – the difference between the shortest and longest C–C bond from all thirteen ^tBu groups in four experiments is only 0.012 Å – the responsible phenomenon has to be very weak. Merely from the orientation of the C–C σ -densities of the ^tBu groups, in plane or apical to the S–N–C planes, hyperconjugation effects might be considered.^[105] Since no significant changes in the bond lengths of the IAM model are observed, the question about the nature of the interactions and the consequences to the charge density distributions are discussed later in this thesis from an electron density point of view.

3.6 Multipole Refinements

Concerning the refinement strategy, the application of local symmetry restrictions and similarity constraints, the employment of radial functions, and the flexibility of the multipole model, all compounds have been treated equally as far as this was feasible for the different symmetries and coordination modes.

In the atomic ED model implemented XD^[14] the deformation density is expanded in terms of Slater-type radial functions. The coefficients n_i of the sulfur atoms were changed to the recommended values ($n_1=4$, $n_2=4$, $n_3=6$, $n_4=8$),^[106] which has been shown a meaningful method especially for sulfur containing compounds.^[107,108] For carbon and nitrogen atoms, respectively, the default values with energy-optimised exponents were used.^[109]

For all hydrogen atoms energy-optimised values were selected too.^[109] Therefore the starting values for the expansion/contraction factors were set to 1.2. It is emphasised that for the refinement of hydrogen atoms several models have been tested due to their diffuse ED distribution and the related problems.

An approach described by Volkov, Abramov and Coppens^[110] was tested and compared with other strategies. Their method is based on the usage of density-optimised radial exponents from *ab initio* calculations. This leads to recommended contraction/expansion parameters for the hydrogen atoms: 1.15 (κ) and 1.40 (κ') for nitrogen bonded and 1.10 (κ) and 1.18 (κ') for carbon bonded hydrogen atoms, respectively. These values should be kept fixed during refinements. The comparison of calculated properties (densities, BCPs,

Laplacian distributions) did not lead to severe changes, depending on the hydrogen model.

Therefore in this thesis a refinement model for the hydrogen atoms was used, which allows the deformation density terms to expand *via* refinement of the contraction/expansion parameters. This model was applied successfully in our group and was tested excessively when we started to develop strategies for multipole refinements.

The complexity of the refined density models was increased stepwise. In the first refinement cycles exclusively the populations of the sulfur atoms were refined to the fourth order. All other non-hydrogen atoms were refined to the third order. For the hydrogen atoms a bond-directed dipole as well as a quadrupole population were refined, respectively. Equal atom types shared the same κ -set. After convergence was reached, the population parameters of the nitrogen atoms were refined to the fourth order, as those of the bridging carbon atom in **IV** and the sulfur bonded carbon atom in **III**, respectively. The model was refined against F_H^2 with an $1/\sigma^2$ weighting scheme, using exclusively reflections with intensities $I > 3\sigma(I)$ until convergence was reached for the complete model. Then a refinement with all positive F_H^2 without any $\| \sigma(I) \|$ -restrictions was appended.

Several refinement strategies were tested. A proceeding, which resulted in a convergent refinement with chemically and physically meaningful parameters for all compounds is presented in detail:

Starting from the IAM (anharmonic for sulfur in **I**), the scaling factors (SFs) were adjusted. During subsequent steps of the refinements the SFs were included if not mentioned explicitly. In a first step the monopole populations together with the κ of the non-hydrogen atoms were refined. Then the multipole populations were refined. After that the P_v , P_{lm} and κ , including those of the hydrogen atoms were block-refined, followed by a refinement of the κ' -values of the non-hydrogen atoms. Subsequently the positional and thermal motion parameters of S, N and C, respectively, were refined, followed by an adjustment of x , y , z and U_{iso} of the hydrogen atoms with the resolution restriction $\sin\Theta/\lambda \leq 0.5 \text{ \AA}^{-1}$. In the next step all parameters but the κ' -values of the hydrogen atoms were block-refined. After adjustment of the hydrogen values all parameters of the multipole model were included. After convergence was reached, the last cycles were

repeated without any $//\sigma(I)$ restrictions. The density models resulting from this strategy were examined in the further analyses.

Several local (non-crystallographic) symmetry restrictions and similarity constraints were implemented to reduce the number of refinement parameters. Application of local symmetry is required as the spherical harmonics have to be compatible to these symmetries. This can reduce the number of refined multipoles dramatically. As an example may serve the local threefold axis perpendicular to the SN_3 plane at the central sulfur atom in **II**. Application of this local symmetry reduced the number of refined populations from 25 to 9.

Similarity constraints can be applied if groups of atoms show the same chemical and geometrical environment. The multipole populations as well as the contraction/expansion coefficients of these atoms can be constrained. A proper application of these restrictions reduces the number of refinement parameters remarkably. It is pointed out, that similarity constraints exclusively affect the populations and expansion/contraction parameters. Coordinates and thermal motion parameters were not constrained.

Local symmetry restrictions and similarity constraints for compounds **I-IV** are listed below:

- $S(N^tBu)_2$ (**I**):

local symmetry: threefold axis along the C–C bonds in the tBu groups.

similarity constraints: all methyl carbon atoms and all hydrogen atoms.

- $S(N^tBu)_3$ (**II**):

local symmetry: threefold axes for the sulfur atom perpendicular to the SN_3 plane and along the C–C bonds in the tBu groups.

similarity constraints: all methyl carbon atoms and all hydrogen atoms; all tertiary carbon and nitrogen atoms as a consequence from the symmetry at the sulfur atom.

- $H(N^tBu)_2SMe$ (**III**):

local symmetry: threefold axes along the C–C and the C–S bonds.

similarity constraints: all methyl carbon atoms of the N^tBu groups, all hydrogen atoms.

- $\text{CH}_2\{\text{S}(\text{N}^t\text{Bu})_2(\text{NH}^t\text{Bu})\}_2$ (**IV**):

local symmetry: twofold axis through the bridging carbon atom and the centre of S1–CH₂–S2; threefold axis along the C–C bonds.

similarity constraints: all methyl carbon atoms, all carbon bonded hydrogen atoms of the methyl groups, and all nitrogen bonded hydrogen atoms; the two hydrogen atoms of the bridging CH₂ group; all atom pairs of the two S(N^tBu)₂(NH^tBu) moieties, as a consequence from the twofold axis.

For all compounds a convergent model was refined using the strategy described above. In table 3–7 the crystallographic data resulting from the multipole refinements of compounds **I–IV** are compared.

Rather than the excellent *R*-values of the multipole refinement, the distributions of the residual densities depicted in figure 3–9 serve as a reliable indicator for a successful description of the molecular densities. The residual density maps are flat and featureless. The few low residual peaks are located mostly in the intermolecular regions where the atom-centred multipole expansions can not model densities sufficiently from principal reasons.

Table 3-7: Crystallographic data after multipole refinements of compounds **I–IV**.

compound	I	II	III	IV
formula	S(N ^t Bu) ₂	S(N ^t Bu) ₃	H(N ^t Bu) ₂ SMe	CH ₂ {S(N ^t Bu) ₂ (NH ^t Bu)} ₂
max. shift / esd	0.36 10 ⁻²	0.83 10 ⁻²	0.11 10 ⁻¹	0.30 10 ⁻⁵
<i>R</i> 1 (<i>I</i> > 3σ)	0.0203	0.0180	0.0210	0.0251
<i>wR</i> 2 (all data)	0.0314	0.0293	0.0271	0.0280
GoF	1.1631	1.5970	1.2344	1.3015
no. reflections	11808	18250	14000	36420
no. of refl. used (<i>I</i> > 0)	10980	17520	13279	32716
<i>N</i> _{refl.} / <i>N</i> _{param.}	44.1	82.6	53.5	67.9

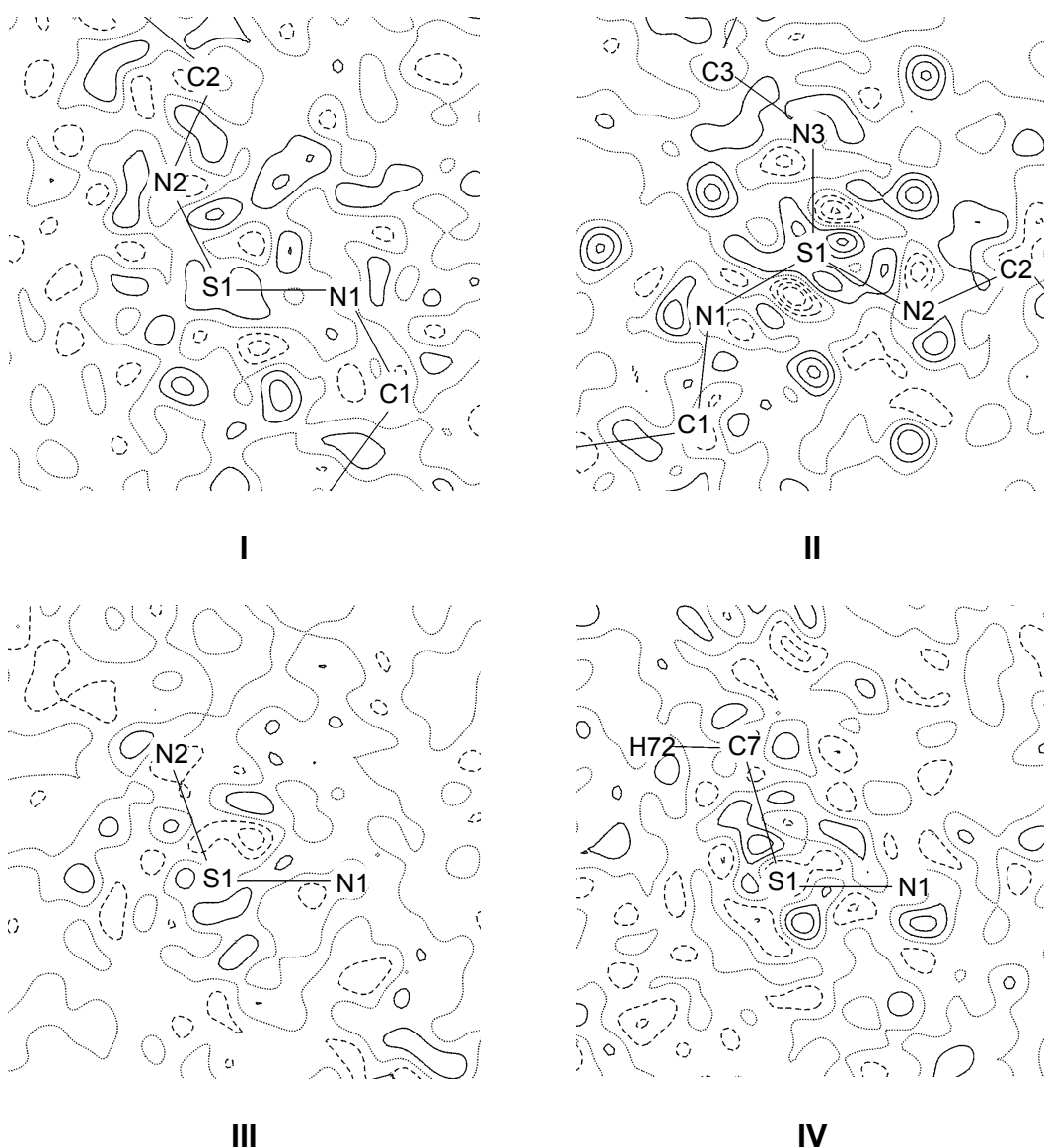


Figure 3-9: Residual densities in representative planes after multipole refinement. Stepwidth is $0.05 \text{ e}\text{\AA}^{-3}$, $\sin\theta/\lambda_{\text{max}} = 1.0 \text{ \AA}^{-1}$. Positive values solid, negative values dashed, zero value dotted lines. N(1)–S(1)–N(2) plane in I, SN₃ plane in II, N(1)–S(1)–N(2) plane in III and N(1)–S(1)–C(7) plane in IV, respectively.

Different to the other three investigations the residual density in II shows a systematic distribution. The maximum values of about $0.15 \text{ e}\text{\AA}^{-3}$ are almost as small as in the other molecules, but the orientation of the most distinct density peaks can be related to a disorder of the whole molecule caused by a 60° rotation about the molecular threefold axis. It was tried to model this disorder in a conventional refinement with the program SHELXL,^[95] but the site occupation factors of the less populated fragment refined to zero. This is not surprising, as the peak heights of $0.15 \text{ e}\text{\AA}^{-3}$ at the expected carbon or nitrogen atom positions,

respectively, indicate an occupation of less than 2%. Nevertheless, the possible existence of a non-resolved disorder has to be taken into account if density related properties are discussed. This is even more striking if the second possible disorder is taken into account. As already mentioned in chapter 3.5, indicators for a not to resolve slight disorder of the central SN_3 unit perpendicular to its mean plane were observed.

Selected bond lengths and angles after multipole refinement are presented in table 3–8 and table 3–9. As they do not differ significantly from the values obtained by high-order refinement, the geometrical features of compounds **I–IV** are not discussed in detail again and may serve for comparison purposes only.

Table 3-8: Selected bond lengths [Å], including the intermolecular (**III**) and the intramolecular hydrogen bond (**IV**), respectively, after multipole refinement (anharmonic model for sulfur in **I**). For **IV** averaged values of the $\text{S}(\text{N}^t\text{Bu})_2(\text{NH}^t\text{Bu})$ units are presented, as no severe differences occur between the two moieties. The given esds are calculated as upper limits.

compound	I	II	III	IV
formula	$\text{S}(\text{N}^t\text{Bu})_2$	$\text{S}(\text{N}^t\text{Bu})_3$	$\text{H}(\text{N}^t\text{Bu})_2\text{SMe}$	$\text{CH}_2\{\text{S}(\text{N}^t\text{Bu})_2(\text{NH}^t\text{Bu})\}_2$
S1,2–N1,4:	1.5437(4)	1.5116(2)	1.6829(2)	1.6494(2)
S1,2–N2,5:	1.5279(4)	1.5120(2)	1.5847(2)	1.5279(3)
S1,2–N3,6:		1.5113(2)		1.5177(6)
S1,2–C_{methyl(ene)}:			1.7907(2)	1.8164(5)
N1,4–C1,4:	1.4871(4)	1.4828(2)	1.4814(3)	1.4971(9)
N2,5–C2,5:	1.4758(4)	1.4848(2)	1.4860(3)	1.4899(11)
N3,6–C3,6:		1.4823(2)		1.4737(5)
(N1)H1...X1_N2: ^a			2.0271(2)	
N1–H1...X1_N2: ^a			167.8(1)	
(N1)H1...N5:				2.1568(3)
(N4)H4...N2:				2.1379(3)
N1–H1...N5:				142.6(1)
N4–H4...N2:				142.7(1)

^a X1 = 1-x, -y, -z

The higher esds after multipole refinement compared to the values after high-order IAM refinement are not caused by model shortcomings, but due to different determinations in the two programs XD and SHEXL. The esds calculated by the program XD after multipole refinement can serve as an upper limit.

Table 3-9: Selected angles [°] after multipole refinement (anharmonic model for sulfur in the case of I). For IV averaged values of the S(N^tBu)₂(NH^tBu) units are presented, as no severe differences occur between the two moieties. The given esds are calculated as upper limits.

compound	I	II	III	IV
formula	S(N ^t Bu) ₂	S(N ^t Bu) ₃	H(N ^t Bu) ₂ SMe	CH ₂ {S(N ^t Bu) ₂ (NH ^t Bu)} ₂
N1,4–S1,2–N2,5:	117.4(1)	120.2(1)	110.1(1)	110.2(3)
N1,4–S1,2–N3,6:		119.9(1)		102.4(3)
N2,5–S1,2–N3,6:		119.9(1)		126.8(2)
N1,4–S1,2–C_{methyl(ene)}:			101.9(1)	105.9(1)
N2,5–S1,2–C_{methyl(ene)}:			100.0(1)	100.2(4)
N3,6–S1,2–C_{methyl(ene)}:				110.2(3)
S1–C–S2:				122.2(1)
S1,2–N1,4–C1,4:	118.3(1)	126.1(1)	119.6(1)	127.3(3)
S1,2–N2,5–C2,5:	128.1(1)	125.5(1)	115.0(1)	123.0(5)
S1,2–N3,6–C3,6:		125.9(1)		126.5(2)
N1,4–C1,4–C11,41:	115.1(1)	103.9(1)	105.4(1)	104.0(2)
N1,4–C1,4–C12,42:	106.6(1)	111.8(1)	112.2(1)	110.6(2)
N1,4–C1,4–C13,43:	106.0(1)	110.8(1)	110.2(1)	113.1(1)
N2,5–C2,5–C21,51:	105.5(1)	104.0(1)	104.9(1)	115.7(1)
N2,5–C2,5–C22,52:	110.7(1)	112.2(1)	112.6(1)	106.2(1)
N2,5–C2,5–C23,53:	110.3(1)	110.3(1)	112.5(1)	107.7(3)
N3,6–C3,6–C31,61:		104.0(1)		115.4(4)
N3,6–C3,6–C32,62:		111.5(1)		104.9(3)
N3,6–C3,6–C33,63:		111.1(1)		109.3(41)

The reliability of the refined parameters was checked by Hirshfeld's rigid body test.^[102] Although the mass differences of S–E (E = C, N) are not neglectable, the differences in the mean square displacement amplitude (MSDA) are very small. In table 3–10 the differences of the MSDAs of the most important bonds are listed.

Table 3-10: Differences of the MSDAs [10^{-4} \AA^2] of selected bonding pairs of atoms in I-IV.

compound	I	II	III	IV
formula	S(N ^t Bu) ₂	S(N ^t Bu) ₃	H(N ^t Bu) ₂ SMe	CH ₂ {S(N ^t Bu) ₂ (NH ^t Bu)} ₂
S1,2–N1,4:	2	3	3	3
S1,2–N2,5:	0	3	2	3
S1,2–N3,6:		4		4
S1,2–C_{methyl(ene)}:			9	10 / 12
N1,4–C1,4:	6	5	4	5
N2,5–C2,5:	8	5	4	8
N3,6–C3,6:		5		10 / 7
C–C:	≤ 6	≤ 5	≤ 7	≤ 10

The results of the rigid bond test are excellent. Apart from the S–C bond in **IV**, for which the mass differences are most distinct, all values are smaller or equal than $10 \times 10^{-4} \text{ \AA}^2$. Therefore the bond lengths do not have to be corrected for thermal motion effects. Furthermore it is evident, that the deconvolution of the density smearing due to thermal motion on one hand and due to bonding effects on the other hand was successful. This is a necessary condition for the determination of physically meaningful density distributions from the multipole refinement.

In figure 3–10 three-dimensional representations of $\Delta\rho_{\text{static}}(\mathbf{r})$ are presented. They already show the main structural properties, such as bonding densities and lone-pairs at the nitrogen and sulfur atoms.

Obviously, the distributions of $\Delta\rho_{\text{static}}(\mathbf{r})$ are already suitable to describe the major features. Figure 3-10 reveals maxima in the lone-pair regions of both nitrogen and sulfur atoms, as well as bonding density in the interatomic regions of all compounds. The static deformation densities exhibit some typical features:

The distributions in σ -bonds show cylindrical symmetry (e.g. the C–C bonds, the N–C bonds, S1–C3 in **III**, or S1–C7 in **IV**, respectively). Although the spatial orientation of lone-pairs can not clearly be assigned yet as these densities are smeared, for some of the formal sp^2 hybridised nitrogen atoms remarkably high density maxima *outside* the related S–N–C planes are present. Most obvious it is at N2 in **III** and around N2 and N3 in **IV**. Almost all bonding density distributions in the S–N bonds differ from rotational symmetry. This can either be attributed to the nearby smeared lone-pair densities of the nitrogen (**I–IV**) or sulfur atoms (**I**, **III**), respectively, or to π -contribution for formal S=N double bonds. The density distributions in the non-bonding regions of the sulfur atoms are quite remarkably. According to their oxidation state, the S^{IV} atoms in **I** and **III** show striking lone-pair densities in the anticipated spatial orientation, while the S^{VI} atoms in **II** and **IV** do not. Perpendicular to the SN_3 plane in **II** a depletion of the static deformation density at the sulfur atom is observed. The out-of-plane extension of the S–N bonding densities in **II** could be affected by the mentioned disorder of the central SN_3 unit, since the refined densities always display a mean distribution.

In addition to the spatial distribution of the static deformation density its variation along the bond path was analysed. $\Delta\rho_{\text{static}}(\mathbf{r})$ was calculated along the interatomic vector with a stepwidth of 0.01 Å. The maximum values of $\Delta\rho_{\text{static}}(\mathbf{r})$ and their positions in the S–E (E = N, C) bonds are given in table 3–11.

This analysis provides another hint that the S–N bonds in the sulfurdiiimide are only equivalent by formal means. The charge density maxima of both bonds differ by almost the factor of two (0.42 to 0.80 eÅ⁻³). While the first maximum at the S1–N1 bond is shifted two thirds of the bond length towards N1, the higher at the S1–N2 bond is shifted one third towards the sulfur atom. This situation is almost identical to the height and location of the maximum in the S–N bond in

$S(N^tBu)_3$ (II). The small differences in the positions of the maxima can be attributed to the slightly longer bond in the sulfur diimide (I).

Table 3-11: Maximum value and its position of the static deformation density. The first value denotes the maximum of $\Delta\rho_{static}(r)$ [$e\text{\AA}^{-3}$], the second is the distance of the maximum from the sulfur atom [\AA].

compound	I	II	III	IV
formula	$S(N^tBu)_2$	$S(N^tBu)_3$	$H(N^tBu)_2SMe$	$CH_2\{S(N^tBu)_2(NH^tBu)\}_2$
S1–N1:	0.42 / 0.99	0.81 / 0.51	0.52 / 0.69	0.57 / 0.91
S1–N2:	0.80 / 0.54		0.62 / 0.63	0.74 / 0.60
S1–N3:				0.79 / 0.58
S1–C_{methyl(ene)}:			0.61 / 0.68	0.50 / 0.84

The two S1–N1 single bonds in III and IV exhibit almost the same height of the deformation density maximum (0.52 and 0.57 $e\text{\AA}^{-3}$) but the location differs considerably. While the first is almost halfway between S and N, the second is shifted towards N1. The formal double bond in III shows higher density (0.62 $e\text{\AA}^{-3}$) and the position of the maximum is comparable to the formal double bonds in IV if the different bond lengths of 1.584 \AA in III vs. av. 1.523 \AA in IV are considered.

From the three different S–N bonds in IV a trend can be deduced, which is valid for all thirteen different S–N bonds analysed in this thesis: the shorter the bond the higher the maximum of the static deformation density and the higher the maximum the closer it is shifted towards the electropositive sulfur atom. This already highlights the important role of electrostatic contributions to sulfur-nitrogen bonding and will later be discussed in detail.

The same seems applicable to the S–C bonds, although only three different bonds were studied in this thesis. The higher maximum at the S–C bond in III is located closer to the single sulfur atom than the lower maximum in IV. In the methylene bridge two electropositive sulfur atoms compete for the charge density.

The formal equivalent bonds in IV are in quite good agreement, while the deformation density maximum of S1–N1 is as expected smaller (0.57 $e\text{\AA}^{-3}$) for this long single bond and shifted towards N1.

The static deformation density is an instructive tool to visualise the density distribution by direct representation of the features of interest. However, the severe limitations should be kept in mind. A topological analysis, independent from any reference state, is much more suitable to determine the density related properties. It is slightly disadvantageous that chemical features have to be deduced more indirectly as the topological analysis is based on first and second derivatives of the density.

3.8 Topological Analyses

For all compounds detailed topological analyses according to Bader's theory of 'Atoms in Molecules'^[21] were performed. All calculations were carried out with the program XDPROP implemented in the XD package.^[14] The analyses included the determination of all BCPs as well as all topological quantities ($\rho(\mathbf{r}_{\text{BCP}})$, $\nabla^2\rho(\mathbf{r}_{\text{BCP}})$, ε_{BCP} , λ_i) and the development of a quantification criterion of bond polarisation from the positions of the BCPs. Furthermore, the spatial Laplacian distributions as well as the CPs in the Laplacian have been determined. This unambiguously determines the hybridisation of an atom directly.

3.8.1 Quantification of Bond Polarisation

The existence of a (3,-1) BCP is a necessary condition for a diatomic bond. The BCP is located at the intersection of the bond path (line of maximum $\rho(\mathbf{r})$ with respect to any neighbouring line) and the zero flux surface given as

$$\nabla\rho(\mathbf{r}) = \mathbf{n}(\mathbf{r}) = 0, \quad (3-32)$$

where $\mathbf{n}(\mathbf{r})$ is the vector normal to the surface. The zero flux surfaces partition space to disjoint regions (basins) in $\rho(\mathbf{r})$. These basins can be related to the atomic volumes. In that respect the BCP can be assumed as a natural border on the bond path. The position of the BCP determines the 'size' of a basin in a given direction and thus the amount of charge density, which is associated to an atom. In that respect polarisation of a bond means reducing the atomic volume by shifting the BCP towards, and at the expense of, the less electronegative partner. The position of the BCP is a direct tool to quantify bond polarisation from the modelled densities, without referring to empirical concepts such as electronegativity, inductive effects of different functional groups, or bond

strength. As long as equivalent bonds are compared (S–N in this case) and the evaluation is based on the same conditions (see chapter 3.1.1.2), no model dependencies should arise and the calculated values are comparable.

For the comparison of polarisation effects a reference point has to be given. In this case it is a hypothetical non-polarised, purely covalent S–N single bond. In this hypothetical bond the S–N distance should be given by the sum of the covalent radii (1.04 Å (S), 0.70 Å (N)),^[100] which is 1.74 Å. In the frame of the topology one would expect the BCP of this bond in distances from the atoms which are given by the covalent radii.

For comparison reasons the ratio Q_h is defined as

$$Q_h = \frac{r_c(A)}{r_c(A) + r_c(B)}, \quad (3-33)$$

where r_c are the covalent radii of the atoms A and B, respectively. The ratio Q_h is 0.598 for the hypothetical S–N bond (A = S, B = N) and can be related to the values found *via* topological analyses, where Q takes the form

$$Q = \frac{d_{\text{BCP}}(\text{S})}{d_{\text{BCP}}(\text{S}) + d_{\text{BCP}}(\text{N})}. \quad (3-34)$$

d_{BCP} are the distances of the BCPs from the atomic positions. The denominator is given by the bond path length. The lower the value of Q relative to 0.598 for the hypothetical non-polarised bond is the more the bond density is polarised away from the electropositive sulfur atom towards the nitrogen atom.

For the S–C bond Q_h is 0.575 (covalent radius (C) = 0.77 Å) with a bond length of 1.81 Å.

3.8.2 Critical Points in the Charge Density Distributions

For all bonds of the compounds I–IV, including the inter- and intramolecular hydrogen bonds, respectively, all BCPs could be located and the topological parameters were determined. In addition to the lengths of the bond paths, the amount of charge density, the eigenvalues of the Hessian matrix λ_i with the associated ellipticities ε_{BCP} and the ratio of $|\lambda_1|/\lambda_3$ were determined at each BCP. For the S–E bonds (E = N, C) the ratio Q was calculated from the positions of the BCPs. The results of the CP investigations for the S–N bonds are listed in table 3–12.

Table 3-12: BCP properties of the S–N bonds in compounds I–IV. d is the bond path length [Å], d_{BCP} [Å] denotes the distances of the BCP from the sulfur atom and Q is the ratio defined before, respectively. λ_i ($i = 1, 2, 3$) [$\text{e}\text{\AA}^{-5}$] are the eigenvalues of the Hessian matrix, ε_{BCP} is the ellipticity, η_{BCP} is the ratio $|\lambda_1/\lambda_3|$, $\rho(\mathbf{r}_{\text{BCP}})$ [$\text{e}\text{\AA}^{-3}$] the charge density and $-\nabla^2 \rho(\mathbf{r}_{\text{BCP}})$ [$\text{e}\text{\AA}^{-5}$] the negative Laplacian at the BCP, respectively.

	I	II	III	IV
S1–N1: d	1.546	1.513	1.683	1.650
d_{BCP}	0.681	0.738	0.834	0.780
Q	0.44	0.49	0.50	0.47
$\rho(\mathbf{r}_{\text{BCP}})$	1.93(3)	2.27(3)	1.76(3)	1.89(3)
$-\lambda_1/-\lambda_2/\lambda_3$	9.62 / 8.99 / 9.18	14.40 / 11.83 / 15.69	10.26 / 9.66 / 11.97	11.47 / 10.32 / 8.38
$-\nabla^2 \rho(\mathbf{r}_{\text{BCP}})$	9.44(8)	10.56(8)	7.95(8)	13.41(7)
$\varepsilon_{\text{BCP}} / \eta_{\text{BCP}}$	0.07 / 1.05	0.22 / 0.92	0.06 / 0.86	0.11 / 1.37
S1–N2: d	1.531		1.585	1.530
d_{BCP}	0.788		0.769	0.718
Q	0.51		0.49	0.47
$\rho(\mathbf{r}_{\text{BCP}})$	2.24(3)		2.06(3)	2.31(3)
$-\lambda_1/-\lambda_2/\lambda_3$	12.58 / 11.73 / 14.92		12.28 / 11.32 / 10.43	13.61 / 12.41 / 9.43
$-\nabla^2 \rho(\mathbf{r}_{\text{BCP}})$	9.38(7)		13.17(9)	16.60(9)
$\varepsilon_{\text{BCP}} / \eta_{\text{BCP}}$	0.07 / 0.84		0.08 / 1.18	0.10 / 1.44
S1–N3: d				1.520
d_{BCP}				0.718
Q				0.47
$\rho(\mathbf{r}_{\text{BCP}})$				2.37(3)
$-\lambda_1/-\lambda_2/\lambda_3$				13.78 / 13.01 / 10.36
$-\nabla^2 \rho(\mathbf{r}_{\text{BCP}})$				16.44(9)
$\varepsilon_{\text{BCP}} / \eta_{\text{BCP}}$				0.06 / 1.33

The comparison of bond lengths and angles, as it was presented in chapter 3.5, leads to two principally different types of S–N bonds: ‘long’ S–N single bonds (S1–N1 = 1.6829(2) Å (**III**) / 1.6491(3) Å (**IV**)) and ‘short’ formal S=N double bonds (S=N from 1.5113(2) Å (**II**) to 1.5847(2) Å (**III**)), with gradual variations related to the oxidation state of the sulfur atom and presence or absence of hydrogen bonds.

The topological properties, which are presented in table 3–12, elucidate the atomic and bonding properties much more subtly differentiated. The analyses unearthed remarkably different properties of formally equal bonds independent from the bond length.

As already stated in chapter 3.1.2.4, have the criteria for the classification of atomic and bonding properties from the topological parameters been elaborated and tested for first-row elements excessively.^[20,111-116] For heavier elements,^[83,84] however, and especially sulfur containing compounds, the interpretation of the topology still is a challenging aim as published information on reference systems is scarce.^[27,117-119] To develop this new area it was vital to find the right benchmark systems with internal standards for various S–N bonding modes inside the same experiment and among the sample. The characteristics at the BCPs of the S–N bonds studied in this thesis are listed in table 3–12. Especially the formal double bonds present an unexpected wide range in all density related features. Even the S1–N1 single bonds in **III** and **IV** differ remarkably concerning their topology. This already demonstrates the necessity to expand the topological analyses to S–N bonds by the investigation of interconnected examples.

S–N bonds

Since the experimentally determined charge density distributions in S–N bonds have exclusively been investigated in S₄N₄ (S–N = 1.629(1) Å, $\rho(\mathbf{r}_{\text{BCP}}) = 1.54(1) \text{ e}\text{\AA}^{-3}$, $\nabla^2\rho(\mathbf{r}_{\text{BCP}}) = -10.60(3) \text{ e}\text{\AA}^{-5}$, $\varepsilon_{\text{BCP}} = 0.17$)^[27,120] and are partly based on investigations of the static deformation density distributions^[120] instead of the more reliable topological properties and for other S–N containing systems only theoretical calculations have been published (e.g. S₄N₄: S–N = 1.62 Å, $\rho(\mathbf{r}_{\text{BCP}}) = 1.282 \text{ e}\text{\AA}^{-3}$, $\nabla^2\rho(\mathbf{r}_{\text{BCP}}) = -4.941 \text{ e}\text{\AA}^{-5}$, $\varepsilon_{\text{BCP}} = 0.143$),^[119] the bonding properties of the compounds studied in this thesis have to be compared at an internal scale.

The obviously covalent S1–N1 single σ -bond in **III** can serve as an internal reference point. It displays the longest bond path of all studied S–N bonds

(1.683 Å), the lowest density (1.76(3) eÅ⁻³), and most less-negative Laplacian at the BCP (-7.95 (8) eÅ⁻⁵) with an almost negligible ellipticity of 0.06. As pointed out earlier, the bond length of 1.6829(2) Å is in the region typically quoted in the literature^[98] as a S–N single bond. The bond length seems to be a good compromise between the mean S–N bond length from the CSD (1.65 Å) and the sum of the covalent radii (1.74 Å). The η -value of 0.86, which is considerably smaller than 1, indicates ionic contribution in the S1–N1 bond in **III** (see chapter 3.1.2.4). This is further substantiated by the Q value lower than 0.598. Compared to the other S–N bonds, the Q of 0.50 is at the upper, while η is at the lower limit of the range covered by both features. This suggests η to be a suitable indicator for bond strength but not to specify covalent or ionic bonding. In that respect the Q value can serve as an internal standard for a S–N single bond, although electron density might be drained by the intermolecular hydrogen bond in (**III**). This possibly increases the polarity of the S–N single bond.

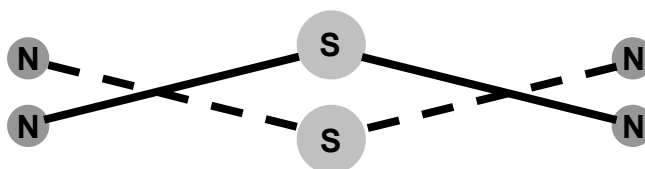
It has to be emphasised that for the interpretation of topological parameters such as the η -value, small molecules with well known physical and chemical properties were studied^[1] (e.g. ethane, benzene, ethylene). However, the density features determined in this thesis should not be compared directly and without the context to those model systems. Different to the small carbohydrates all S–N density distributions in this thesis are - sometimes extremely - polarised (Q , d) and some of the bonds show features characteristically for multiple bonding (ϵ , λ_i), as well as for a mixed ionic/shared interactions (ρ , $-\nabla^2\rho$). Therefore the objective criteria presented in this thesis have to be ranked internally rather than to be compared to other molecules composed of elements from the second period. In that respect no absolute characterisation derived directly from the topological properties can be provided. However, the internal ranking, together with additional information such as density distributions and the spatial distributions of the negative Laplacian, provides substantial insight to the S–N bonding beyond the limited methodology of bond theory in carbon chemistry.

Compared to the standard single bond S1–N1, the density and the negative Laplacian at the BCP of S1=N2 are higher (2.06(3) eÅ⁻³, -13.17(9) eÅ⁻⁵) for the formal double bond in **III**. The η -value of 1.18 is a sign of increased bond strength. The low ellipticity of 0.08 is given by the relatively distinct, but almost equal contractions of the density perpendicular to the bond path ($\lambda_1 = -10.28$

$e\text{\AA}^{-5}$, $\lambda_2 = -11.32 e\text{\AA}^{-5}$). This does not support the formulation of a double bond for S1–N2. The contraction towards the nuclei, given by λ_3 ($10.43 e\text{\AA}^{-5}$), indicates a flat minimum of the density along the bond path.

The closest approximation to a classical double bond is found in $S(\text{N}^t\text{Bu})_3$ (II). The density at the BCP of $2.27(3) e\text{\AA}^{-3}$ is the highest found at all thirteen studied S–N bonds. The same holds for the remarkably pronounced ellipticity of 0.22. These dramatic changes clearly are not reflected in the marginal bond shortening of only 0.07\AA of the S–N bonds in II compared to S1–N2 in III. Furthermore, the polarisation features of both bonds are similar. The high ellipticity in II is caused by strong contractions perpendicular to the bond path, while λ_1 ($-14.40 e\text{\AA}^{-5}$) is much more distinct than λ_2 ($-11.83 e\text{\AA}^{-5}$). Although η of 0.92 indicates a weaker bond in II than the S1–N2 bond in III, the first is closer to the concept of a double bond than the latter.

At this point of the discussion the already mentioned out-of-plane disorder in II has to be taken into account. Since this disorder can not be handled in the least squares procedure, the refined density displays the mean distribution. Therefore the extension of bonding density perpendicular to SN_3 plane and by that the high ellipticity may be increased by the disorder as clarified by scheme 3–2.



Scheme 3-2: Schematic representation of the out-of-plane disorder of the SN_3 unit in II.

It is not the S1–N2 bond in III, but the S1–N2 bond in $S(\text{N}^t\text{Bu})_2$ (I), which is similar to the double bonds in II. For the only 0.016\AA longer and slightly less polarised bond an almost identical value of $2.24(3) e\text{\AA}^{-3}$ for $\rho(\mathbf{r}_{\text{BCP}})$ is detected. Similarly, a deep density minimum along the bond path is observed but the perpendicular contractions are smaller ($\lambda_1 = -12.58 e\text{\AA}^{-5}$, $\lambda_2 = -11.73 e\text{\AA}^{-5}$) and, even more striking, they are almost equal in value, which leads to an ellipticity of only 0.07. This is much too small for an anticipated double bond considering the small η -value of 0.84. The comparison of the formally equivalent S1–N1 bond in I leads to even more astonishing results. Again, the dramatic change in the topological parameters is certainly not reflected by the bond elongation of only 0.015\AA . The bond seems to be extremely polarised ($Q = 0.44$) with low

density at the BCP ($1.93(3) \text{ e}\text{\AA}^{-3}$), which is closer to the value of the standard single bond in **III** than to the second S–N bond in **I**. Similarly low are the eigenvalues of the Hessian matrix. Although the algebraic sum $\nabla^2\rho(\mathbf{r}_{\text{BCP}})$ of $-9.44(8) \text{ e}\text{\AA}^{-5}$ is almost identical to that at the BCP of S1–N2, the contractions perpendicular to the bond path ($\lambda_1 = -9.62 \text{ e}\text{\AA}^{-5}$, $\lambda_2 = -8.99 \text{ e}\text{\AA}^{-5}$) are even smaller than in the S1–N1 single bond of **III**, indicating reduced shared interaction. This is accompanied by a low degree of density contraction (flat minimum) parallel to the bond path ($\lambda_3 = 9.18 \text{ e}\text{\AA}^{-5}$) and an almost vanishing ellipticity of 0.07. The slightly larger than unity η -value suggests bond strength between these of the formal double bonds in **II** and **III**, respectively. The remarkable features of the S1–N1 in **I** will be discussed on the basis of the Laplacian in chapter 3.8.4.1.

IV is an exceptional molecule, as the topological characteristics of the three different S–N bond modes can be discussed on the basis of the same experiment. Both formal S–N double bonds are almost equal concerning bond lengths, densities ($2.31(3) \text{ e}\text{\AA}^{-3}$ (S1–N2), $2.37(3) \text{ e}\text{\AA}^{-3}$ (S1–N3)) and negative Laplacian at the BCPs ($-16.60(9) \text{ e}\text{\AA}^{-5}$ (S1–N2), $-16.44(9) \text{ e}\text{\AA}^{-5}$ (S1–N3)), respectively. Even the relations between the λ_i are comparable, which indicate distinct contraction perpendicular ($\lambda_1 = -13.61 \text{ e}\text{\AA}^{-5}$, $\lambda_2 = -12.41 \text{ e}\text{\AA}^{-5}$ (S1–N2), $\lambda_1 = -13.78 \text{ e}\text{\AA}^{-5}$, $\lambda_2 = -13.01 \text{ e}\text{\AA}^{-5}$ (S1–N3)) and a flat minimum parallel to the bond path ($\lambda_3 = 9.43 \text{ e}\text{\AA}^{-5}$ (S1–N2), $\lambda_3 = 10.36 \text{ e}\text{\AA}^{-5}$ (S1–N3)). The slight differences can be assigned to the fact that N2 is an intramolecular hydrogen bond donor with H4 as the acceptor. This causes charge transfer from the S–N bonding region towards the nitrogen atom. The high η -values of 1.44 and 1.33 indicate as well the presence of strong double bonds in **IV**. In contrast the ellipticities of 0.10 and 0.06 are even smaller than ε_{BCP} of the S–N(H) single bond in **IV** (0.11).

The S1–N1 single bond in **IV** shows the same polarisation as the two formal double bonds ($Q = 0.47$) and differs in its topological properties from the S1–N1 standard single bond in **III**. The density at the BCP of $1.89(3) \text{ e}\text{\AA}^{-3}$ is relatively high (almost the same as at the formal double bond S1–N1 in $\text{S}(\text{N}^t\text{Bu})_2$ (**I**)). Compared to S1–N1 in **III**, the absolute value of the negative Laplacian ($13.41(7) \text{ e}\text{\AA}^{-5}$) and the η -value (1.37) are much higher. The prominent negative Laplacian is the consequence of a very weak parallel contraction of the density towards the nuclei, while the contractions perpendicular to the bond path are more prominent.

In conclusion from the comparison of the topological properties of the S–N bonds, there is no evident set of features to be assigned to a single or a double bond. Most obvious are the indications for the anticipated pronounced polarity of the bonds and the absence of a classical double bond. This will further be elucidated in chapter 3.8.4.

S–C bonds

Both S–C bonds studied in this thesis are in good agreement. In the light of the values found for S–N, the absolute values of the topological properties are not unexpected, although they do not adopt the same characteristics as the few examples of comparable S–C bonds quoted in the literature.^[81,107,121] This is not unexpected, since exclusively in I-cystine^[81] the S–C bonding is comparable, while in the BTDMTTF-TCNQ complex^[107] (bis(thiodimethylene)-tetrathiafulvalene tetracyanoquinodimethane, $C_{10}H_8S_6^+ \cdot C_{12}H_4N_4^-$) the sulfur atom is part of a ring system or like in the [Nit(SMe)Ph] radical^[121] bonded to such one. Therefore only to one of the two S–C bonds in [Nit(SMe)Ph] is referred. The results of the topological analyses of the S–C bonds in **III** and **IV** are presented in table 3–13, together with comparable values found in the literature.

Table 3-13: BCP properties of the S–C bonds in **III**, **IV** and some examples from the literature. d is the bond path length [Å], d_{BCP} [Å] denotes the distances of the BCP from the sulfur atom and Q is the ratio defined in 3.8.1. λ_i ($i = 1, 2, 3$) [$e\text{Å}^{-5}$] are the eigenvalues of the Hessian matrix, ε_{BCP} is the ellipticity, η_{BCP} the ratio $|\lambda_1|/\lambda_3$, $\rho(\mathbf{r}_{\text{BCP}})$ [$e\text{Å}^{-3}$] the charge density and $-\nabla^2\rho(\mathbf{r}_{\text{BCP}})$ [$e\text{Å}^{-5}$] the negative Laplacian at the BCP, respectively.

	III	IV	I-cystine	Nit(SMe)Ph^{a,b}
d	1.791	1.817	1.818	1.802
d_{BCP}	0.994	0.984	0.971	0.948
Q	0.55	0.54	0.53	0.53
S–C: $\rho(\mathbf{r}_{\text{BCP}})$	1.54(2)	1.45(2)	1.21	1.23
$-\lambda_1/-\lambda_2/\lambda_3$	9.18 / 8.72 / 9.20	8.69 / 7.95 / 8.64	6.82 / 6.23 / 7.37	–
$-\nabla^2\rho(\mathbf{r}_{\text{BCP}})$	8.70(5)	8.01(4)	5.68	5.42
$\varepsilon_{\text{BCP}} / \eta_{\text{BCP}}$	0.05 / 1.00	0.09 / 1.01	0.09 / 0.93	0.11 / –

a) [Nit(SMe)Ph] = *p*-(methylthio) phenyl nitronyl nitroxide

b) exclusively the S–Me bond is listed

Although the bond lengths (1.7907(2) Å in **III**, 1.8162(3) Å in **IV**) are at the upper limit of the range covered by S–C single bonds already studied by charge density analysis, the densities and the negative Laplacian at the BCP are relatively high in the absolute value ($\rho(\mathbf{r}_{\text{BCP}}) = 1.54(2) \text{ e}\text{\AA}^{-3}$, $-\nabla^2\rho(\mathbf{r}_{\text{BCP}}) = 8.70(5) \text{ e}\text{\AA}^{-5}$, $\varepsilon_{\text{BCP}} = 0.05$ (**III**) and $\rho(\mathbf{r}_{\text{BCP}}) = 1.45(2) \text{ e}\text{\AA}^{-3}$, $-\nabla^2\rho(\mathbf{r}_{\text{BCP}}) = 8.01(4) \text{ e}\text{\AA}^{-5}$, $\varepsilon_{\text{BCP}} = 0.09$ (**IV**)). This is even more remarkable, since the ellipticities are equal or less pronounced and therefore multiple bonding or π -contribution effects should be ruled out.

Those findings are consistent to an internal comparison, as the shorter S–C bond in **III** bears the higher density than its counterpart in **IV**. The η -values are with 1.00 and 1.01 comparable to the value in l-cystine (0.93). The higher values should be assigned to slightly increased bond strengths. The S–C bonds should be classified as (polarised) covalent σ -bonds. Although the bond lengths are close to the sum of the covalent radii, the Q-values indicate bond polarisation from S to C (0.55 (**III**), 0.54 (**IV**)). The polarisation is slightly more pronounced for the longer bond in **IV**.

From further discussion of the S–C bonding properties is abstained, since too few examples are present. However, a general finding of this thesis is, that in the studied sulfur-element bonds the densities and the sum of the eigenvalues of the Hessian matrix are systematically increased compared to published S–N or S–C bonds. No straightforward correlation to the oxidation state of the sulfur atom, the bonding partner, and the bonding type can be detected.

N–C and C–C bonds

The topological features of the N–C and C–C BCPs are compared with respect to their orientation relative to the nitrogen lone-pairs and the C–N–S–N–C backbones, because of the significant differences of the bond angles in the N^tBu groups already discussed in chapter 3.5. The results are composed in table 3–14.

Although the values found for the N–C bonds are in the expected range,^[122] they vary of approximately $0.15 \text{ e}\text{\AA}^{-3}$ for $\rho(\mathbf{r}_{\text{BCP}})$ and $2.5 \text{ e}\text{\AA}^{-5}$ for $\nabla^2\rho(\mathbf{r}_{\text{BCP}})$. Obviously, the topological parameters in the N-bonded ^tBu groups are biased by the S–N bonds. The densities at the BCPs in the N–C bonds, which are formally double bonded to the sulfur, are systematically higher and vary from $1.771(10) \text{ e}\text{\AA}^{-3}$ in **I** to $1.874(11) \text{ e}\text{\AA}^{-3}$ in **III**.

Table 3-14: BCP properties of the N–C and C–C bonds in **I–IV**. $\rho(\mathbf{r}_{\text{BCP}})$ [$\text{e}\text{\AA}^{-3}$] is the charge density and $-\nabla^2\rho(\mathbf{r}_{\text{BCP}})$ [$\text{e}\text{\AA}^{-5}$] the negative Laplacian at the BCP. Due to symmetry restrictions during the refinements for **I** only one ^tBu group and for **IV** only one moiety are listed.

		I	II	III	IV
N1–C1:	$\rho(\mathbf{r}_{\text{BCP}})$	1.771(10)	1.729(5)	1.842(11)	1.767(6)
	$-\nabla^2\rho(\mathbf{r}_{\text{BCP}})$	11.54(3)	7.68(2)	12.39(4)	10.24(2)
N2–C2:	$\rho(\mathbf{r}_{\text{BCP}})$	1.879(11)		1.874(11)	1.853(6)
	$-\nabla^2\rho(\mathbf{r}_{\text{BCP}})$	11.28(4)		9.76(4)	11.09(2)
N3–C3:	$\rho(\mathbf{r}_{\text{BCP}})$				1.852(6)
	$-\nabla^2\rho(\mathbf{r}_{\text{BCP}})$				10.62(2)
C1–C11:	$\rho(\mathbf{r}_{\text{BCP}})$	1.760(6)	1.718(4)	1.735(6)	1.761(4)
	$-\nabla^2\rho(\mathbf{r}_{\text{BCP}})$	12.38(2)	10.56(2)	11.05(2)	12.16(2)
C1–C12:	$\rho(\mathbf{r}_{\text{BCP}})$	1.642(6)	1.759(4)	1.737(6)	1.781(4)
	$-\nabla^2\rho(\mathbf{r}_{\text{BCP}})$	11.53(2)	10.99(2)	11.05(2)	12.31(2)
C1–C13:	$\rho(\mathbf{r}_{\text{BCP}})$	1.719(6)	1.754(4)	1.754(6)	1.754(4)
	$-\nabla^2\rho(\mathbf{r}_{\text{BCP}})$	12.01(2)	10.89(2)	11.27(2)	11.84(2)
C2–C21:	$\rho(\mathbf{r}_{\text{BCP}})$	1.662(6)		1.725(6)	1.794(4)
	$-\nabla^2\rho(\mathbf{r}_{\text{BCP}})$	11.10(2)		10.94(2)	12.64(2)
C2–C22:	$\rho(\mathbf{r}_{\text{BCP}})$	1.676(6)		1.730(6)	1.804(4)
	$-\nabla^2\rho(\mathbf{r}_{\text{BCP}})$	11.41(2)		10.95(2)	12.93(2)
C2–C23:	$\rho(\mathbf{r}_{\text{BCP}})$	1.695(6)		1.700(6)	1.745(4)
	$-\nabla^2\rho(\mathbf{r}_{\text{BCP}})$	11.57(2)		10.02(2)	11.84(2)
C3–C31:	$\rho(\mathbf{r}_{\text{BCP}})$				1.746(4)
	$-\nabla^2\rho(\mathbf{r}_{\text{BCP}})$				11.52(2)
C3–C32:	$\rho(\mathbf{r}_{\text{BCP}})$				1.760(4)
	$-\nabla^2\rho(\mathbf{r}_{\text{BCP}})$				11.78(2)
C3–C33:	$\rho(\mathbf{r}_{\text{BCP}})$				1.748(4)
	$-\nabla^2\rho(\mathbf{r}_{\text{BCP}})$				11.73(2)

However, the density in **II** of $1.729(5) \text{ e}\text{\AA}^{-3}$ is even smaller than at the formally single bonded $\text{N}(\text{H})\text{tBu}$ in **IV** ($1.767(6) \text{ e}\text{\AA}^{-3}$) as well as in **III** ($1.842(11) \text{ e}\text{\AA}^{-3}$). This small value in **II** corresponds to only $-7.68(2) \text{ e}\text{\AA}^{-5}$ in $\nabla^2 \rho(\mathbf{r}_{\text{BCP}})$, which is the least negative Laplacian found in the N–C bonds.

Striking is the difference between the two NtBu groups in **I**: $\rho(\mathbf{r}_{\text{BCP}})$ in N2–C2 adopts the largest value observed in all compounds, while the density found in the N1–C1 is at the lower limit of the range. A comparison with table 3–12 shows correlations between $\rho(\mathbf{r}_{\text{BCP}})$ and $\nabla^2 \rho(\mathbf{r}_{\text{BCP}})$ in the S–N and N–C bonds. The reduced density at the BCP of N1–C1 might be caused by the orientation of the tBu group at the same side as the lone-pair at S1.

The C–C bonds reveal features in $\rho(\mathbf{r}_{\text{BCP}})$, which can partly be related to the orientation of the bonds relative to the assumed sp^2/sp^3 lone-pair densities at the nitrogen atoms. If the methyl groups are oriented towards nitrogen lone-pairs a density reduction in this bonds is observed (C12, C13, C21 in **I** and C11 in **II**). The density depletion is more pronounced at the in-plane oriented methyl groups C21 in **I** and C11 in **II**. This supports the assumption of an interaction of the C–C bonds with the lone-pair densities at the nitrogen atoms.

In **III** and **IV** the correlations are not as obvious. As mentioned before (chapter 3.5), their C–N–S–N–C backbones are distorted from planarity. Apart from that, hydrogen bonds and the steric strain within those compounds may counterbalance the small density variations observed in **I** and **II**. Nevertheless, marginal differences are observed in **III**, where C1–C11 and C2–C21 show a reduced $\rho(\mathbf{r}_{\text{BCP}})$, as they are oriented towards the lone-pair density (sp^3 for N1) of the next nitrogen atom. However, the argument remains weak, as the density at the C1–C12 bond is identical with C1–C11 within one esd and this methyl group definitely does not point towards any lone-pair. For the formally double bonded NtBu groups in **III** all $\rho(\mathbf{r}_{\text{BCP}})$ of the C–C bonds were found to be smaller than those in the singly bonded. The lowest density was found at the BCP of C2–C23 with $1.700(6) \text{ e}\text{\AA}^{-3}$. At first sight this seems confusing, as the lowest value is expected at the C2–C21 bond, since this points in-plane towards the lone-pair of the presumably sp^2 hybridised nitrogen atom N2. The topic will be discussed again and explanation is provided *vide infra* in chapter 3.8.4, where the spatial lone-pair distribution is determined experimentally.

Even more than in **III**, the electron density features in **IV** should be dominated by steric hindrance of the bulky tBu groups. The connection of two sterically

demanding $S(N^tBu)_3$ moieties by a methylene bridge and the presence of two intramolecular $N-H\cdots N$ hydrogen bonds causes energetically disfavoured proximity. Due to steric strain it is not possible to correlate the densities determined at the BCPs directly to the geometrical parameters.

Density related bond angles

In addition to the topological features, the positions of the BCPs facilitate the direct determination of density related bond angles (table 3–15).

Table 3-15: Selected bond angles [°] calculated from the BCPs for compound I-IV. For II exclusively the angles of one tBu group and for IV the values of one $S(N^tBu)_2(NH^tBu)$ moiety due to the molecular symmetry are presented.

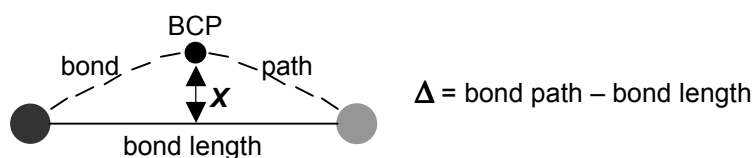
compound	I	II	III	IV
formula	$S(N^tBu)_2$	$S(N^tBu)_3$	$H(N^tBu)_2SMe$	$CH_2\{S(N^tBu)_2(NH^tBu)\}_2$
CP(N1)–S1–CP(N2):	116.4	120.1	110.8	110.5
CP(N1)–S1–CP(N3):		119.9		105.0
CP(N2)–S1–CP(N3):		119.9		122.8
CP(N1)–S1–CP(C_{methyl(ene)}):			100.6	104.4
CP(N2)–S1–CP(C_{methyl(ene)}):			102.4	102.3
CP(N3)–S1–CP(C_{methyl(ene)}):				110.6
CP(S1)–C–CP(S2):				119.5
CP(S1)–N1–CP(C1):	115.1	123.1	117.3	124.6
CP(S1)–N2–CP(C2):	123.0		111.3	118.1
CP(S1)–N3–CP(C3):				122.0
CP(N1)–C1–CP(C11):	112.5	105.4	107.5	105.9
CP(N1)–C1–CP(C12):	107.7	111.2	110.8	110.4
CP(N1)–C1–CP(C13):	107.2	109.8	110.1	111.4
CP(N2)–C2–CP(C21):	106.9		108.4	112.6
CP(N2)–C2–CP(C22):	108.2		111.9	108.3
CP(N2)–C2–CP(C23):	110.3		111.0	108.8
CP(N3)–C3–CP(C31):				112.2
CP(N3)–C3–CP(C32):				106.1
CP(N3)–C3–CP(C33):				110.4

Since the BCPs are located on the bond paths, which represents the course of the bonding density, angles determined from the BCPs should lead to meaningful bond angles rather than values calculated from the direct connectivity lines between nuclear positions.

If the values presented in table 3–15 are compared to those of table 3–5 and table 3–8, the differences are striking. All angles at the formally double bonded nitrogen atoms are smaller if the BCPs are used for their calculation. As a consequence, the BCP-deduced geometrical properties do not suggest the wider bond angles expected for a sp^2 hybridised nitrogen atom, like the connectivity deduced data propose. Most of the bond angles at the central sulfur atoms, nitrogen atoms, and tertiary carbon atoms are closer to tetrahedral angles. It is obvious that electronical properties like the hybridisation of atoms or their bond orders should only be deduced from *density related* geometrical features and not from standard structure determinations. Those might be biased from conceptional self-fulfilling prophecies like tetrahedral orientation of sp^3 orbitals.

Bond path analyses

For testing purposes the S–E (E = N, C) bond paths were subject to an examination *via* an Euler second order numerical integration technique. During this routine $\nabla\rho(\mathbf{r})$ is integrated from the BCP towards the bonded atoms by extrapolating the gradient from neighboured steps. This calculation provides the bond path length, which is always longer than the bond length, and the distance of the BCP from the direct connection line between the two atoms. If both lengths differ significantly and the BCP distance from the straight line is notable, the bond is strained.^[123] The shifts of the BCPs from the direct connection line between the atoms are the quantitative criteria for sterical strain.



Scheme 3-3: Definition of bond path characteristics.

For all bonds presented in table 3–16, the BCP is located some hundredth of an Ångström off the direct connection line indicating slight strain in the bonds. The strain is more distinct in the formal double bonds than in the S–N and S–C single bonds, respectively. It should be pointed out, that the shifts of the BCPs

away from the direct connection lines of the atoms are not induced by the refinement procedure. From the atom model used during multipole refinement, no hybridisation state was assumed. This enhances the physical and chemical significance of the positions of the BCPs and the angles calculated from them. Since almost all BCP shifts result in angles closer to tetrahedral coordination, this is a strong and reliable indicator for the sp^3 hybridisation of the nitrogen atoms, precluding double bonds.

Table 3-16: Bond path characteristic of the S–E (E = N, C) bonds in compounds **I–IV**. The first value denotes $X [10^{-2} \text{ \AA}]$, the second is $\Delta [10^{-2} \text{ \AA}]$, as defined in scheme 3–3.

compound	I	II	III	IV
formula	$S(N^tBu)_2$	$S(N^tBu)_3$	$H(N^tBu)_2SMe$	$CH_2\{S(N^tBu)_2(NH^tBu)\}_2$
S1–N1:	3.91 / 0.42	2.78 / 0.16	1.66 / 0.10	2.12 / 0.26
S1–N2:	4.74 / 0.80		2.25 / 0.21	4.23 / 0.43
S1–N3:				3.81 / 0.38
S1–C_{methyl(ene)}:			1.37 / 0.07	2.03 / 0.09

Since the differences between the bond path lengths and the straight connection lines are only marginal, the bond lengths do not have to be corrected and the values given in table 3–5 and table 3–8 can be used for the discussion of bond distances without restrictions.

Hydrogen bonds

In addition to the search of (3,-1) BCPs in $\rho(\mathbf{r})$, concerning all direct chemical bonds, the inter- or intramolecular hydrogen bonds in **III** and **IV** were investigated.

The BCP search in **III** led to the localisation of an intermolecular (3,-1) BCP in a distance $d_{BCP}(H1)$ of 0.746 Å from H1 ($H1 \cdots N2 = 2.0271(2)$ Å), a density $\rho(\mathbf{r}_{BCP})$ of 0.162 e\AA^{-3} and a positive Laplacian $\nabla^2\rho(\mathbf{r}_{BCP})$ of 2.154 e\AA^{-5} . In **IV** two intramolecular hydrogen bonds could be identified by localisation of two (3,-1) BCPs between $H1 \cdots N5$ ($d_{BCP}(H1) = 0.807$ Å, $H1 \cdots N5 = 2.1568(3)$ Å, $\rho(\mathbf{r}_{BCP}) = 0.131 \text{ e\AA}^{-3}$, $\nabla^2\rho(\mathbf{r}_{BCP}) = 1.871 \text{ e\AA}^{-5}$) and $H4 \cdots N2$ ($d_{BCP}(H4) = 0.793$ Å, $H4 \cdots N2 = 2.1379(3)$ Å, $\rho(\mathbf{r}_{BCP}) = 0.131 \text{ e\AA}^{-3}$, $\nabla^2\rho(\mathbf{r}_{BCP}) = 1.871 \text{ e\AA}^{-5}$), respectively. The topological properties – low density values and a slightly positive Laplacian at

the BCP – are almost the same for the inter- and intramolecular hydrogen bonds. They are in the expectation range for closed shell interactions with hydrogen participation, although hydrogen bonds studied by experimental charge density determination quoted in literature are mostly of the E–H...O type (E = C, N, O).^[115,124-126]

For the calculated topological properties of the hydrogen bonds no esds are given (although they are calculated by the program XDPROP), since the values of $\rho(\mathbf{r}_{\text{BCP}})$ are in the range of the residual densities and therefore at the limit of the experimental resolution. The calculated esds are suspected to be underestimated.

The presence of hydrogen bonds results in intermolecular ring formation in **III** and intramolecular ring formation in **IV**. The related (3,+1) ring critical points were determined. In **IV** two (3,+1) RCPs are located in two six-membered rings, each made up from the two sulfur and two facing nitrogen atoms, the bridging CH₂ carbon atom and the single hydrogen atom, respectively. In **III** one (3,+1) RCP was found, which is located in the centre of the ring made up by two facing SN₂H units of adjacent molecules, which are related by a centre of inversion.

S...S interactions

Due to the very short distances between the sulfur atoms of two neighbouring molecules in the solid state structure of **I** (3.5663(5) Å), which is about 0.13 Å shorter than the sum of the van der Waals radii,^[100] a CP search was performed in the intermolecular region between the two sulfur atoms. Almost at the centre of the connection line ($d_{\text{BCP}}(\text{S1}) = 1.786 \text{ Å}$) a (3,-1) BCP was found, which reveals a very small density of 0.053 eÅ^{-3} and a positive Laplacian of 0.57 eÅ^{-5} . Again, no esds are given, since the value of $\rho(\mathbf{r}_{\text{BCP}})$ is lower than the experimental resolution.

S...S interactions have been investigated by topological analyses before.^[27,117-119,127] An intramolecular S...S bond in S₄N₄ was classified as a weak closed shell interaction.^[27] The longer of two slightly different S...S distances there was 2.599 Å, which is almost one Ångström shorter than the related distance in S(N^tBu)₂ (**I**). Consequently, it is not surprising that both, the density $\rho(\mathbf{r}_{\text{BCP}})$ and the Laplacian $\nabla^2\rho(\mathbf{r}_{\text{BCP}})$ at the S...S vector in S₄N₄ are much higher and were determined to be $0.37(1) \text{ eÅ}^{-3}$ and $1.61(1) \text{ eÅ}^{-5}$, respectively.

However, in a study of 3,3,6,6-tetramethyl-S-tetrathiane the intramolecular S...S distance is 2.023 Å,^[118] hence much smaller than in S₄N₄, but the $\rho(\mathbf{r}_{\text{BCP}})$ value is only 0.043(1) eÅ⁻³ and even lower than the density at the BCP found in I.

Despite all the ambiguities caused by interpretations at the resolution limit, a weak S...S interaction in the solid state structure of the S(N^tBu)₂ is present, since a (3,-1) BCP is found at the anticipated position and the amount of density is in the expectation range.

3.8.3 Bond Orders from the Topology

As outlined in chapter 3.1.2.4 the bond order can be estimated from $\rho(\mathbf{r}_{\text{BCP}})$ by application of the equation

$$n = \exp[A(\rho(\mathbf{r}_{\text{BCP}})-B)].$$

It is strictly valid exclusively for non-polar homonuclear bonds, which is obviously not the case in the compounds studied in this thesis. Nevertheless, the estimated empirical bond orders may help to understand the bonding and can serve as a rough guide.

The main problem here is the lack of two bonds of known bond order and $\rho(\mathbf{r}_{\text{BCP}})$ for the calibration of the empirical variables *A* and *B*, respectively. *B* can be determined from the known bond order of one from S1–N1 in III (*n* = 1, $\rho(\mathbf{r}_{\text{BCP}})$ = 1.76(3) eÅ⁻³). This leads to *B* = -1.76 eÅ⁻³. Since no experimental values for the determination of *A* are available due to the unknown bond orders, theoretically obtained values were employed.

In our group theoretical studies were performed parallel to the experiments. DFT calculations using GAUSSIAN 98^[128] were accomplished on S(NMe)₃ as a model compound for S(N^tBu)₃. The bond order is calculated to be 1.33 for the S–N bonds if the NRT (Natural Resonance Theory) method^[129] is used and 1.56 if the Bader formalism (AIM) is applied, respectively.^[130] Assuming that the bond orders of the S–N bonds in the sulfurtriamide do not differ significantly from those in the model compound S(NMe)₃, the variable *A* can be calculated with the experimental $\rho(\mathbf{r}_{\text{BCP}})$ value of 2.27 eÅ⁻³ in II. *A* was calculated to 0.559 e⁻¹Å³ (NRT), or 0.872 e⁻¹Å³ (AIM), respectively.

Table 3-17 compiles remarkable results. If the NRT-values are used, all estimated bond orders are very small on first sight, the more since all S–N bonds but the S1–N1 bonds of III and IV, respectively, are usually formulated as

double bonds. Clearly, this is caused by the use of a bond order of 1.33 as the reference point and all calculated n -values have to be assessed with respect to this standard.

Table 3-17: Empirically determined bond orders n of the S–N bonds in compounds **I–IV**.

compound	I	II	III	IV
formula	$S(N^tBu)_2$	$S(N^tBu)_3$	$H(N^tBu)_2SMe$	$CH_2\{S(N^tBu)_2(NH^tBu)\}_2$
n (S1–N1): NRT / AIM	1.10 / 1.16	1.33 / 1.56	1.00 / 1.00	1.08 / 1.12
n (S1–N2): NRT / AIM	1.31 / 1.52		1.18 / 1.30	1.36 / 1.62
n (S1–N3): NRT / AIM				1.41 / 1.70

The bond orders of the two formally equivalent S–N bonds in **I** differ substantially with n -values of 1.10 and 1.31. As already indicated by the other topological features, the S1–N1 bond lies in the range of the reference single bond, while the S1–N2 related value is close to that of the reference bond in $S(N^tBu)_3$ (**II**). In **IV** one formal single bond ($n = 1.08$, S1–N1) and two formal double bonds with even slightly higher n -values (1.36 and 1.41) than those of the reference are determined. Compared to that, the bond order of the formal double bond S1–N2 (1.18) in **III** is relatively small. Its n -value is nearly exactly half-way between that of the S1–N1 single bond and the reference from the sulfurtriiimide.

An internal ranking of the bond orders and the associated strengths gives the highest values for the two formal double bonds in $CH_2\{S(N^tBu)_2(NH^tBu)\}_2$ (**IV**), followed by the three equivalent S–N bonds in the sulfurtriiimide (**II**), and the S1–N2 bond in the sulfurdiimide (**I**). Of average bond order and strength are the formal double bonds in $H(N^tBu)_2SMe$ (**III**) and the S1–N1 bond in the sulfurdiimide (**I**), which are remarkably close to the reference of the single bond in **III** and particularly to the S1–N1 in $CH_2\{S(N^tBu)_2(NH^tBu)\}_2$ (**IV**).

If the bond orders are calculated on the basis of the AIM approach, the situation is different on absolute scale, but the internal relations are equivalent. The absolute values are closer to those expected from widely used concepts, as n for the formal double bonds is calculated up to 1.70 (S1–N3 in **IV**). Regardless to the absolute scale, this concept of bond orders is limited anyway, since the criterion is strictly valid only for non-polar homonuclear bonds.

All features presented for the characterisation of bonding properties include uncertainties resulting from model dependencies ($\Delta\rho_{\text{static}}$), limited validity (n, η), or unknown reference points ($\rho(\mathbf{r}_{\text{BCP}})$, $-\nabla^2\rho(\mathbf{r}_{\text{BCP}})$, ε_{BCP} , λ_i). Therefore the Laplacian distributions, which elucidate atomic and bonding properties without all these restrictions, are presented in detail for all compounds in the following chapters.

3.8.4 Laplacian Distributions

If the density distribution around and between atoms is the subject of interest, the Laplacian distribution is the most powerful analytical method, since it is independent from any reference state and exhibits very small changes in the ED due to its calculation from second order derivatives of $\rho(\mathbf{r})$. The representation of the Laplacian shows the shell structure of the atoms and its spatial distribution shows the lone-pair presence and orientation. Furthermore, it permits to judge on the nature of bonding (e.g. closed shell vs. shared interaction). It reveals areas of charge concentrations and depletions and plays the key role in this thesis, especially to answer the question of major interest: are the sulfur nitrogen interactions of the S^+-N^- type or should they be described as S=N double bonds with d-orbital participation or as sigma bonded SN_x backbones with additional π -electron delocalisation by employment of non-hybridised p- or even d-orbitals?

A recent study by Tafipolsky et al. showed the capability of the method for the classification of density delocalisation in some carbenes and their complexes.^[23] For the compounds presented here, the classification is not that straightforward, since no gradual differences in known bonding modes are under study. In this thesis the principal nature of the S,N interaction is in question. The following list summarises the prerequisites:

- lack of charge concentration above or below the sigma bond allows two S–N modes: S^+-N^- with concentrations exclusively near the atomic positions or in lone-pair regions and S–N sigma bonds exclusively.
- for **III** and **IV** the tetrahedral arrangement around the sulfur atoms allows two S–N bonding modes: S^+-N^- or S=N with participation of d-orbitals
- the planarity of the SN_x cores in **I** and **II** adds a new tentative bonding mode to both already mentioned: π -delocalisation might occur *via* parallel aligned p-

orbitals. In that case no severe charge concentrations should be observed above and below the SN_x planes.

To answer those questions, the Laplacian distributions have been investigated excessively. All bonds and the atomic properties of the most interesting atoms (S, N, sulfur bonded C atoms) have been studied by calculation of the Laplacian distribution in planes (bonds) and cubes (atoms). The spatial distributions around the nitrogen atoms were investigated for the existence of (3,-3) CPs in the negative Laplacian. The orientation of the lone-pairs derived from this procedure was determined and the angles with lone-pair participation were calculated.

Furthermore, the isosurface defined by the zero-value of the Laplacian (reactive surface) was calculated. It visualises areas of relative charge depletions and indicates the most probable directions for a nucleophilic attack.

3.8.4.1 Laplacian Distribution in I

The Laplacian distribution in I confirmed both, expected and unexpected bonding features. All bonding densities are contracted perpendicular to the bond paths and reveal non-vanishing charge density concentrations in the internuclear regions, which is typical for shared interactions.

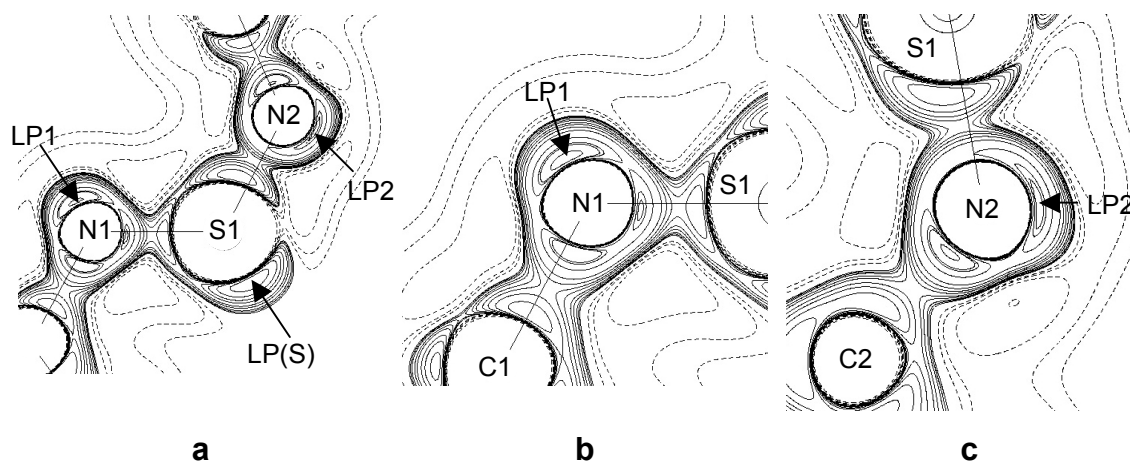


Figure 3-11: Contour plots of the Laplacian $\nabla^2\rho(\mathbf{r})$ in I displaying charge concentrations in the N1-S1-N2 (a), LP1-N1-S1 (b) and LP2-N2-S1 plane (c), respectively. Negative values (concentrations) are marked by solid lines, positive values by dashed lines, respectively. Maxima of the non-bonding VSCCs (lone-pairs) are labelled LP.

At the central sulfur atom, as well as at both nitrogen atoms, non-bonding valence shell charge concentrations (VSCCs) are found (Figure 3-11). At the nitrogen atoms they were identified as local minima in the Laplacian. Their

positions are almost in plane with respect to the mean C1–N1–S1–N2–C2 plane, as the angles of the lone-pair (LP) connections to the nitrogen atoms with the S–N–C planes are very small (0.9° N1, 13.3° N2). The maxima of the non-bonding VSCCs at the nitrogen atoms are both oriented towards the sulfur atom, since the LP–N–S angles are significantly smaller than the LP–N–C angles (118.5° vs. 123.2° (N1), 99.9° vs. 130.3° (N2)). The effect of lone-pair tilt and the out-of-plane distortion are much more pronounced for N2 (out of the paper plane, towards the spectator in figure 3–13c). The valence shell in the non-bonding region shows only one in-plane maximum.

The VSCCs in the non-bonding regions of the nitrogen atoms and the sulfur centre indicate for both atom types predominately sp^2 hybridisation. Both nitrogen atoms and the sulfur atom exhibit a single stereochemically active lone-pair in the SN_2 plane. The second lone-pair at sulfur must be of radially symmetrically s-character, as it causes no additional minimum in the Laplacian.

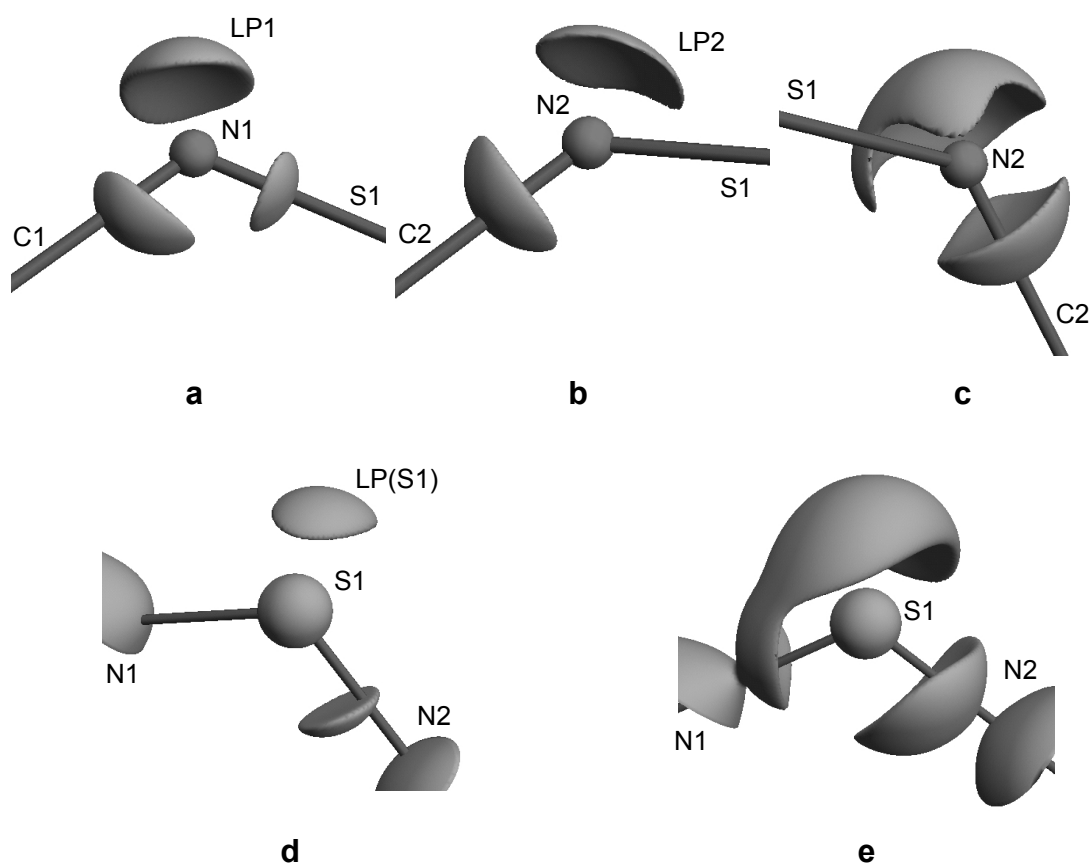


Figure 3-12: Isosurface representation in \mathbf{I} at constant values of the negative Laplacian $-\nabla^2\rho(\mathbf{r})$ (45 (a, b), 33 (c), 15 (d), $5 \text{ e}\text{\AA}^{-5}$ (e)) indicating bonding and non-bonding (LP) VSCCs around N1 (a), N2 (b, c) and S1 (d, e), respectively.

In a qualitative model derived from simplistic orbital considerations this would result in a three-centres-two-electron bond from both singly occupied p-orbitals at the nitrogen atoms and the vacant p-orbital at the sulfur atom. This electron poor delocalised π -system along the SN_2 backbone is favoured by the investigations of the Laplacian.

The VSCCs in the bonding and non-bonding regions explain consistently the asymmetry of the sulfur diimide molecule **I** in the solid state. The most remarkable feature is the bending of the lone-pair LP2 at N2 towards the sulfur atom. Different to the lone-pair at N1, located almost exactly at the bisection of the S–N–C bond angle (figure 3–12a), LP2 at N2 reaches out to the electropositive sulfur atom (figure 3–13b,c). While the LP1–N1–S1 angle is 118.5° , the related LP2–N2–S1 angle is only 99.9° (figure 3–13). This electrostatic LP2–S1 interaction rises the charge density $\rho(r_{\text{BCP}})$ at the S1–N2 bond to $2.24 \text{ e}\text{\AA}^{-3}$ in comparison to $1.93 \text{ e}\text{\AA}^{-3}$ at S1–N1, where this reinforcement is not present.

The Laplacians rehabilitate the reliability of the static deformation density studies, as this effect was already detected there (figure 3–10). Another consequence is the location of the S1–N2 BCP much closer at the N2 nitrogen atom than the S1–N1 BCP at the N1 nitrogen atom. The polarity Q of the S1–N1 bond remains the highest among the studied S–N bonds (0.44), while the S1–N2 bond polarity is reduced by the electrostatic LP2–S1 interaction (0.51). In addition to the steric strain of the Z-oriented ^tBu group, this electrostatic LP2–S1 interaction causes the S1–N2–C2 angle to be widened to $128.1(1)^\circ$ compared to $118.5(1)^\circ$ for S1–N1–C1. As a consequence the S1–N2 bonding VSCC is dislocated from the straight S1–N2 line towards the inside of the N1–S1–N2 angle (figure 3–11a,c and figure 3–12d). This mutual bending causes S1–N2 in **I** to be the most strained sulfur-nitrogen bond with the most significant difference between bond length and bond path among the thirteen studied in this thesis (table 3–16). The LP2–S1 interaction causes the sulfur lone-pair VSCC to be dislocated from the parallel orientation relative to the bisection of the N1–S1–N2 angle and tilted towards the S1–N1 bonding VSCC (figure 3–12e). This orientation of the sulfur lone-pair suits the higher electronegativity of N1 and the polar character of the S1–N1 bond.

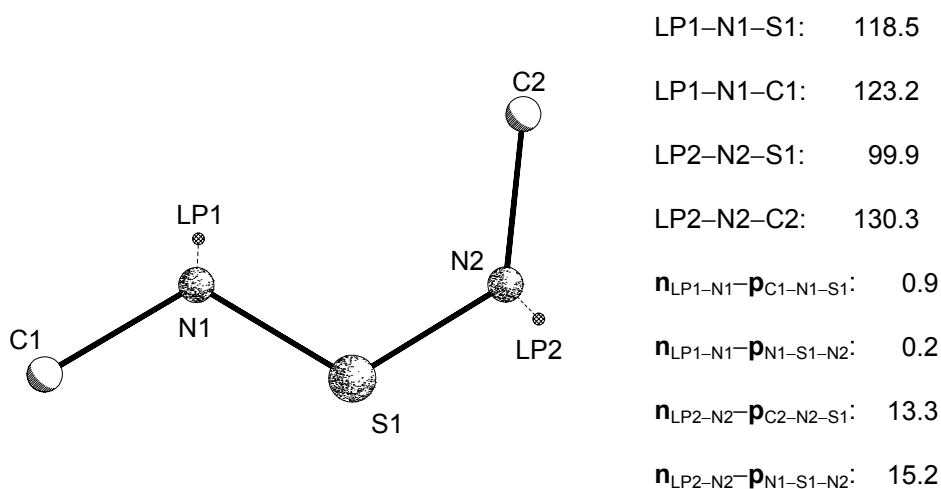


Figure 3-13: Orientation of the non-bonding VSCCs (lone-pairs) in I. $n-p$ denote angles [°] between the bonding vectors n_{A-B} and vectors parallel to the A-B-C planes, respectively.

The electrostatic LP2-S1 interaction, already present in the contour plot of the negative Laplacian (see figure 3-11a), can equally be detected in the spatial distribution of the reactive surface around the sulfur atom, where the Laplacian vanishes ($\nabla^2\rho(\mathbf{r}) = 0$). The latter visualises the most probable directions of a nucleophilic attack to the electrophilic centre.

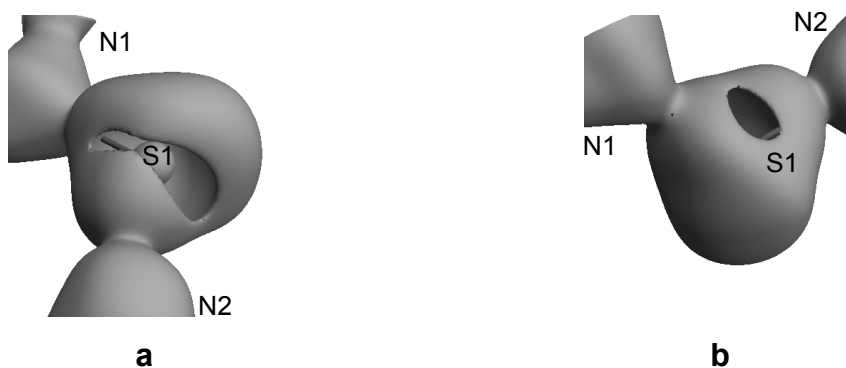


Figure 3-14: Isosurface representation of the reactive surface ($\nabla^2\rho(\mathbf{r}) = 0$) in I.

The reactive surface at the sulfur atom reveals holes towards N2 (figure 3-14a) and orthogonal to the SN_2 plane (figure 3-14b). As the first is occupied by the LP2 lone-pair, a nucleophile has to approach the sulfur atom *via* the second hole. This is in accordance with the products isolated e. g. from the reactions of sulfur diimides with alkali organometallics. On metal-carbon bond cleavage the carbanion binds to the sulfur through the hole, while the metal is chelated by the lone-pairs of the two nitrogen atoms.^[37]

3.8.4.2 Laplacian Distribution in **II**

Since the sulfurtriamide molecule **II** was constrained during the refinements to be C_3 symmetrical by a threefold axis through S1 perpendicular to the SN_3 plane, this symmetry is valid in the contour plots (figure 3–15), the isosurface representations of the negative Laplacian (figure 3–16), and in the reactive surfaces (figure 3–18).

The symmetry independent S1–N1 bond is very similar to the S1–N2 bond in the sulfurdiimide **I**. The bonding VSCCs are contracted perpendicular to the connection line and the non-vanishing negative Laplacian in the bonding regions (figure 3–15) indicates shared electron interaction. A non-bonding VSCC at N1 (LP1A) is located almost in plane with respect to the SN_3 core, since the angle between $\mathbf{n}_{LP1A-N1}$ and the S–N–C plane is only 7.4° . As the central sulfur atom in **II** is of oxidation state +VI, there is no stereochemically active lone-pair present.

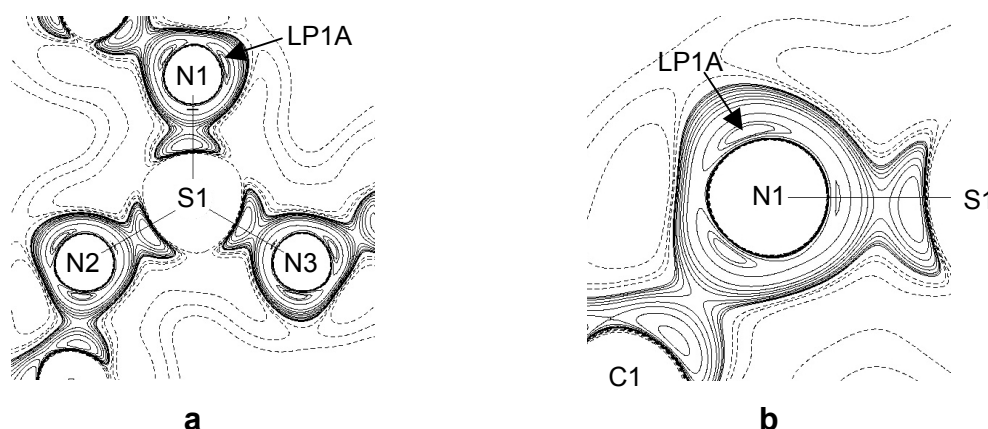


Figure 3-15: Contour plots of the Laplacian $\nabla^2\rho(\mathbf{r})$ in **II** displaying charge concentrations in the SN_3 (**a**) and LP1A–N1–S1 (**b**) plane, respectively. Negative values (concentrations) are marked by solid lines, positive values by dashed lines. Maxima of the non-bonding VSCCs (lone-pairs) are labelled LP.

The out-of-plane low-level contractions in $-\nabla^2\rho(\mathbf{r})$ are located between the sulfur and the nitrogen atom, while the high-level concentrations are located close to the nitrogen atom N1 (figure 3–16). Like in **I**, the in-plane lone-pair is tilt to the electropositive sulfur atom ($LP1A-N1-S1 = 109.4^\circ$, $LP1A-N1-C1 = 124.0^\circ$, figure 3–17). The charge density $\rho(r_{BCP})$ of $2.27 \text{ e}\text{\AA}^{-3}$ at S1–N1 is increased to a value almost identical to that at the S1–N2 bond in **I** ($2.24 \text{ e}\text{\AA}^{-3}$). In addition, the electrostatic LP1A–S1 interaction widens the average S–N–C bond angle to $125.98(2)^\circ$.

However, the in-plane LP1A is not the only non-bonding VSCC which is characterised by a (3,-3) CP in the negative Laplacian of Π . LP1B has to be classified as lone-pair density as well (figure 3–16a,b). While LP1A would be an excellent indication for a sp^2 hybridised nitrogen atom, LP1B is located almost orthogonal to the line LP1A–N1 (LP1A–N1–LP1B = 83.9°) above the SN_3 plane (figure 3–17). At first sight this geometry clearly is reminiscent to a sp^2 hybridised nitrogen atom with a populated orthogonal p-orbital. At second sight, however, there should be a maximum in the non-bonding VSCC underneath the SN_3 plane as well. Although the orientation of the second lone-pair does not match a classical sp^3 hybridised nitrogen atom, two stereochemically active sp^3 lone-pairs would explain the non-bonding VSCCs best.

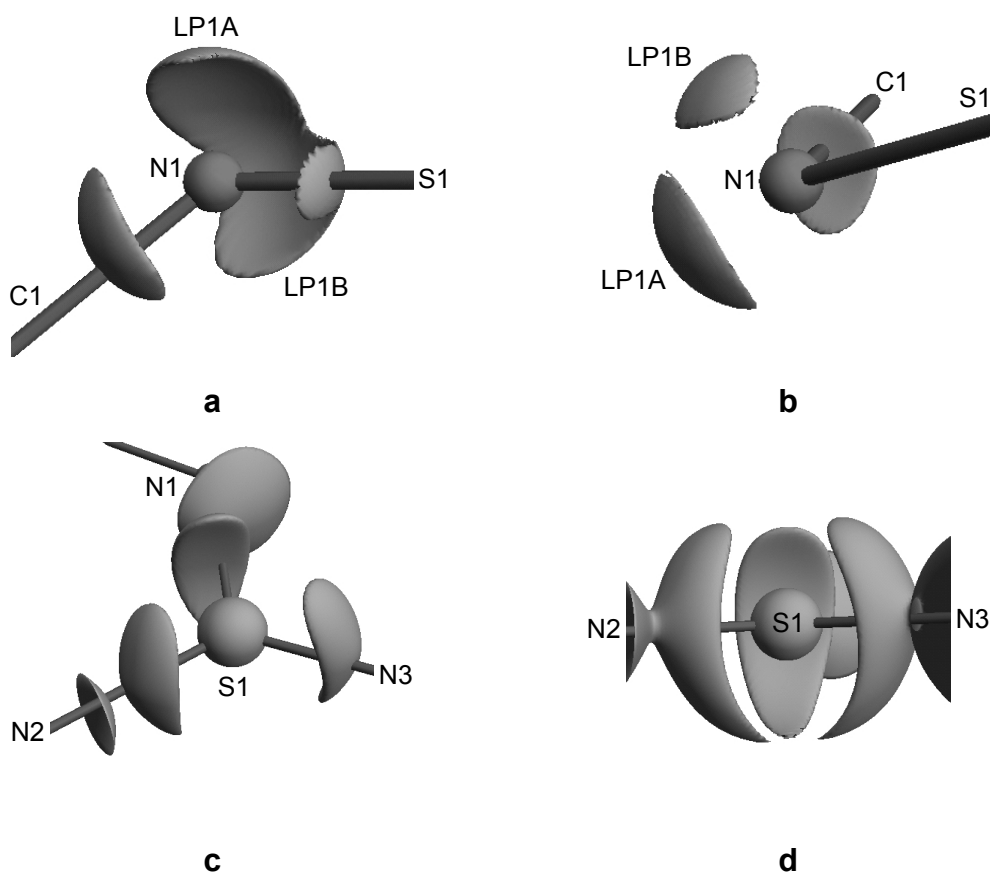


Figure 3-16: Isosurface representation in Π at constant values of the negative Laplacian $-\nabla^2\rho(r)$ (44 (a), 47 (b), 8 (c), $5 \text{ e}\text{\AA}^{-5}$ (d)) indicating bonding and non-bonding (LP) VSCCs around N1 (a, b) and S1 (c, d), respectively.

In addition to the mentioned out-of-plane disorder (see scheme 3–2) the considerable ellipticity (0.22) of the S1–N1 bond is presumably caused by LP1B reaching out to S1. In this context it is pointed out, that the second apical lone-pair at the nitrogen atom is not an artefact of the disorder in Π , since above and

below the sulfur atom only weak charge concentrations are located instead (see figure 3–16d).

The S1–N1 bond intersects the LP1A–N1–LP1B plane at an angle of 110.0° , while the N1–C1 bond at an angle of 126.0° . This indicates the tilt of both non-bonding VSCCs towards the sulfur atom. Since most of the electron density is located at the electronegative atoms, a nitrogen centred 4-centres-6-electrons bond with considerable partial charges might explain the bonding in **II** best. π -delocalisation with valence expansion due to d-orbital population at sulfur experimentally seems most unlikely, as the sulfur atom shows severe electron depletion.

The asymmetry of the pronounced non-bonding VSCCs in the Laplacian at the nitrogen atoms is reproduced in the marginal bonding VSCCs at sulfur, depicted in figure 3–16c and d. The negative Laplacians are constrained to be C_3 symmetrical but do not reveal C_{3h} symmetry upon refinement. They show marginal concentration at one side and depletion at the opposite side of the SN_3 plane. The in-plane lone-pair LP1A is slightly bent towards the side of concentration, while LP1B resides at the side of depletion at the sulfur atom. The slight pyramidalisation of the molecule is not only indicated by the ADPs discussed previously in chapter 3.5, but also displayed by the electron density distribution.

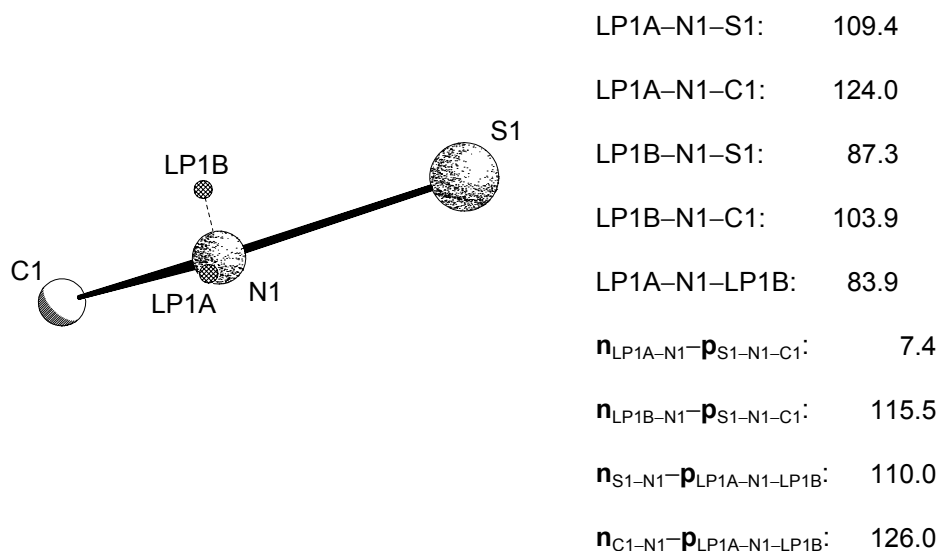


Figure 3-17: Orientation of the non-bonding VSCCs (lone-pairs) in **II**. The $n-p$ denote angles [$^\circ$] between the bonding vectors n_{A-B} and vectors parallel to the A–B–C planes, respectively.

The reactive surface at the sulfur atom in **II** shows areas of strong depletion of charge located in the SN_3 plane at the bisections of the N–S–N angles (figure 3–15a and figure 3–18a).

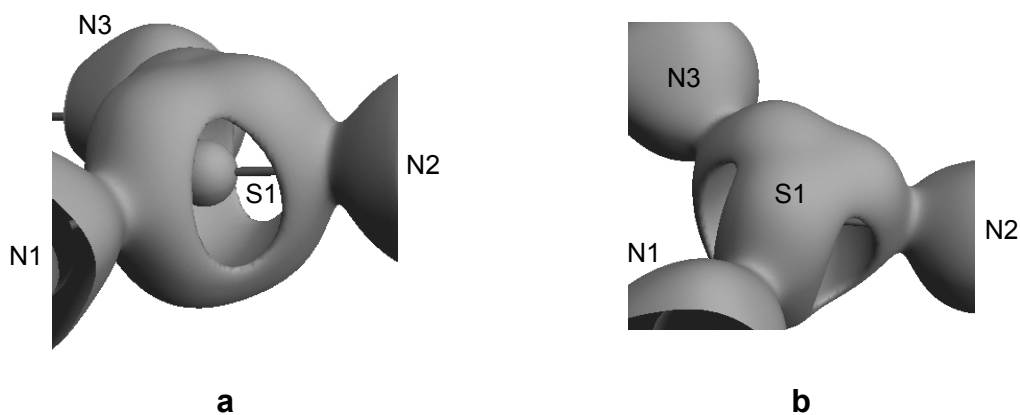


Figure 3-18: Isosurface representation of the reactive surface ($\nabla^2\rho(\mathbf{r}) = 0$) in **II**.

Interestingly, there is no hole on top of the sulfur atom. A nucleophilic attack orthogonal to the SN_3 plane is precluded by the electron density distribution. This, in fact explains the reactivity of the sulfur triimide: $S(N^tBu)_3$ reacts smoothly with $MeLi$ ^[37c] or $PhCCLi$ but not with nBuLi or tBuLi .^[44] The carbanionic nucleophile has to approach the sulfur triimide in an angle of about 45° and that is only feasible by small carbanions. Large anions can not reach the holes, as they only can approach the molecule in a wider angle. The steric argument is not valid if a direct orthogonal attack is anticipated, as there is enough room in the planar molecule to reach the sulfur atom at a direct orthogonal line.

3.8.4.3 Laplacian Distribution in **III**

The spatial distributions of $-\nabla^2\rho(\mathbf{r})$ in $H(N^tBu)_2SMe$ reveal two differing S–N bonds. Like the others, both show the typical features for shared interactions, as clear contractions of the density perpendicular to the bonds and non-vanishing contributions in the internuclear regions (figure 3–19a-d) are observed.

The bonding maxima of the VSCCs are separated and are located on the direct connection line between the bonded atoms. The non-bonding VSCCs are well resolved at the nitrogen atoms as well as at S1. The stereochemically active lone-pair concentrations at N1 and S1 are located as (3,-3) CPs in $-\nabla^2\rho(\mathbf{r})$ at the expected apical position of a trivalent sp^3 hybridised nitrogen or sulfur atom (see figure 3–19a,d and figure 3–20a,d). Different to the sulfur lone-pair in **I**, the LP(S) in **III** is clearly resolved from the S–N bonding VSCC. The geometry at

N1, including the lone-pair orientation, shows a slightly distorted tetrahedral environment ($\text{LP1-N1-H1} = 116.5^\circ$) with the typical tilt of LP1 towards the electropositive S1 ($\text{LP1-N1-S1} = 90.8^\circ$, $\text{LP1-N1-C1} = 101.4^\circ$). The geometry at both nitrogen atoms is depicted in figure 3–21. At the formally double bonded nitrogen atom N2 in **III** two separated (3,-3) CPs in the negative Laplacian have been found, indicating the presence of two lone-pairs at N2 (figure 3–19e and figure 3–20b,c).

Different to the orientation of the lone-pairs in the sulfurtriamide **II**, the non-bonding VSCCs in **III** are positioned above and below the S1–N2–C2 plane. This geometry indicates a classical sp^3 hybridised N2 atom.

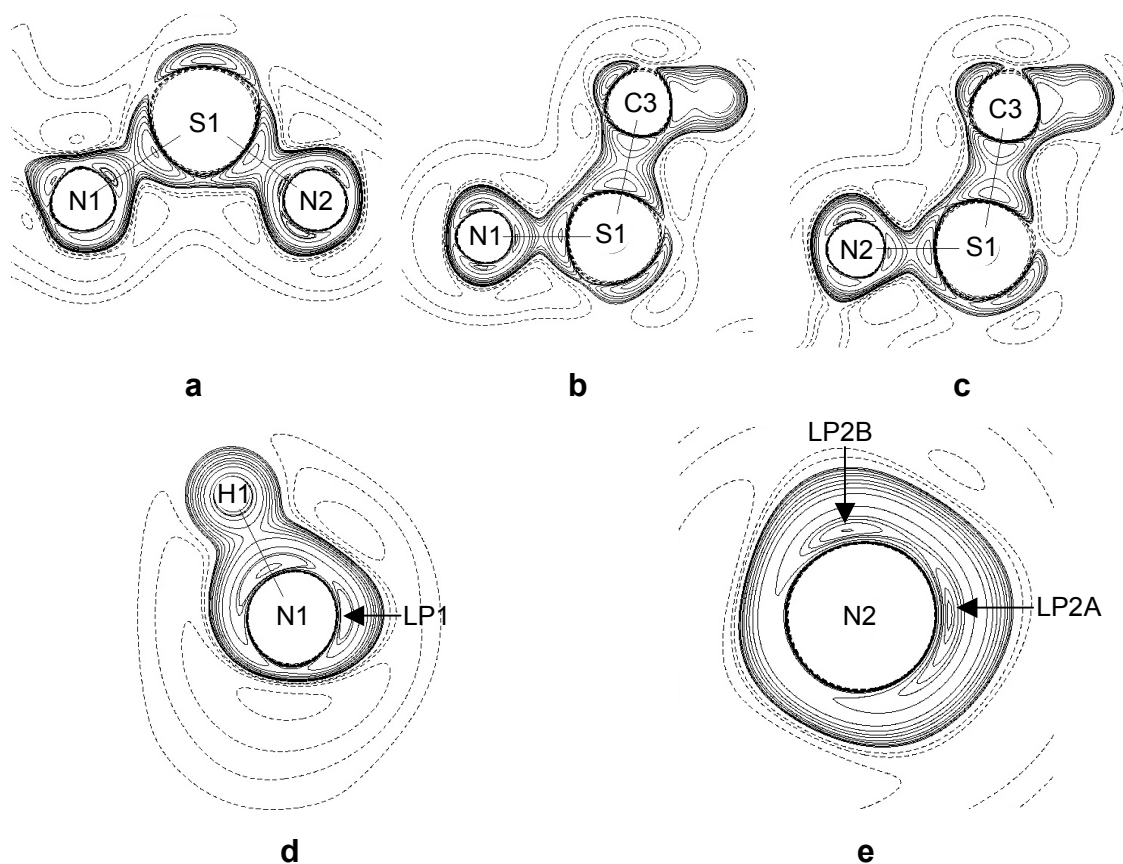


Figure 3-19: Contour plots of the Laplacian $\nabla^2\rho(\mathbf{r})$ in **III** displaying charge concentrations in the N1–S1–N2 (a), N1–S1–C3 (b), N2–S1–C3 (c), H1–N1–LP1 (d) and LP2A–N2–LP2B plane (e). Negative values (concentrations) are marked by solid lines, positive values by dashed lines, respectively. Maxima of the non-bonding VSCCs (lone-pairs) are labelled LP.

The vectors along the connection line between the lone-pairs and N2 and the S–N–C plane form an angle of 141.3° and 117.9° , respectively. The LP2A-N2-LP2B angle is 100.9° and displays with the LP-N-S (98.0° for LP2A,

96.8° for LP2B) and LP–N–C angles (129.6° for LP2A, 111.2° for LP2B) a distorted tetrahedral environment for N2.

Again, both lone-pairs are remarkably inclined towards the electropositive sulfur atom. The S1–N2 bond intersects the LP2A–N2–LP2B plane at an angle of 101.7°, the N2–C2 bond at an angle of 143.5°. The tilt of LP2A is more pronounced than that of LP2B, because the latter is the stronger donor in the hydrogen bond to H1A and therefore less attractive to the sulfur atom (LP2A⋯H1 = 1.865 Å, LP2B⋯H1 = 1.742 Å). The contraction of the LP1A–N2–LP2B angle from the ideal 109.5° to 100.9° can be explained by the interaction of both lone-pairs with the hydrogen atom akin a bifurcated hydrogen bond.

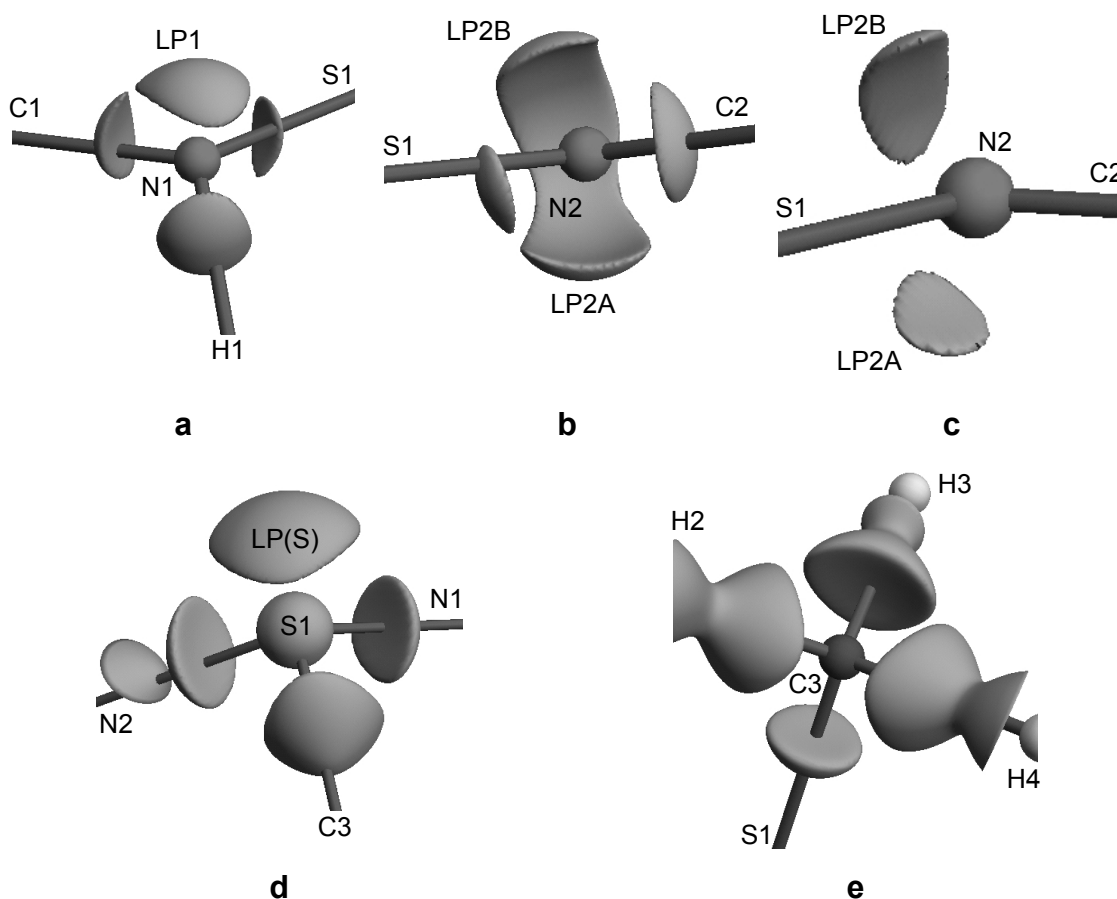


Figure 3-20: Isosurface representation in **III** at constant values of the negative Laplacian $-\nabla^2\rho(\mathbf{r})$ (48 (a), 44 (b), 55 (c), 10 (d), 15 $\text{e}\text{\AA}^{-5}$ (e)) indicating bonding and non-bonding (LP) VSCCs around N1 (a), N2 (b, c), S1 (d) and C3 (e), respectively.

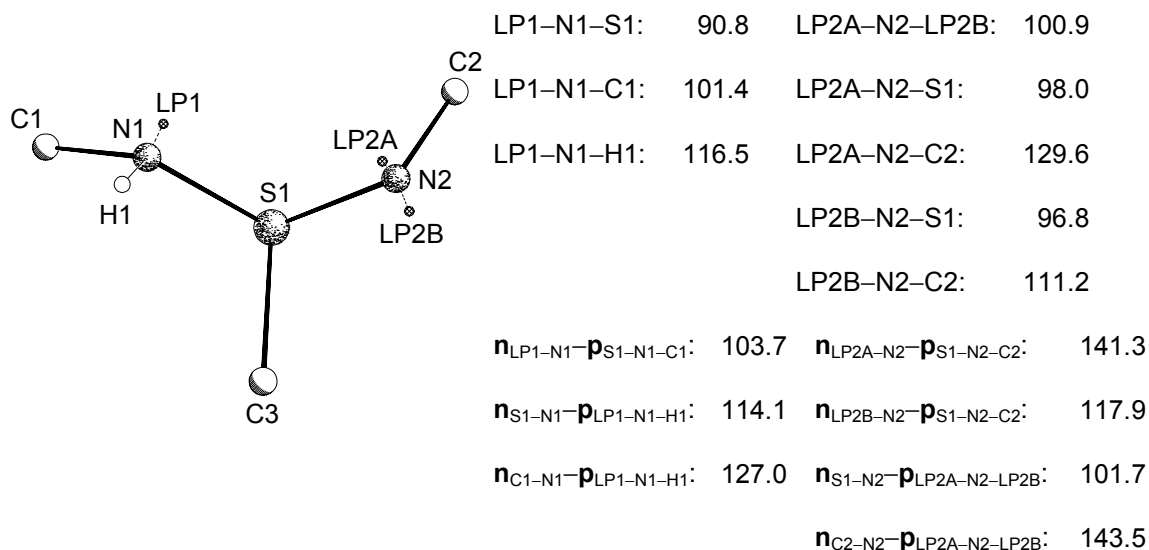


Figure 3-21: Orientation of the non-bonding VSCCs (lone-pairs) in **III**. The $n-p$ denote angles [$^{\circ}$] between the bonding vectors n_{A-B} and vectors parallel to the A-B-C planes, respectively.

The reactive surface of the sulfur atom in **III**, depicted in figure 3-22, reveals holes at the four faces of the density tetrahedron formed by the lone-pair and the bonds of S1 to N1, N2, and C3, respectively. The smallest hole is present in the LP(S)/N1/N2 face. Therefore the electronically preferred direction of a nucleophilic attack at S1 is either at the LP(S)/N1,2/C3 faces or from below at the N1/N2/C3 face, causing inversion at the sulfur atom.

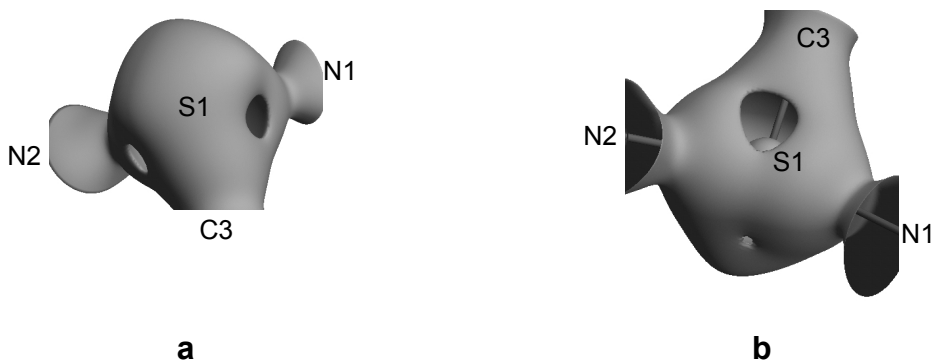


Figure 3-22: Isosurface representation of the reactive surface ($\nabla^2\rho(r) = 0$) in **III**.

3.8.4.4 Laplacian Distribution in **IV**

Since a twofold axis through C7 and the centre of the S₂C7 unit was assumed during the refinements, this symmetry restriction is reflected in the $\nabla^2\rho(r)$ distributions of CH₂{S(N^tBu)₂(NH^tBu)}₂ (**IV**).

All bonds reveal perpendicular contraction of the internuclear densities with the characteristics of shared interactions. All VSCCs are well separated. The density polarisations at the formally double bonded nitrogen atoms N2 and N3 in the direction of S1 are less distinct than for the other atoms (figure 3–23a). That was already found for S1–N2 in the sulfur diimide (I). The maxima of the S1–C7 and N–H bonds are located on the direct connection line, the bonding VSCCs of the S–N bonds are only slightly shifted away (figure 3–23b-d).

At N1 one (3,-3) CP in $-\nabla^2\rho(\mathbf{r})$ was found, while at N2 and N3 two non-bonding charge concentrations could be located. The lone-pair at N1 forms an angle of 119.2° with N1 and H1 and is distinctly oriented towards S1 (LP1–N1–S1 = 87.0° , LP1–N1–C1 = 105.3°) to form a distorted tetrahedral environment at N1.

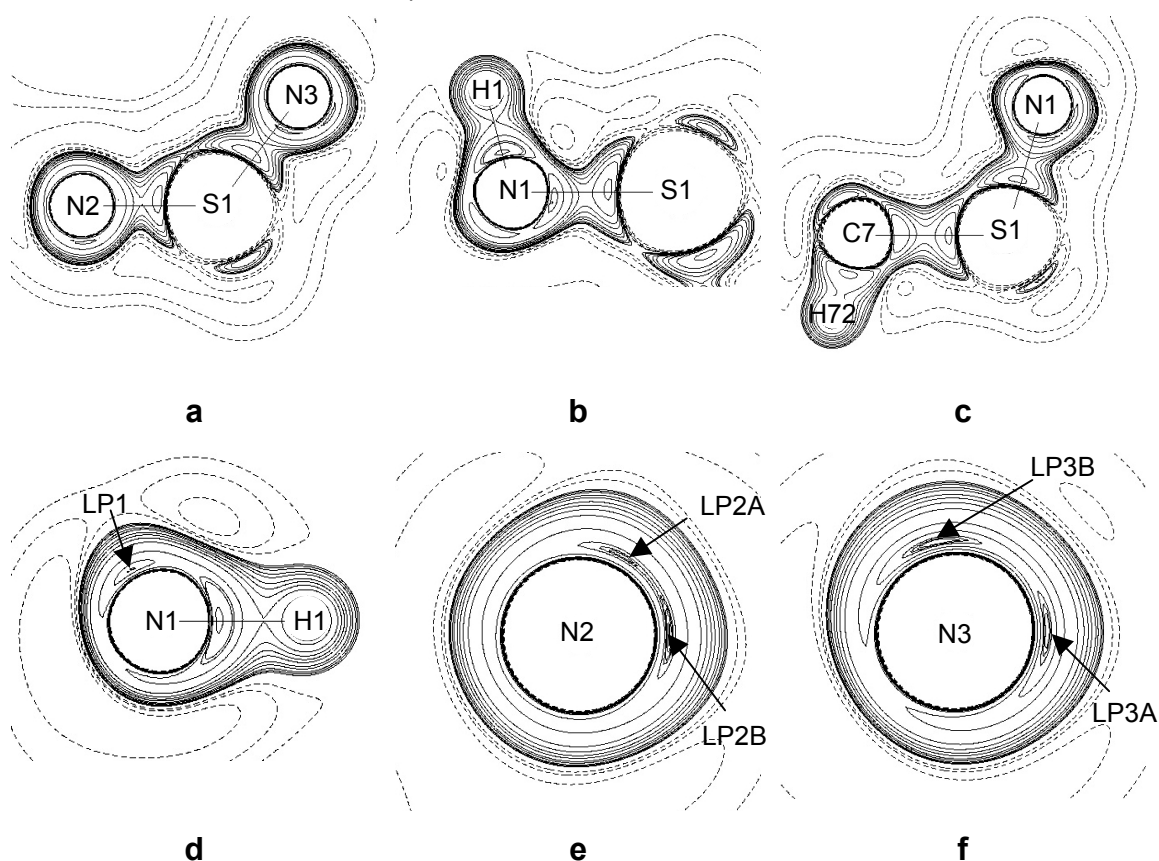


Figure 3-23: Contour plots of the Laplacian $\nabla^2\rho(\mathbf{r})$ in **IV** displaying charge concentrations in the N2–S1–N3 (a), H1–N1–S1 (b), N1–S1–C7 (c), LP1–N1–H1 (d), LP2A–N2–LP2B (e) and LP3A–N3–LP3B plane (f), respectively. Negative values (concentrations) are marked by solid lines, positive values by dashed lines, respectively. Maxima of the non-bonding VSCCs (lone-pairs) are labelled LP.

The lone-pair VSCCs at N2 and N3 are all well resolved (see figure 3–23e,f and figure 3–24b,c), but the LP2A–N2–LP2B angle of 62.8° is very small. Like in **III**, the small angle can be explained by the participation of N2 at the intramolecular

N4–H4...N2 hydrogen bond. The non-bonding VSCCs interact like a bifurcated hydrogen bond with the opposite hydrogen atom and are therefore contracted considerably.

At the pendent nitrogen atom N3 the LP3A–N3–LP3B angle of 102.2° is much closer to the ideal tetrahedral angle. Comparable to **III**, the lone-pair densities at N2 and N3 are oriented towards the bonded sulfur atom (LP2A–N2–S1/C1 = 98.4/123.8°, LP2B–N2–S1/C1 = 97.0/133.7°, LP3A–N3–S1/C3 = 98.2/114.2°, LP3B–N3–S1/C3 = 102.8/109.9°).

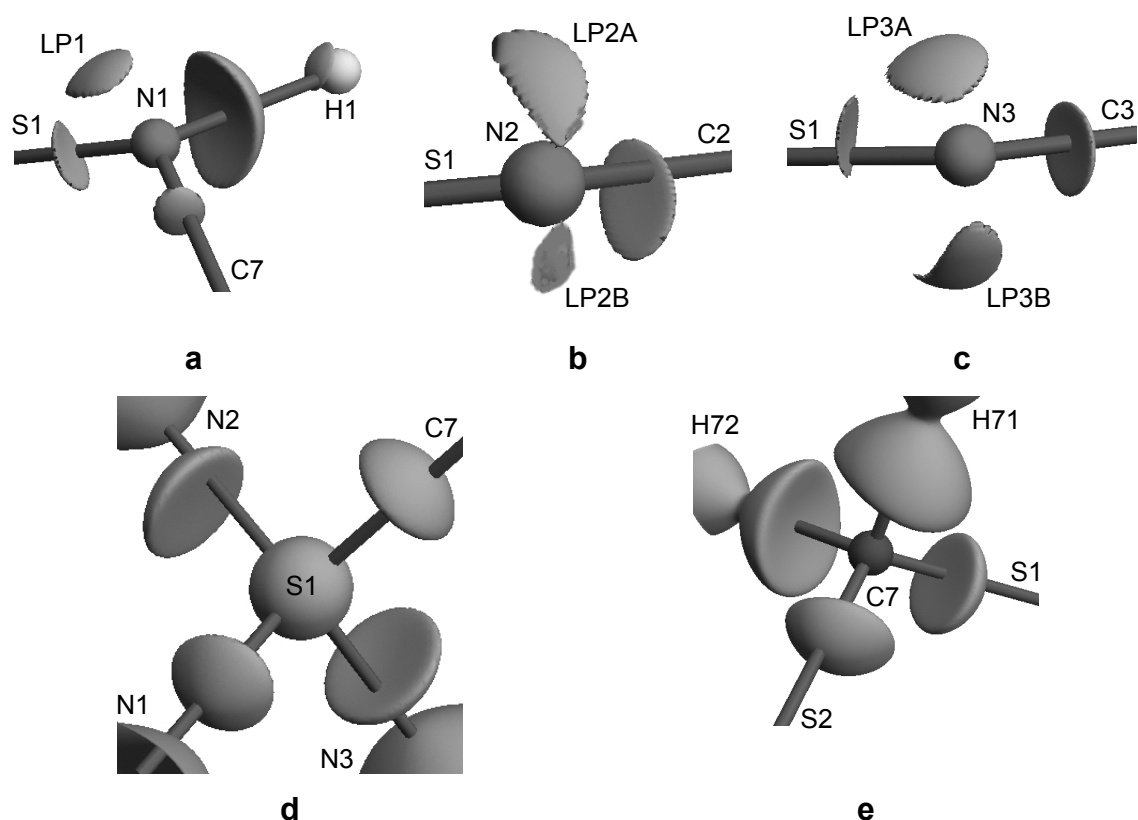


Figure 3-24: Isosurface representation in **IV** at constant values of the negative Laplacian $-\nabla^2\rho(r)$ (47 (**a**, **c**), 48 (**b**), 12 (**d**), 16 eÅ⁻⁵ (**e**)) indicating bonding and non-bonding (LP) VSCCs around N1 (**a**), N2 (**b**), N3 (**c**), S1 (**d**) and C7 (**e**), respectively.

The analyses of the Laplacian distributions around the nitrogen atoms indicate that they are sp³ hybridised. N1 reveals the expected one and both other, formally double bonded nitrogen atoms, show two separated (3,-3) CPs in $-\nabla^2\rho(r)$. The lone-pair VSCC at N1 indicates concentration at the apical position of a trigonal pyramidal coordinated sp³-nitrogen atom (figure 3–24a), but it is oriented towards the bonding region, proofed by the small angle of 87.0° to the S1–N1 bond (figure 3–25). This feature explains the considerable ellipticity of the S1–N1 bond.

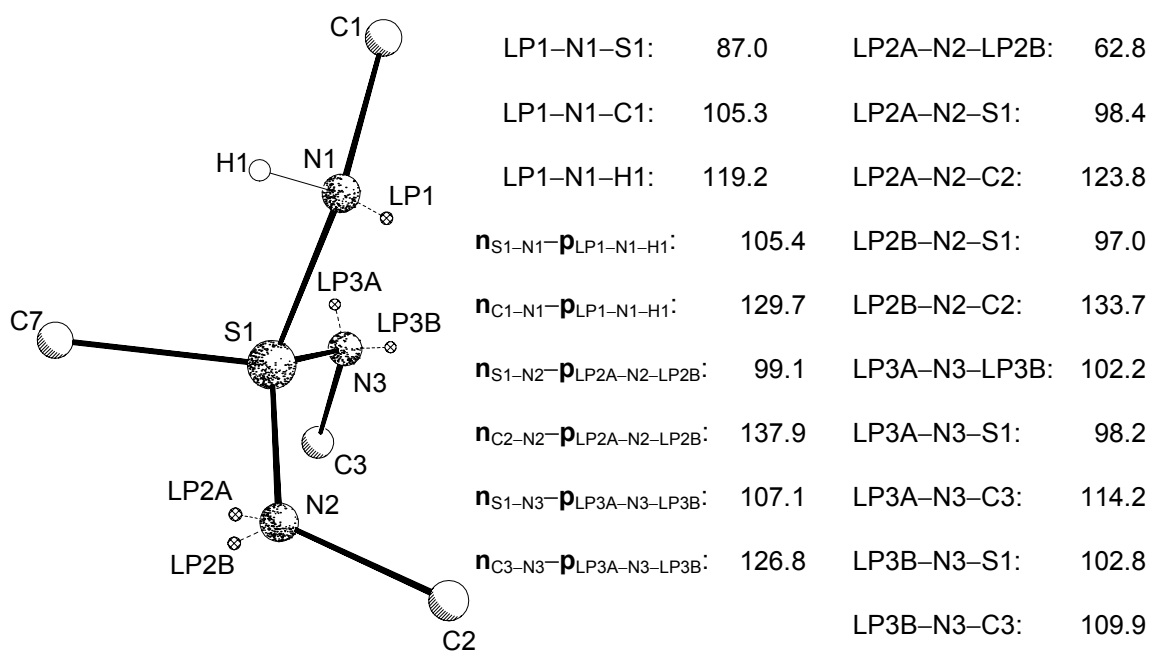


Figure 3-25: Orientation of the non-bonding VSCCs (lone-pairs) in **IV**. The $\mathbf{n} \cdot \mathbf{p}$ denote angles [°] between the bonding vectors \mathbf{n}_{A-B} and vectors parallel to the A–B–C planes, respectively.

The VSCCs at N3 in the lone-pair regions affirm sp^3 -character, as the maxima in $-\nabla^2\rho(r)$ are located above and below the S–N–C plane (figure 3–24b,c) with an LP3A–N3–LP3B angle of 102.2°. With the S1–N3–C3 bond angle of 126.6(1)°, this causes a rather distorted tetrahedral environment at N3. However, the angle between N3 and the two related BCPs is only 122.0°. This more acute angle confirms the steric strain between the *tert.*-butyl group and the sulfur atom. Two maxima in $-\nabla^2\rho(r)$ are resolved in the non-bonding region at N2. The situation is similar to N3 (S1–N2–C2 = 123.4(1)° vs. BCP–N2–BCP = 118.1°), although more perturbed by hydrogen bonding. The LP2A–N2–LP2B angle is only 62.8° because both lone-pairs at N2 interact like a bifurcated hydrogen bond (LP2A⋯H4 = 1.75 Å and LP2B⋯H4 = 1.91 Å) to the opposite H4 contracting the angle considerably.

It is obvious that all non-bonding VSCCs are bent towards the associated S–N bond, shown by the angle differences between the S–N and C–N bonds and the LP–N–LP planes, indicating the orientation of the lone-pairs away from the C–N towards the S–N bonding regions (137.9° vs. 99.1° at N2 and 126.8° vs. 107.1° at N3). This causes additional density shifted towards the bond and leads to relatively high $\rho(r_{BCP})$ values, prominent negative Laplacians at the BCPs, and substantial ellipticities.

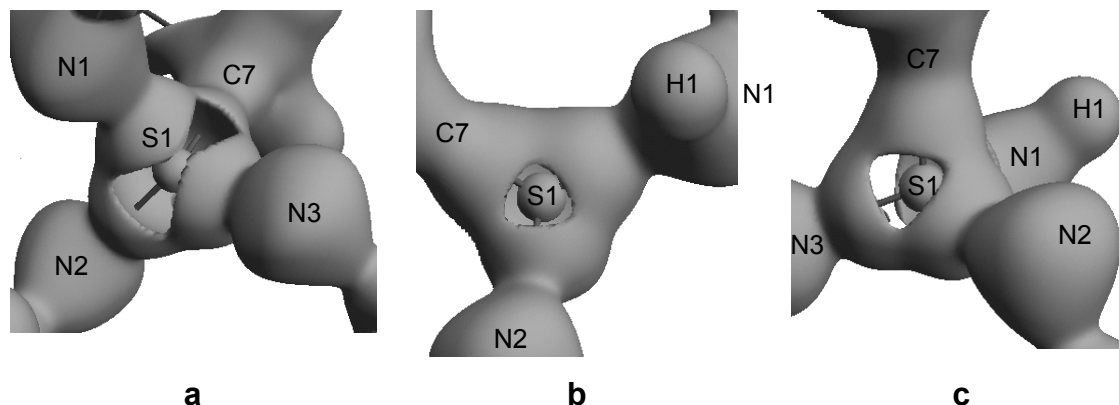


Figure 3-26: Isosurface representation of the reactive surface ($\nabla^2\rho(\mathbf{r}) = 0$) in **IV**.

The spatial distribution of the reactive surface of the sulfur atoms in **IV** depicted in figure 3–26 shows, apart from general charge depletion at the sulfur atom, holes at the faces of the tetrahedral coordination polyhedron formed by N1, N2, N3, and C7. While the holes at the C7/N1/N2- and C7/N2/N3-faces are similarly small (figure 3–26a,b), the holes at the N1/N2/N3- and C7/N1/N3-faces are equally more extended (figure 3–26c).

3.8.4.5 Comparison of the Laplacian Distributions

Although chemically quite different, the $(\text{C}-)\text{S}^{\text{IV,VI}}-\text{N}_x$ units in **III** and **IV** reveal similarities concerning their Laplacian distributions. The S–C bonding VSCCs of the sulfur and carbon atoms are well defined and their maxima are positioned almost exactly on the direct connection lines indicating a strainless bonding. The perpendicular contractions of the bonding densities, together with the non-vanishing Laplacians in the internuclear regions, show the expected features for shared S–C interactions.

The S–N bonding modes cover a wide range from S–N(H) single bonds to potential short S=N double bonds. The S–N(H) single bonds show comparable properties like the mentioned characteristics for shared unstrained interaction and similar lone-pair orientations (LP1–N1–S1: 90.8° (**III**) vs. 87.0° (**IV**), LP1–N1–C1: 101.4° (**III**) vs. 105.3° (**IV**), LP1–N1–H1: 116.5° (**III**) vs. 119.2° (**IV**)). They differ only slightly, since the N-bonded hydrogen atoms are either inter- (**III**) or intramolecular (**IV**) hydrogen bond donors.

The formal S=N double bonds supply a far-less uniform image. Actually, the Laplacian distributions in all compounds show well defined concentrations towards the bonded atoms with an exception at N2 in (**I**). All formal S=N bonds

show charge concentrations perpendicular to the bond, supporting the concept of a shared interaction between the sulfur and the nitrogen atoms.

By far the most characteristic feature concerning the Laplacian distributions are the lone-pair related non-bonding VSCCs around the sulfur and nitrogen atoms. For all compounds those at the nitrogen atoms were identified as (3,-3) CPs in the negative Laplacian. In the sulfur diimide (**I**) sp^2 hybridisation can be doubtless predicted from the detection of a single in-plane lone-pair at each nitrogen and the sulfur atom. Therefore a second sulfur centred lone-pair has to reveal s-character. Those findings predict a three-centres-two-electrons bonding model for **I**. All lone-pairs show severe orientation towards the electropositive sulfur atom. In **I** the inclination is stronger at N2 (LP2-N2-S1: 99.9° and LP2-N2-C2: 130.3° vs. LP1-N1-S1: 118.5° and LP1-N1-C1: 123.2°), which causes an orientation of the sulfur lone-pair density towards the S1-N1 bonding region.

Similarly to **I**, the non-bonding VSCCs at the nitrogen atoms in **III** and **IV** are inclined towards the central sulfur atom. In contrast to **I**, two well resolved lone-pairs have been identified at each formally double bonded nitrogen atom. Their orientation above and below the S-N-C plane makes them an indicator for sp^3 hybridisation. Therefore in the formal double bonds **III** and **IV** should be formulated as S^+-N^- . The bonds are strongly reinforced by extreme inclination of the nitrogen centred lone-pairs. These reorientations towards the positively charged sulfur atom are elucidated by large differences between the bisecting angles of the LP-N-LP plane with the S-N or N-C bonding vectors, respectively (LP2A-N2-LP2B with n_{S-N}/n_{N-C} : 101.7° vs. 143.5° (**III**), LP2A-N2-LP2B with n_{S-N}/n_{N-C} : 99.1° vs. 137.9° , LP3A-N3-LP3B with n_{S-N}/n_{N-C} : 107.1° vs. 126.8° (**IV**)).

Compared to these bonds, the S-N bonding mode in the sulfur triimide (**II**) is not to explain straightforward. The Laplacian distribution reveals features which support both, the S=N and the S^+-N^- bonding mode as well. Like in **III** and **IV**, two (3,-3) CPs in the negative Laplacian were identified at the nitrogen atoms. On the first view this leads to sp^3 hybridisation. But one lone-pair is like in **I** oriented almost coplanar to the S-N-C plane (7.4° below), while the other is oriented in apical position above the nitrogen atom (LP1A-N1-LP1B = 83.9°). Like in all other compounds, the lone-pairs are oriented towards the S-N bonding region (LP1A-N1-LP1B with $n_{S-N} = 110.0^\circ$ vs. LP1A-N1-LP1B with $n_{N-C} = 126.0^\circ$) but here the back-polarisation is not as severe as in the others.

This finding is guided by out-of-plane (SN_3) expansion of the bonding VSCCs at the sulfur atom. This precludes to categorise the bonding in **II** one way or the other. It seems to be halfway between the S^+-N^- mode with sp^3 hybridisation of the nitrogen atoms, as found in **III** and **IV**, and a nitrogen centred four-centres-six-electrons system, by the use of p-orbitals comparable to the situation found in **I**.

The reactive surfaces ($\nabla^2\rho(\mathbf{r}) = 0$) revealed for all compounds possible reaction pathways for nucleophilic attacks at the electropositive sulfur atoms. While in **I** orthogonal to the SN_2 plane a probable site for a nucleophilic attack was found, in **II** exclusively the S–N–C bisections are predestined. This makes the electrophilic sulfur in **I** easier accessible for large nucleophilic reagents. Concerning the reactive surface, the situation at **II** is closer to those in **III** and **IV**, where the holes in the reactive surfaces are located in the centres of the faces of the density tetrahedrons formed by LP(S)/N1/N2/C3/S1 in **III** and N1/N2/N3/C7/S1 in **IV**, respectively. Therefore the size of nucleophiles to attack the sulfur atoms in **II**, **III** and **IV** successfully is surely limited.

3.9 Resonance Structures from the Topology

For the understanding of the bonding situation in the molecules investigated in this thesis, all density related properties, which are deducible from the modelled charge density distributions, have to be taken into account. Those characteristics, starting with the geometrical parameters bond lengths and angles, followed by similar but directly density related bond path features, the model dependent deformation densities, and finally the topological properties as the BCPs and spatial distributions of the second derivative of the molecular ED, were presented in the previous chapters independently. In this chapter all these features are used to derive easy-to-understand resonance structures for all compounds.

Most obvious is the situation in the two species with coexistence of formal S=N double and S–N(H) single bonds: $H(N^tBu)_2SMe$ (**III**) and $CH_2\{S(N^tBu)_2(NH^tBu)\}_2$ (**IV**). Both N(H) bonds are standard S–N single bonds involved in inter- (**III**) or intramolecular (**IV**) hydrogen bonding, respectively. All nitrogen atoms in the short formal S=N double bonds reveal two lone-pairs, which unambiguously prove them to be primarily sp^3 hybridised. All lone-pairs are oriented towards

the electropositive sulfur atom leading to density back-donation. This increases densities and absolute values of the negative Laplacian and non-vanishing, but very small, ellipticities at the BCPs (0.08 to 0.10). The severe polarisation of density from S to N is displayed by the low Q values (0.47, 0.49), while the relative bond strengths can be seen from high η -values (1.18 to 1.44). The formally double bonded nitrogen atoms of both compounds should be interpreted to be negatively charged. The bond strengths and shortness are caused by electrostatic reinforcement to give $S^+ - N^-$ bonds.

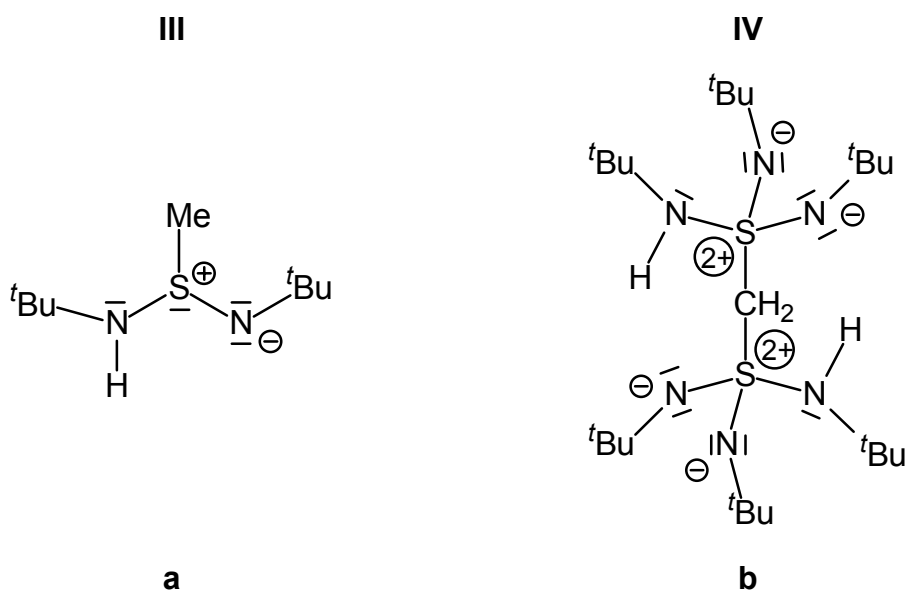
Although the classical structural parameters in **IV** as e.g. the S–N–C bond angles of $123.4(1)^\circ$ and $127.1(1)^\circ$ do not indicate sp^3 hybridisation, the related angles calculated from the BCPs are much smaller (118.1° to 124.6°) but nevertheless close to 120° . However, the lone-pairs are well separated with LP–N–LP angles of 102.2° at the undisturbed pendent N3 and 62.8° at N2. Even by weak interactions, the lone-pair geometry is modified, exemplified by the hydrogen bonds. Both lone-pairs at N2 take part in a bifurcated hydrogen bond to H4, which leads to the remarkable small LP2A–N2–LP2B angle.

In **III** the S–N–C angles are much closer to the ideal $N(sp^3)$ -value of 109.5° , namely $115.0(1)^\circ$ at N2 and $119.6(1)^\circ$ at N1. The angles calculated from the BCPs are even closer to the ideal tetrahedral angle (111.3° and 117.3°). The LP2A–N2–LP2B angle in **III** was found to be 100.9° with LP2A oriented towards the hydrogen atom in the intermolecular hydrogen bond.

Taking all those findings into account, the resonance structures displayed in scheme 3–4 describe the bonding in **III** and **IV** best: sp^3 hybridisation for all nitrogen atoms and formal negative charges with back polarisation towards the positively charged sulfur atom. Bond shortening occurs by coexistence of a covalent S–N single bond and electrostatic reinforcement due to atomic charges.

The sp^3 lone-pair densities interact with the C–C bond densities, which leads to inclination of the methyl groups towards the lone-pair densities of the nitrogen atoms at the same side. Although this observation is not substantiated by always consistent and significant changes in bond length, densities at the BCPs or their position at the bond path, these are strong hints to hyperconjugation effects. The inclinations of the affected methyl groups are significant. However, at present it seems impossible to deconvolute the distortions of the N^tBu groups

by means of steric hindrance, hydrogen bonding, and weak hyperconjugation effects.



Scheme 3-4: Best resonance structures for **III** (a) and **IV** (b).

As discussed before, the planar geometry of the SN_x backbones in **I** and **II** allows a third probable bonding mode for the description of the electrical situation in the SN_x cores: bond strengthening by m -centres- n -electrons bonds employing non-hybridised p -orbitals.

The two formal $S=N$ bonds in the sulfurdiimide (**I**) are formally equivalent, which is supported by almost identical bond lengths (1.5437(4) Å ($S1=N1$), 1.5279(4) Å ($S1=N2$)), but the ED related properties differ significantly. Beginning with the topological properties at the BCPs ($\rho(r_{BCP})$: 1.93(3) $e\text{Å}^{-3}$ vs. 2.24(3) $e\text{Å}^{-3}$, η_{BCP} : 1.05 vs. 0.84, λ_3 : 9.18 $e\text{Å}^{-5}$ vs. 14.92 $e\text{Å}^{-5}$ for $S1=N1$ vs. $S1=N2$), followed by the ratio Q , which adopts the smallest value found for all investigated $S-N$ bonds in $S1=N1$ (0.44) and the largest value in $S1=N2$ (0.51), respectively, differing bond orders (1.10 vs. 1.31 (NRT) 1.16 vs. 1.52 (AIM)), and finally the spatial distributions of the negative Laplacian, all features were very different for the two formally equivalent $S=N$ bonds. Those differences result from the molecular E/Z conformation present in the solid state, which leads to lone-pair densities at the nitrogen atoms oriented towards the same side ($N2$) or to the opposite direction ($N1$), with respect to the stereochemically active lone-pair located at the sulfur atom. This lone-pair orientation is already visualised by the distribution of the static deformation densities and further quantified by (3,-3) CPs found in the negative Laplacian. At each atom of the SN_x core one in-plane

stereochemically active lone-pair was located, indicating sp^2 hybridisation (N1: 0.9° and N2: 13.3° out-of-plane). Like all investigated nitrogen centred lone-pairs, they are strongly inclined towards the electropositive sulfur atom. This preferred orientation is more pronounced at N2 (LP2–N2–S1: 99.9° and LP2–N2–C2: 130.3° vs. LP1–N1–S1: 118.5° and LP1–N1–C1: 123.2°), which causes an interaction with the sulfur lone-pair. This leads to a coupling of the non-bonded ED at the sulfur atom into the S1–N1 bond.

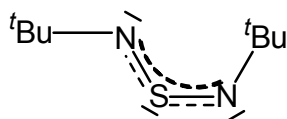
The central SN_2C_2 backbone in **I** is almost planar. Together with the sp^2 like lone-pair orientation at the nitrogen atoms and the lack of a second stereochemically active lone-pair at the sulfur atom (it has to reveal s-character), this allows the assumption of electron delocalisation over a 3-centres-2-electrons system.

The mentioned lone-pair orientation at the sulfur atom towards the S1–N1 bond leads to charge concentrations above the SN_2 plane on low-level found in the spatial distribution of the negative Laplacian at S1. In addition, those might be affected by the intermolecular S...S interaction verified by the existence of a (3,-1) BCP with non-vanishing density at the critical point between two neighbored sulfur atoms. As already Scherer *et al.* pointed out, the nature and extend of long range interactions of the S...S type is still unclear.^[27] Therefore the influence on the S=N bonding situation is furthermore not deducible, even more as the lone-pair orientations in **III** and **IV** have been proved to be extremely affected by weak long range hydrogen bonds. However, the weak S...S interaction might have some influence on the delocalised 3-centres-2-electrons system. The bond path between the S...S interaction is not bisecting the N1–S1–N2 angle, the S...S1–N1 angle is 108.1° , while the S...S1–N2 angle was found to be 97.5° , and the angle formed by the SN_2 plane with the S...S bonding vector is 115.9° . The disturbance of the delocalised 3-centres-2-electrons system due to the S...S interaction is therefore not symmetric with respect to the SN_2 unit. Therefore the S...S interaction might have some influence on the out-of-plane charge concentrations at the sulfur atom.

Taking all those findings into account, a bonding model is presented in scheme 3–5, which seems to describe the electronic situation in the sulfur diimide best:

- A σ -bonded SN_2 backbone strengthened by a 3-centres-2-electrons system, which is delocalised over the SN_2 unit formed by the non-hybridised p-orbitals;
- asymmetrical electron density back-donation due to different lone-pair

inclinations; (iii) possible disturbance of the effective delocalisation in the π -electron system due to long-range S...S interaction.



Scheme 3–5: Schematic representation of the delocalised 3-centres-2-electrons system in I.

Although two (3,-3) CPs in $-\nabla^2\rho(\mathbf{r})$ were found at the nitrogen atoms in the sulfurtriamide (II) as well, the bonding situation differs from those in III and IV. The sulfur–nitrogen interactions in II show several characteristics for multiple bonding. In addition to the short bonds (av. 1.5100 Å), a relatively high density (2.27(3) eÅ⁻³) and a unprecedented high ellipticity of 0.22 at the BCP is observed. The problematic of BCP based bond classification was discussed before, but the increased ellipticities at the BCP of the sulfur-nitrogen bonds in II might be caused in part by the mentioned out-of-plane disorder of the SN₃ core.

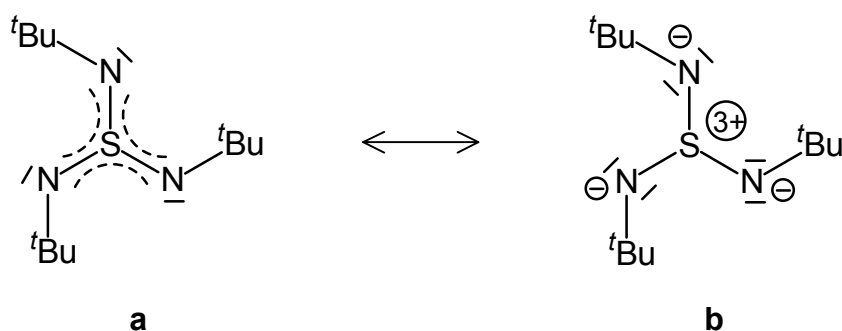
Therefore more significance is given to the localisation of two non-bonding VSCCs at the nitrogen atoms. In addition to an in-plane lone-pair another (3,-3) CP in $-\nabla^2\rho(\mathbf{r})$ was determined in an apical position. The position of the in-plane lone-pair associated VSCC supports sp² character, but the presence of two well separated non-bonding maxima, both identified as (3,-3) CPs in $-\nabla^2\rho(\mathbf{r})$, suggests a sp³ hybridisation for the nitrogen atoms (LP1A–N1–LP1B = 83.9°). The charge concentrations around the sulfur atom do not exactly show mirrorplane symmetry. The contractions parallel to the apical lone-pair peak at the nitrogen atoms are slightly pronounced. Together with the very flat trigonal pyramidal geometry one could tend to assign partial sp³ character to S1. But it has to be emphasised that this effect is marginal, especially if the possible disorder, which was discussed before, is taken into account.

Nevertheless, the S–N bonds are distinctly polarised, as reflected by the relatively low Q (0.49), low η (0.92), and high λ_3 value (15.69 eÅ⁻⁵), which balances the perpendicular contractions. As already mentioned in chapter 3.8.3, a bond order larger than unity was predicted by calculations for the S–N bonds in S(NMe)₃ by theoretical methods.^[130]

Obviously, the charge density distribution in the sulfurtriamide reveals features which allow two bonding modes to be formulated: S⁺–N⁻ comparable to III and IV, mainly supported by the existence of two non-bonding VSCCs, and a nitrogen centred 4-centres-6-electrons system akin I, deducible from the BCP

characteristics (i. e. $\varepsilon = 0.22$). S=N bonding by π -delocalisation with valence expansion due to d-orbital population at sulfur experimentally seems most unlikely, as the sulfur atom shows severe electron depletion. As seen before, the lone-pairs, which were identified by (3,-3) CPs in the negative Laplacian, are remarkably inclined towards the sulfur atom leading to high densities at the BCPs ($n_{S1-N1-p_{LP1A-N1-LP1B}}$: 110.0° vs. $n_{N1-C1-p_{LP1A-N1-LP1B}}$: 126.0°).

Especially the bonding situation in the sulfurtriiimide impressively reveals the limitation of easy-to-handle schematic representations of molecular bonding modes. None of the resonance structures presented before describes the density features satisfactory. Compared to the other compounds, which were investigated in this thesis, the charge density distribution within the SN_3 core of the sulfurtriiimide seems to adopt an intermediate state between S^+-N^- as found in **III** and **IV** and bond strengthening by a delocalised π -electron system as proposed for **I**.



Scheme 3-6: Best resonance structures for **II**.

Since the mentioned disorder may cause the out-of-plane density extension, more weight is assigned to resonance structure **b** in scheme 3-6. The S^+-N^- bonding mode leads to a positive charge of three at the sulfur atom. That induces severe density back-polarisation from the lone-pair densities at the nitrogen atoms.

To elucidate these findings, further theoretical methods have to be used. Only quantum mechanically derived density distributions can reveal orbital participation, which may help to describe the bonding situation within the S-N bonds of the sulfurtriiimide more comprehensively.

As already found in **III** and **IV**, hyperconjugation might affect the tBu groups. C-C bonds, which are oriented at the same side of the non-bonding VSCCs are without exception inclined remarkably towards the lone-pair densities. In addition, for the sulfurtriiimide (**I**) as well as for the sulfurtriiimide (**II**), at least at

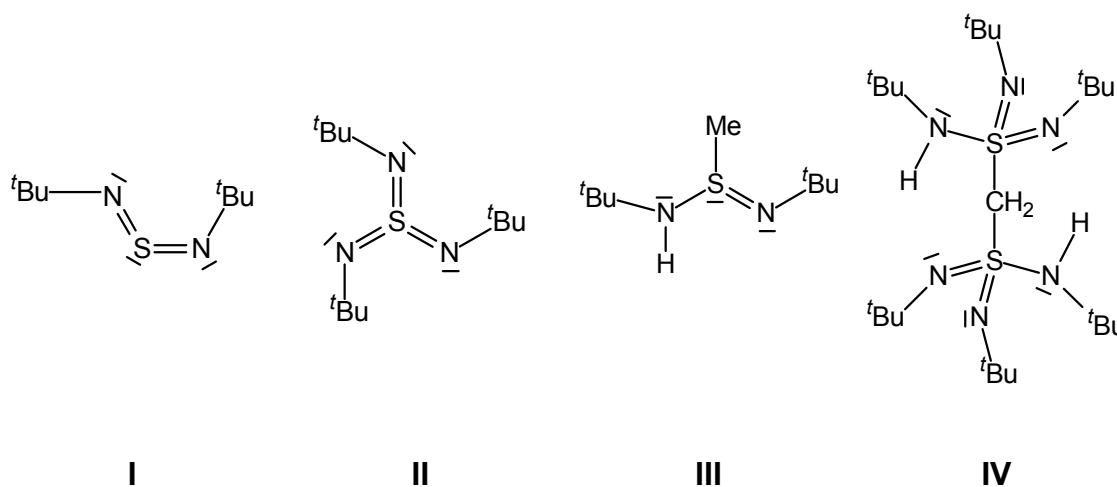
the limit of significance, a reduced density at the BCP was found for the coplanar oriented C–C bonds (C21 in **I** and C11 in **II**). This indicates the presence of negative hyperconjugation effects. In the sulfurtriiimide $\rho(\mathbf{r}_{\text{BCP}})$ of C1–C11 is about $0.04 \text{ e}\text{\AA}^{-3}$ smaller than the values in both C–C bonds, which are oriented away from the nitrogen lone-pair.

The investigations of the Laplacian distributions in the studied compounds are the key to understand the atomic interactions. All other features were affected by limitations, as the model dependence of the deformation densities, the much too rough grading of bond lengths, or the often contradictory properties at the BCPs, like $\rho(\mathbf{r}_{\text{BCP}})$, $-\nabla^2\rho(\mathbf{r}_{\text{BCP}})$, λ_i , and ε_{BCP} . The values calculated from them, as Q , η , and n are all very sensible to correct determination of the position of the BCP, since they all change along the bond path. The angles formed by the nitrogen atoms and the C–C bonds have been identified as a very sensible tool to investigate the gradual variations of the assumed hyperconjugation effects. This proves, that conventional refinements can also reveal sensible information about electronic effects if reliable atomic positions from high-order IAM refinements with high-resolution data are used.

4 Conclusion and Prospects

The main aim of this thesis was to characterise structurally four sulfur-nitrogen compounds in terms of their experimental electron density distribution:

Sulfurdiimide $S(N^tBu)_2$ (I), sulfurtriimide $S(N^tBu)_3$ (II), methyl(diimido)sulfinic acid $H(N^tBu)_2SMe$ (III) and methylene-bis(triimido)sulfonic acid $CH_2\{S(N^tBu)_2-(HN^tBu)\}_2$ (IV).



Standard resonance structures for compounds I-IV.

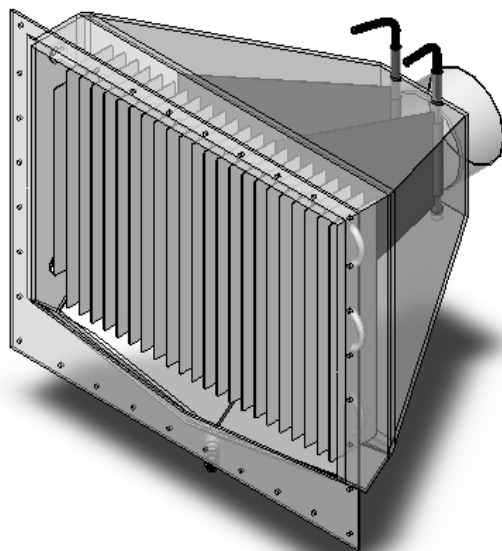
Since I and II were synthesised, the S–N bonds were a point of constant debate. Are there S=N double bonds? If so, the sulfur atoms would not obey the eight-electron-rule. Would the hypervalent sulfur atoms employ the vacant d-orbitals in bonding? This thesis approaches these problems experimentally. The electron density was determined by multipole refinements on high-resolution X-ray data at low temperatures. The refined densities were analysed by means of Bader's theory of 'Atoms in Molecules' to get information about the bonding types (shared/ closed shell), bond strengths, and the extent of polarisation.

Hardware Development

High-resolution experiments still are extremely time consuming due to the decrease of intensity at large Bragg angles. Long exposure times can lead to

icing problems at the single crystal as the atmospheric humidity condenses at the mounting fibre.

Therefore an air drying device was constructed, which can be integrated into the commercial diffractometer cabin. The drying principle bases on freezing out the humidity on cooling fins.



Schematic representation of the air drying device.

Air-tight connection to the diffractometer cabin, the usage of impermeable high-grade steel for radiation protection, the integration of the internal air circulation system, and the facilitated external handling of the cooling unit prevents the crystal from icing even in long-term experiments. It is a safe low-cost extension, which converts an ordinary diffractometer cabin into a dry box suitable for cryo-experiments.

Experimental

All experiments were performed on a Bruker 3-circle goniometer equipped with an APEX-CCD detection system at 100 K. To enable reliable empirical absorption correction, the data were collected up to a resolution $\sin\theta / \lambda$ of at least 1.11 \AA^{-1} ($2\theta_{\text{MoK}\alpha} = 104^\circ$) with high redundancies. Due to the low symmetry (**I** and **II** triclinic, **III** and **IV** monoclinic) and the restricted measurement time, an optimised strategy for the data collection had to be developed.

Structure refinements

All structures were refined with comparable strategies. An optimised refinement strategy was developed in this thesis.

Atomic coordinates and thermal motion parameters of the non-hydrogen atoms were determined by conventional high-order refinement ($\sin\theta/\lambda > 1.0 \text{ \AA}^{-1}$, $2\theta_{\text{MoK}\alpha} > 90.6^\circ$), the values of the hydrogen atoms were adjusted by the exclusive use of the low-order reflections ($\sin\theta/\lambda < 0.5 \text{ \AA}^{-1}$, $2\theta_{\text{MoK}\alpha} < 41.6^\circ$). This led to the starting models for the subsequent multipole refinements along the algorithm of Hansen and Coppens. The number of refinement parameters (multipoles, contraction/expansion parameters) was reduced by similarity and non-crystallographic site symmetry constraints.

The refinements gave excellent residuals. Additional tests (Hirshfeld test, residual densities) showed that all compounds were suitable for a multipole refinement. Shortcomings in the model of the sulfurdiimide (**I**) were reduced by application of an anharmonic motion model based on the Gram-Charlier expansion.

Geometrical properties

A comparison of the S,N bond lengths showed, that the formally equivalent bonds reveal significant differences. The formal S=N double bonds in **I**, **II** and **IV** varied slightly, while the one in **III** was found to be severely elongated.

Wide S–N–C angles, previously exclusively attributed to steric hindrance, now can be traced back to the electrostatic interaction of nitrogen lone-pairs and the electropositive sulfur atom. Furthermore, C–C bond elongation in the ^tBu groups due to hyperconjugation effects might occur.

An analysis of the anisotropic displacement parameters in **II** showed that the SN₃ core is probably disordered relative to the mean SN₃ plane. This leads to a slight pyramidal character of the central sulfur atom.

The crystal packing of the sulfurdiimide (**I**) revealed relatively close distances between two adjacent sulfur atoms, which causes a weak intermolecular S...S interaction. In the solid state H(N^tBu)₂SMe (**III**) adopts a dimeric twisted boat conformation of a S₂N₄H₂ eight-membered ring due to intermolecular hydrogen bonding of the nitrogen-bonded H-atoms to the opposite formally double bonded nitrogen atom.

In $\text{CH}_2\{\text{S}(\text{N}^t\text{Bu})_2(\text{HN}^t\text{Bu})\}_2$ (**IV**) the two $\text{S}(\text{N}^t\text{Bu})_2(\text{HN}^t\text{Bu})$ moieties form two intramolecular hydrogen bonds according to the pattern in **III**.

Charge density distributions

The quality of all refinements was tested by the calculation of residual densities. Exclusively for the solid state structure of sulfurtriamide (**II**) a non-statistical distribution of small residual densities was found. They were identified as a consequence of a 60° rotational disorder relative to an axis through the central sulfur atom along the normal vector of the SN_3 plane. Due to the almost vanishing occupation of the second position, the disorder could not be resolved.

The distributions of the static deformation densities, which already showed the most important electronical features as lone-pairs and bonding densities, were calculated for all compounds. The spatial distributions provided a first impression about the bonding properties. The nitrogen lone-pair densities were found to be inclined towards the electropositive sulfur atoms. In **II**, **III** and **IV** the spatial distributions already suggested sp^3 hybridisation of the nitrogen atoms. In **I** gradual differences between the *E/Z* and *Z/Z* oriented N^tBu groups were visualised. The charge density distribution was analysed along the bond paths, which showed some of the S,N bonds to be considerably bent.

Topological analyses

In the central part of this thesis detailed topological analyses of the electron density distributions were performed. All BCPs and the related electronical properties as the electron density, the negative Laplacian, the eigenvalues of the Hessian matrix, and several values, which can be deduced from these, were calculated. Due to the low number of comparable published compounds, *internal* scaling facilitated by **III** and **IV** led to system-specific ranking of the S–N and S–C bonds in terms of bond type (shared vs. closed shell), bond order, and bond strength.

To quantify bond polarisation, a criterion was developed, which relates shifts in the BCPs to electron transfer from the electropositive to the electronegative bonding partner.

All hydrogen bonds in **III** and **IV**, as well as the intermolecular S...S interaction in the solid state of sulfur diimide (**I**), could be verified by the determination of the related BCPs and non-vanishing densities at the critical points.

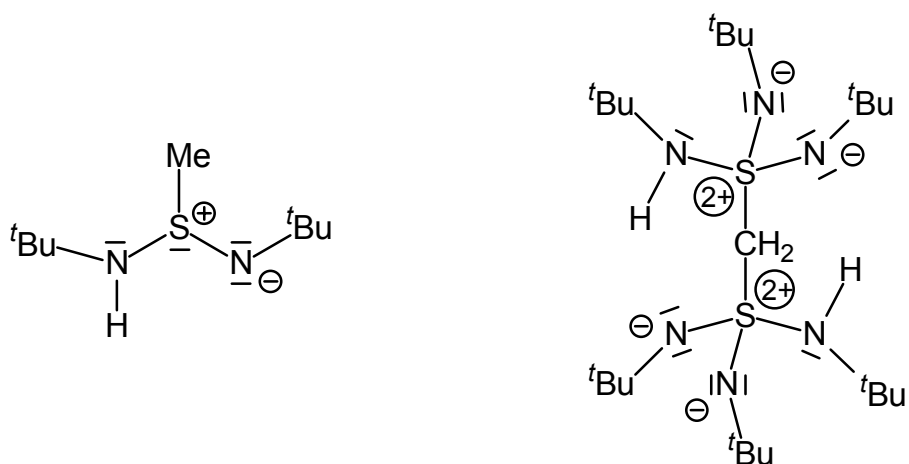
The distributions of the Laplacian $\nabla^2\rho(\mathbf{r})$ were determined for all S–E (E = N, C) bonds because of their fundamental importance for the classification of atomic interactions. Furthermore, the spatial distribution of $-\nabla^2\rho(\mathbf{r})$ with respect to all important bonds was determined around the central sulfur and nitrogen atoms. The analyses led to detailed information about the S,N interactions. Especially the spatial distributions around the nitrogen atoms revealed unexpected properties. Around each of the formally double bonded nitrogen atoms in **II**, **III**, and **IV** doubtlessly two non-bonding VSCCs were found, which were identified as (3,-3) critical points in the distributions of the negative Laplacian. Therefore the formulation of the associated S=N bonds as double bonds could not longer be maintained. The spatial orientation of the lone-pair densities was determined and could be related to the inclination of the ^tBu-groups due to hyperconjugation effects.

A calculation of the reactive surfaces with $\nabla^2\rho(\mathbf{r}) = 0$ revealed possible reaction pathways of nucleophilic attacks to the central sulfur atoms.

Resonance structures

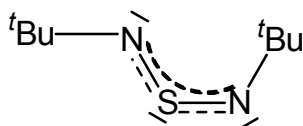
The charge density distributions, the properties at the BCPs and the spatial distributions of the Laplacian required an alternative interpretation of the classical S=N double bonds.

All nitrogen atoms in $\text{H}(\text{N}^t\text{Bu})_2\text{SMe}$ (**III**) as well as in $\text{CH}_2\{\text{S}(\text{N}^t\text{Bu})_2(\text{HN}^t\text{Bu})\}_2$ (**IV**) are predominantly sp^3 hybridised. The S,N bonds should therefore be formulated as S^+-N^- single bonds, strengthened and shortened by electrostatic reinforcement. This leads to increased bonding densities due to back-polarisation of lone-pair densities into the S–N bonds.



In $S(N^tBu)_2$ (**I**) the sp^2 hybridisation of the nitrogen atoms was verified. All topological criteria unearthed the inequity of the formally equivalent $S=N$ double bonds. The differences were assigned to the molecular E/Z conformation in the solid state. Interaction between the in-plane lone-pair density of the nitrogen and the sulfur atom located at the same side, causes the non-bonding charge concentration at the sulfur atom to be dislocated into the second $S-N$ bond.

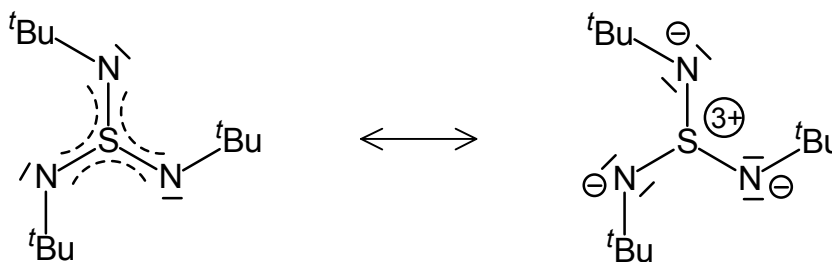
The existence of a delocalised 3-centres-2-electrons system within the planar SN_2 core was assumed to be formed by non-hybridised p-orbitals. An effective delocalisation was found to be possibly disturbed by a weak intermolecular $S\cdots S$ interaction.



Inclination of the tBu groups towards the nitrogen lone-pairs and the significant density reduction in $C-C$ bonds support the assumption of hyperconjugation effects.

The interpretation of the S,N interaction in $S(N^tBu)_3$ (**II**) was not straightforward, since the electron density distribution showed both, indicators for multiple bonding as well as for sp^3 hybridisation of the nitrogen atoms, which verifies the formulation of a S^+-N^- bonding mode. **II** demonstrates the limitation of easy-to-handle concepts as Lewis formulas, hybridisation, or formulation of atomic charges as integers for the description of unusual charge density features. The bonding situation in $S(N^tBu)_3$ was identified as an intermediate state between

that of a delocalised 4-centres-6-electrons system formed by non-hybridised p-orbitals within the planar SN_3 unit and that of a S^+-N^- system.



Since some of the features which revealed multiple bonding characteristics could be assigned to a disorder of the SN_3 core, the S^+-N^- bonding mode contributes most to describe II.

Résumé and prospects

In the course of this thesis, the method of experimental determination of charge density distributions from multipole refinements was established in our group. Strategies for data collection, data processing, and structure refinement were developed and optimised. Therefore future work will be focused on the application of the method, while in the present work the methodical development was emphasised.

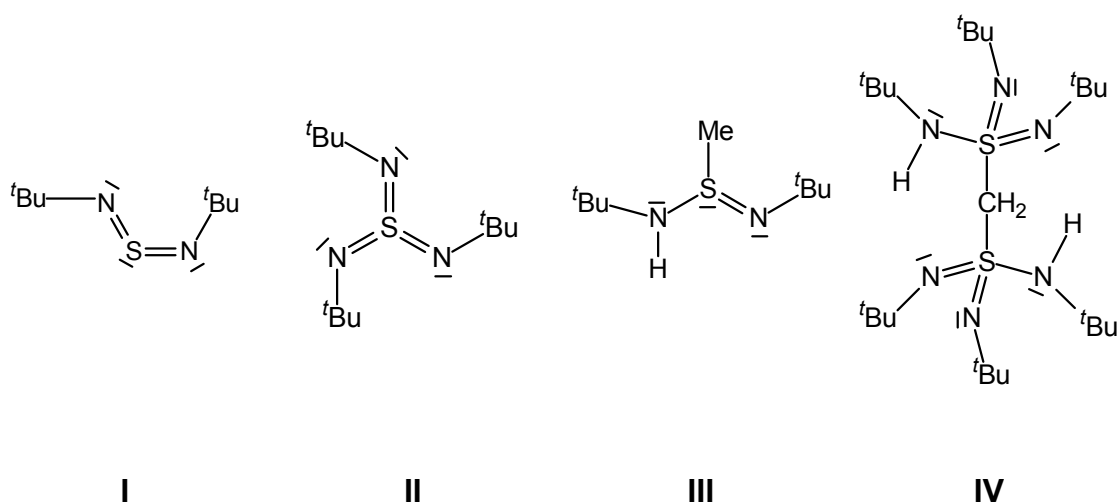
Some of the on first sight contradictory findings during the topological analyses are mainly caused by the characterisation of bonds exclusively from the properties at the BCPs. Here will be the main progress in the near future, since our group is already testing advanced software, which allows the topological analysis along the complete bond path. This, together with the determination of the atomic basins and the integration of charge density within these volumes, will lead to meaningful atomic charges and a much deeper understanding of the nature of bonding.

The complete analyses of experimentally derived electron density distributions from multipole refinements by means of Bader's theory of 'Atoms in molecules' will close the gap between theoretical methods on one side and the experimental approach on the other side by the use of a common standard for comparison.

5 Zusammenfassung

Ziel der vorliegenden Arbeit war die strukturelle Charakterisierung von vier für unsere Arbeitsgruppe grundlegenden molekularen Schwefel-Stickstoffverbindungen, sowie deren Elektronendichteverteilung mit experimentellen Mitteln zu bestimmen:

Schwefeldiimid $S(N^tBu)_2$ (I), Schwefeltriimid $S(N^tBu)_3$ (II), Methyl(diimido)sulfonsäure $H(N^tBu)_2SMe$ (III) und Methylen-bis(triimido)sulfonsäure $CH_2\{S(N^tBu)_2-(HN^tBu)\}_2$ (IV).



Übliche Formulierung der Bindungsverhältnisse in I-IV.

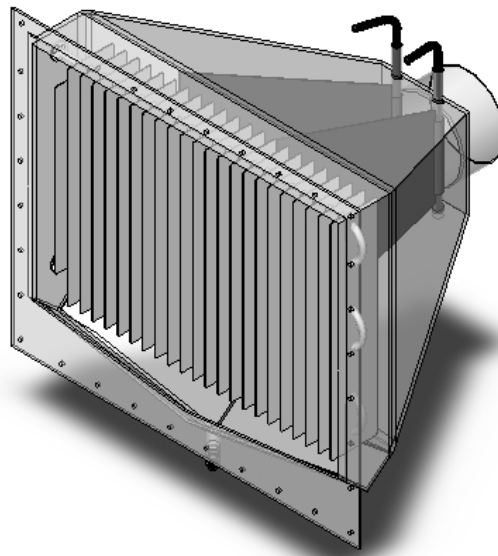
Seit der Synthese von I und II waren die S–N-Bindungsverhältnisse Gegenstand kontroverser Diskussionen. Gibt es S=N Doppelbindungen? Falls ja, erfüllen die zentralen Schwefelatome die Acht-Elektronen-Regel nicht. Werden bei den hypervalenten Schwefelatomen die nicht besetzten d-Orbitale bei der Bindung zu den Stickstoffatomen benutzt? Die vorliegende Arbeit versucht diese Fragen auf experimenteller Basis zu beantworten. Die Ergebnisse wurden aus hochauflösenden Röntgenbeugungsexperimenten an Einkristallen bei tiefen Temperaturen mit anschließender Multipolverfeinerung gewonnen. Die so erhaltenen experimentellen Elektronendichteverteilungen wurden einer topologischen Analyse nach dem Bader-Formalismus der 'Atoms in Molecules' unterzogen. Ziel dieser Analysen war die Charakterisierung der

atomaren Wechselwirkungen innerhalb der Moleküle nach Kriterien wie Bindungstyp (kovalent/ionisch), Bindungsstärke oder Polarisationsgrad.

Geräteentwicklung

Hochauflösende Röntgenbeugungsexperimente sind trotz der Fortschritte in der Detektortechnologie aufgrund der großen Datenmengen immer noch sehr zeitaufwendig. Der Intensitätsabfall bei hohen Beugungswinkeln macht Belichtungszeiten von mehreren Minuten notwendig. Während dieser Zeit bleibt der Kristall unbewegt in Beugungsposition, was zu Vereisung am Kristallort infolge kondensierender Luftfeuchtigkeit im Stickstoff-Kaltgasstrom führen kann.

Dies zu verhindern, wurde eine Trockeneinrichtung konstruiert, die es erlaubt, die Luft innerhalb der Diffraktometerhaube zu trocknen. Das Prinzip der Apparatur besteht im Ausfrieren der Luftfeuchtigkeit an Kühlblechen, die in einem geschlossenen Kreislauf mit einem Kryostaten auf tiefen Temperaturen gehalten werden.



Schematische Darstellung der Trocknungseinheit.

Die Trocknungseinheit ist luftdicht an das Diffraktometergehäuse angeflanscht und durch Verwendung des gleichen Materials (2mm Edelstahlblech) undurchlässig für Röntgenstrahlung. Ein Tangentiallüfter sorgt für den Umwälzbetrieb. Die Optimierung des zu trocknenden Luftstromes sowie das gelegentlich notwendige Abtauen der vereisten Kühlbleche können extern ohne Öffnung der Haube vorgenommen werden. Dies gewährleistet den

Dauerbetrieb während der hochauflösenden Langzeitexperimente. Dauertests zeigten, dass bereits innerhalb von 30 Minuten die relative Feuchte auf ca. ein Drittel des Ausgangswertes reduziert wurde, was in allen bisherigen Experimenten ein Vereisen des Einkristalls verhinderte. Die entwickelte low-cost Apparatur sorgt für eine konstant niedrige Luftfeuchtigkeit in der kommerziellen Diffraktometerhaube und erlaubt langwierige Experimente bei tiefen Temperaturen.

Experimentelles

Alle Datensammlungen erfolgten an einem Bruker 3-Kreisgoniometer mit APEX-CCD Detektor bei 100 K Messtemperatur bis zu einer Auflösung $\sin\theta/\lambda$ von mindestens 1.11 \AA^{-1} ($2\theta_{\text{MoK}\alpha} = 104^\circ$). Bei den Datensammlungen wurde besonderes Augenmerk auf hohe Datenredundanz gelegt, um eine physikalisch sinnvolle empirische Absorptionskorrektur zu ermöglichen. Dies machte die Entwicklung einer speziellen Datensammlungsstrategie nötig, da die Verbindungen in Raumgruppen niedriger Symmetrie (triklin für **I** und **II**, monoklin für **III** und **IV**) kristallisieren.

Strukturverfeinerungen

Um die Verbindungen intern vergleichen zu können, wurden alle Strukturen mit identischer Strategie verfeinert. Diese Verfeinerungsstrategie wurde im Rahmen der vorliegenden Arbeit entwickelt und optimiert.

Zunächst wurden Hochwinkelverfeinerungen ($\sin\theta/\lambda > 1.0 \text{ \AA}^{-1}$, $2\theta_{\text{MoK}\alpha} > 90.6^\circ$) mit einem konventionellen Atommodell durchgeführt, um bestmögliche Startwerte für Koordinaten und anisotrope Auslenkungsparameter der Nichtwasserstoffatome zu bestimmen. Die Parameter der Wasserstoffatome wurden aus den Beugungsdaten bei kleinen Beugungswinkeln gewonnen ($\sin\theta/\lambda < 0.5 \text{ \AA}^{-1}$, $2\theta_{\text{MoK}\alpha} < 41.6^\circ$).

Diese Startmodelle wurden Multipolverfeinerungen nach dem Formalismus von Hansen und Coppens unterzogen. Dabei wurden so viele chemische Informationen (similarity constraints) und nicht-kristallographische Symmetriebeschränkungen wie möglich genutzt. Die Anzahl der Verfeinerungsparameter wurde durch geeignete Wahl eines lokalen Koordinatensystems (symmetry constraints) reduziert.

Alle Verfeinerungen lieferten ausgezeichnete Gütekriterien. Die weiterführenden Tests (Hirshfeld Test, Residualdichten) zeigten, dass mit Ausnahme von $S(N^tBu)_2$ (I) geeignete Startmodelle für die Multipolverfeinerungen erhalten wurden. Im Falle des Schwefeldiimid (I) wurden die Unzulänglichkeiten durch Anwendung eines anharmonischen Schwingungsmodells mittels Gram-Charlier Entwicklung beseitigt.

Geometrische Auswertung

Die geometrischen Strukturparameter aller vier Verbindungen wurden einander gegenübergestellt. Ein Vergleich der S,N Bindungslängen zeigte, dass sich die formal äquivalenten Bindungen signifikant unterscheiden. Während die formalen S=N Doppelbindungsabstände im Schwefeldiimid (I), Schwefeltriimid (II) und in der Methylen-bis(triimido)sulfonsäure $CH_2\{S(N^tBu)_2(HN^tBu)\}_2$ (IV) vergleichbare Werte aufwiesen, zeigte jener in $H(N^tBu)_2SMe$ (III) eine signifikante Verlängerung.

Eine S–N–C Winkelaufweitung, die bislang nur dem qualitativen Konzept der sterischen Hinderung zugeschrieben werden musste, lässt sich jetzt unter anderem durch die Wechselwirkung der freien Elektronenpaare an den Stickstoffatomen mit den elektropositiven Schwefelatomen erklären. Außerdem können die freien Elektronenpaare aufgrund von Hyperkonjugation zu C–C Bindungsverlängerungen in den tBu -Gruppen führen.

Die Analyse der anisotropen Auslenkungsparameter in II lieferte Hinweise auf eine Fehlordnung der SN_3 Einheit. Daraus resultiert eine leicht pyramidale Umgebung für das zentrale Schwefelatom.

Im Schwefeldiimid (I) weist die Anordnung der Moleküle im Festkörper relativ kurze Abstände zwischen zwei benachbarten Schwefelatomen auf. Dies wurde als Indiz für eine intermolekulare S...S Wechselwirkung gewertet.

Im $H(N^tBu)_2SMe$ (III) wird die Festkörperstruktur durch intermolekulare Wasserstoffbrückenbindungen zwischen den stickstoffgebundenen H-Atomen und den formal doppelgebundenen Stickstoffatomen des Nachbarmoleküls determiniert, woraus eine dimere getwistete Bootkonformation eines achtgliedrigen Ringes ($S_2N_4H_2$) resultiert. $CH_2\{S(N^tBu)_2(HN^tBu)\}_2$ (IV) kristallisiert unter Ausbildung intramolekularer Wasserstoffbrückenbindungen zwischen den beiden $S(N^tBu)_2(HN^tBu)$ Einheiten.

Elektronendichteverteilungen

Nach Abschluss der Multipolverfeinerungen wurde für alle Verbindungen die Modellqualität mittels Berechnung der Residualdichteverteilungen getestet. Lediglich in $S(N^tBu)_3$ (**II**) wurden geringe, vom Strukturmodell nicht erfasste Restdichten gefunden, die eine systematische Anordnung aufwiesen. Dies wurde als nicht auflösende Fehlordnung äußerst geringer Besetzung interpretiert. Die Fehlordnung entspricht einer 60° Rotation um einen Vektor durch das Schwefelatom entlang der Flächennormalen der SN_3 Ebene.

Weiterhin wurden die statischen Deformationsdichteverteilungen in allen Verbindungen bestimmt. Diese zeigten, dass die wichtigsten elektronischen Strukturmerkmale modelliert wurden. Die freien Elektronenpaare und Bindungsdichten in den zentralen Einheiten konnten beschrieben werden und ihre Symmetrie lieferte erste Anhaltspunkte für die Klassifizierung der Wechselwirkungen. Die freien Elektronenpaare an den Stickstoffatomen sind durchweg in Richtung des elektropositiven Schwefelatoms orientiert. In **II**, **III** und **IV** lieferte die räumliche Orientierung der freien Elektronenpaare erste Hinweise auf eine mögliche sp^3 -Hybridisierung der Stickstoffatome. In **I** wurden die graduellen Unterschiede zwischen den formal äquivalenten N^tBu -Gruppen durch ihre unterschiedlichen Deformationsdichteverteilungen verdeutlicht.

Des Weiteren wurden die Elektronendichteverteilungen entlang der S–N und S–C Bindungspfade analysiert, was Rückschlüsse auf Spannungen innerhalb der Bindungen erlaubte.

Topologische Analyse der Elektronendichteverteilungen

Im zentralen Teil der Arbeit wurden die verfeinerten Elektronendichteverteilungen aller vier Verbindungen einer ausführlichen topologischen Analyse unterzogen. Dabei wurden zunächst alle bindungskritischen Punkte sowie die Elektronendichte, der Wert der negativen Laplacefunktion und die Eigenwerte der Hessematrix am kritischen Punkt als auch verschiedene Kriterien, die sich aus diesen Werten ableiten, berechnet. Durch interne Skalierung, sowie Einordnung in die wenigen literaturbekannten Beispiele, wurden die S–N und S–C Bindungen nach Typus (kovalent/ionisch), Bindungsordnung und Stärke klassifiziert.

Um Polarisierungseffekte zu quantifizieren, wurde ein Kriterium entwickelt, das über die Lage des kritischen Punktes in den S–N Bindungen einen Quotienten definiert, dessen Wert ein Maß für Polarisation infolge eines Elektronendichtetransfers vom elektropositiveren Schwefelatom zum elektronegativeren Stickstoffatom ist.

Durch die Identifizierung bindungskritischer Punkte in allen Wasserstoffbrückenbindungen konnten diese ebenso zweifelsfrei verifiziert werden wie die intermolekularen S...S Wechselwirkungen im Schwefeldiimid (**I**).

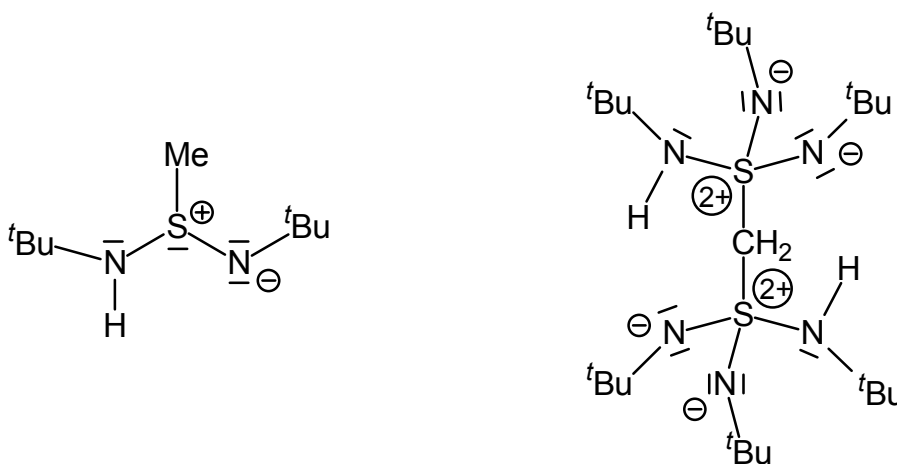
Als wichtigste Größe für die Klassifizierung atomarer Wechselwirkung wurde die Verteilung der Laplacefunktion für alle S–E (E = N, C) Bindungen bestimmt. Sowohl in allen relevanten Ebenenschnitten als auch für die zentralen Einheiten (S, N) in dreidimensionalen Volumina wurde die Laplacefunktion mit hoher Auflösung berechnet. Die Analysen lieferten ein detailliertes Bild der Bindungssituation. Besonders die Laplaceverteilungen um die Stickstoffatome lieferten unerwartete Ergebnisse. Die formal doppelgebundenen Stickstoffatome in **II**, **III** und **IV** zeigten eindeutig zwei nichtbindende Ladungsdichtekonzentrationen in der Valenzschale, die durch die Existenz (3,-3) kritischer Punkte in der negativen Laplacefunktion als freie Elektronenpaare verifiziert werden konnten. Damit konnte die Formulierung dieser S,N Wechselwirkungen als S=N Doppelbindungen nicht länger aufrecht erhalten werden. Die räumliche Orientierung der freien Elektronenpaare wurde bestimmt und konnte mit der schon bei der geometrischen Auswertung beobachteten Neigung der N^tBu-Gruppen korreliert werden.

Über die Bestimmung der reaktiven Oberfläche als Isofläche mit $\nabla^2\rho(\mathbf{r}) = 0$ konnten mögliche Reaktionswege eines Nucleophils zum elektropositiven Zentrum aufgezeigt werden. Auch hier ist man nicht mehr ausschließlich auf qualitative Größenüberlegungen angewiesen.

Schlussfolgerungen

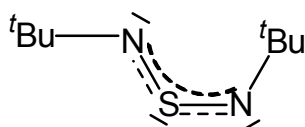
Die Elektronendichteverteilungen, Eigenschaften der kritischen Punkte und vor allem die Verteilungen der Laplacefunktion machten eine alternative Interpretation der S–N Wechselwirkungen gegenüber der Formulierung als S=N Doppelbindungen nötig.

Sowohl für die Methyl(diimido)sulfinsäure $\text{H}(\text{N}^t\text{Bu})_2\text{SMe}$ (III) als auch für die Methylen-bis(triimido)sulfonsäure $\text{CH}_2\{\text{S}(\text{N}^t\text{Bu})_2(\text{HN}^t\text{Bu})\}_2$ (IV) ließen die Topologien ausschließlich die Formulierung sp^3 -hybridisierter Stickstoffatome zu, welche infolge ausgeprägter Polarisierung S^+-N^- Einfachbindungen ausbilden, die durch elektrostatische Rückbindung verstärkt und damit auch verkürzt werden. Die Rückbindung erfolgt durch eine ausgeprägte Orientierung der freien Elektronenpaare an den Stickstoffatomen in Richtung des S–N Bindungsbereiches, was zu erhöhter Elektronendichte in der Bindung und deren Verstärkung führt.



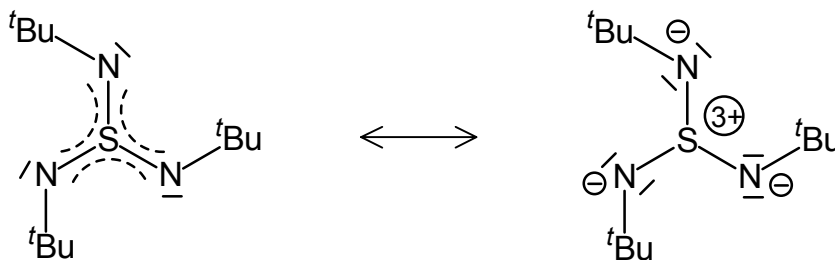
Im Falle des Schwefeldiimides $\text{S}(\text{N}^t\text{Bu})_2$ (I) wurde die sp^2 -Hybridisierung der Stickstoffatome verifiziert. Die weiteren Kriterien lieferten ein zunächst widersprüchliches Bild der beiden formal äquivalenten $\text{S}=\text{N}$ Bindungen. Die Unterschiede in den Bindungen lassen sich durch die unterschiedliche Ausrichtung der freien Elektronenpaare an den Stickstoffatomen erklären. Die Wechselwirkung des freien N-Elektronenpaares auf der gleichen Seite wie das S-Elektronenpaar mit dem elektropositiven Schwefelatom bewirkt seinerseits die Neigung des S-Paares zur zweiten S–N Bindung.

Als zutreffendste Beschreibung der Bindungssituation wurde die Existenz eines delokalisierten 3-Zentren-2-Elektronen Systems in der SN_2 Einheit, gebildet aus nicht-hybridisierten p-Orbitalen, vorgeschlagen. Effektive Delokalisation ist möglicherweise durch intermolekulare $\text{S}\cdots\text{S}$ Wechselwirkungen gestört.



Die ausgeprägte Orientierung der ^tBu Gruppen hin zu den freien Elektronenpaaren der Stickstoffatome und die zumindest im Falle der koplanaren C–C Bindungen signifikante Erniedrigung der Elektronendichte am bindungskritischen Punkt, rechtfertigen die Annahme von Hyperkonjugation.

Die Beschreibung der S,N Wechselwirkung im Schwefeltriimid S(N^tBu)₃ (II) bereitete die größten Schwierigkeiten, da sowohl Anzeichen für eine sp³-Hybridisierung der Stickstoffatome als auch Mehrfachbindungscharakteristika gefunden wurden. Verbindung (II) machte das Versagen einfacher Konzepte wie Lewis Formeln, Hybridisierung oder die Formulierung ganzzahliger Formalladungen deutlich. Die S,N Wechselwirkungen in S(N^tBu)₃ wurden als Übergangssituation zwischen dem Typus des delokalisierten 4-Zentren-6-Elektronen Systems und dem der Ladungstrennung infolge ausgeprägter Polarisierung klassifiziert.



Da einige der Mehrfachbindungsindikatoren auf die nicht aufzulösende Fehlordnung der SN₃ Einheiten zurückgeführt werden können, wird der mesomeren Grenzstruktur mit S⁺–N[–] Bindungsmodus höheres Gewicht bei der korrekten Beschreibung der Bindungsverhältnisse zugemessen.

Resumée und Ausblick

Die vorliegende Arbeit hatte die Einführung der Methode der experimentellen Elektronendichtebestimmung aus hochaufgelösten Röntgenbeugungsdaten mit anschließender Multipolverfeinerung zum Ziel. Das Verfahren sollte an vier beispielhaften Verbindungen getestet werden, deren Bindungssituation innerhalb der S–N Bindungen bisher äußerst widersprüchlich diskutiert wurde.

Die Arbeiten haben dafür gesorgt, dass die hier vorgestellte Methode in unserer Arbeitsgruppe inzwischen wohl etabliert ist. Die Messtechnik und die Datenprozessierung wurden standardisiert. Die anfänglichen Probleme bei Langzeitexperimenten wurden durch die Konstruktion einer

Lufttrocknungseinrichtung behoben, die auf die Bedürfnisse von Datensammlungen an Einkristalldiffraktometern optimiert wurde.

Unterschiedliche Strukturverfeinerungsmodelle wurden überprüft und die Ergebnisse auf physikalische und chemische Plausibilität getestet. Auf diese Weise wurden auch die Verfeinerungsstrategien standardisiert und optimiert, so dass bei zukünftigen Arbeiten die Anwendung und nicht mehr die Entwicklung der Methodik im Vordergrund stehen kann.

Die topologischen Analysen der vier Modellverbindungen lieferten erstaunliche Ergebnisse, die mit weit verbreiteten Konzepten zur Beschreibung molekularer Strukturen nicht in Einklang zu bringen sind. Die vorgeschlagenen Bindungsmodi stehen jedoch im Einklang mit den Erfahrungen der synthetisch arbeitenden Arbeitsgruppenmitglieder.

Einige der auf den ersten Blick widersprüchlichen Befunde in dieser Arbeit liegen in der Beschränkung der topologischen Analysen auf die bindungskritischen Punkte begründet. Hier sind in zukünftigen Arbeiten die größten Fortschritte zu erwarten. Die Kriterien zur Klassifikation von Bindungen werden in Zukunft über den gesamten Bindungspfad berechnet werden, was einen wesentlich tieferen Einblick in die Natur der atomaren Wechselwirkung erlauben wird.

Des Weiteren sind bereits weiterführende Softwarepakete in der Erprobung, die eine noch weitergehende Untersuchung der Elektronendichteverteilungen erlauben. Die genaue Bestimmung der Bader'schen Bassins und die Integration der enthaltenen Elektronendichte wird die Quantifizierung atomarer Ladungen ermöglichen. Die vollständige topologische Analyse nach dem Bader-Formalismus wird die Lücke zwischen Theorie und Experiment schließen. Die Ergebnisse, die beide Methoden unabhängig voneinander liefern, können an einem gemeinsamen Maßstab direkt miteinander verglichen werden.

6 References

- [1] P. Coppens, *X-Ray Charge Densities and Chemical Bonding*, Oxford University Press, Oxford and New York, **1997**.
- [2] T. S. Koritsanszky, P. Coppens, *Chem. Rev.* **2001**, *101*, 1583.
- [3] V. G. Tsirelson, R. P. Ozerov, *Electron Density and Bonding in Crystals*, Inst. of Phys. Publ., Bristol **1996**.
- [4] A. Domenicano, I. Hargittai (eds.), *Accurate Molecular Structure*, Oxford University Press, New York **1992**.
- [5] W. Massa, *Crystal Structure Determination*, Springer Verlag, Berlin **1999**.
- [6] J. A. Ibers, W. C. Hamilton (ed.), *International Tables for X-Ray Crystallography, Vol. 4*, Kynoch Press, Birmingham **1974**.
- [7] a) R. F. Stewart, *J. Chem. Phys.* **1968**, *48*, 4882. b) R. F. Stewart, *J. Chem. Phys.* **1969**, *51*, 4569. c) R. F. Stewart, *J. Chem. Phys.* **1973**, *58*, 1668. d) R. F. Stewart, *J. Chem. Phys. Lett.* **1979**, *65*, 5335.
- [8] F. L. Hirshfeld, *Acta Crystallogr.* **1971**, *B27*, 769.
- [9] B. Dawson, *Acta Crystallogr.* **1964**, *17*, 1990.
- [10] F. L. Hirshfeld, *Acta Crystallogr.* **1975**, *B31*, 162.
- [11] N. K. Hansen, P. Coppens, *Acta Crystallogr.* **1978**, *A34*, 909.
- [12] R. F. Stewart, M. A. Spackman, VALRAY, Department of Chemistry, Carnegie-Mellon Univ., Pittsburg, PA, U.S.A.
- [13] N. K. Hansen, P. Coppens, MOLLY, *Acta Crystallogr.* **1978**, *A34*, 909.
- [14] T. Koritsanszky, S. Howard, P. R. Mallinson, Z. Su, T. Richter, N.K. Hansen, *XD - A Computer Program Package for Multipole Refinement and Analysis of Electron Densities from Diffraction Data*, Berlin **1996**.
- [15] P. Coppens (Project Reporter), *Acta Crystallogr.* **1984**, *A40*, 184.
- [16] A. Martin, A. A. Pinkerton, *Acta Crystallogr.* **1998**, *B54*, 471.
- [17] S. Kuntzinger, S. Dahaoui, N. E. Germani, C. Lecomte, J. A. K. Howard, *Acta Crystallogr.* **1999**, *B55*, 273.

- [18] R. F. Stewart, in *The Application of Charge Density Research to Chemistry and Drug Design*, NATO ASI Series, Series B, Vol. 250, G. A. Jeffrey, J. F. Piniella (eds.), Plenum Press, New York **1991**.
- [19] T. Haumann, R. Boese, S. I. Kozhushkov, A. K. Rauch, A. de Meijere, *Liebigs. Ann./Recl.* **1997**, 2047.
- [20] S. T. Howard, M. B. Hursthouse, C. W. Lehmann, E.A. Poyner, *Acta Crystallogr.* **1995**, B51, 328.
- [21] R. F. W. Bader, *Atoms in Molecules: A Quantum Theory*, Oxford University Press, Oxford, **1990**.
- [22] W. Scherer, P. Sirsch, D. Shorokhov, G. S. McGrady, S. A. Mason, M. C. Gardiner, *Chem. Eur. J.* **2002**, 8, 2323.
- [23] M. Tafipolsky, W. Scherer, K. Öfele, G. Artus, B. Pedersen, W. A. Hermann, G. S. McGrady, *J. Am. Chem. Soc.* **2002**, 124, 5865.
- [24] R. Flaig, T. Koritzanszky, B. Dittrich, A. Wagner, P. Luger, *J. Am. Chem. Soc.* **2002**, 124, 3407.
- [25] T. S. Hwang, Y. Wang, *J. Phys. Chem.* **1998**, 102, 3726.
- [26] R. V. Williams, V. R. Gadhil, P. Luger, T. Koritsanszky, M. Weber, *J. Org. Chem.* **1999**, 64, 1180.
- [27] W. Scherer, M. Spiegler, B. Pedersen, M. Tafipolsky, W. Hieringer, B. Reinhard, A. J. Downs, G. S. McGrady, *J. Chem. Soc. Chem. Commun.* **2000**, 635.
- [28] T. Koritsanzky, R. Flaig, D. Zobel, H. G. Krane, W. Morgenroth, P. Luger, *Science* **1998**, 279, 356.
- [29] C. Lecomte, at 19th Europ. Crystallogr. Meeting, Nancy **2000**.
- [30] P. Macchi, D. M. Proserpio, A. Sironi, *J. Am. Chem. Soc.* **1998**, 120, 1447.
- [31] P. Macchi, D. M. Proserpio, A. Sironi, *J. Am. Chem. Soc.* **1998**, 120, 13429.
- [32] P. Macchi, A. J. Schultz, F. K. Larsen, B. B. Iversen, *J. Phys. Chem.* **2001**, A105, 9231.
- [33] M. A. Spackman, *Chem. Rev.* **1992**, 92, 1769.

- [34] M. A. Spackman, P. G. Byrom, M. Alfredson, K. Hermansson, *Acta Crystallogr.* **1999**, A55, 30.
- [35] M. O'Keeffe, J. C. H. Spence, *Acta Crystallogr.* **1994**, A50, 33.
- [36] A. Fkyerat, A. Guelzim, F. Baert, J. Zyss, A. Perigaud, *Phys. Rev.* **1996**, B53, 16236.
- [37] a) R. Fleischer, S. Freitag, F. Pauer, D. Stalke, *Angew. Chem.* **1996**, 108, 208; *Angew. Chem. Int. Ed. Engl.* **1996**, 35, 204; b) R. Fleischer, A. Rothenberger, D. Stalke, *Angew. Chem.* **1997**, 109, 1140; *Angew. Chem. Int. Ed. Engl.* **1997**, 36, 1105; c) R. Fleischer, S. Freitag, D. Stalke, *J. Chem. Soc. Dalton Trans.* **1998**, 193; d) R. Fleischer, D. Stalke, *Organometallics* **1998**, 17, 832; e) R. Fleischer, D. Stalke, *J. Chem. Soc. Chem. Commun.* **1998**, 343; f) R. Fleischer, D. Stalke, *J. Organomet. Chem.* **1998**, 550, 173; g) D. Ilge, D. S. Wright, D. Stalke, *Chem. Eur. J.* **1998**, 4, 2275; h) B. Walfort, L. Lameyer, W. Weiss, R. Herbst-Irmer, R. Bertermann, J. Rocha, D. Stalke, *Chem. Eur. J.* **2001**, 7, 1417; i) B. Walfort, S. K. Pandey, D. Stalke, *J. Chem. Soc. Chem. Commun.* **2001**, 1640.
- [38] a) B. Walfort, R. Bertermann, D. Stalke, *Chem. Eur. J.* **2001**, 7, 1424; b) B. Walfort, D. Stalke, *Angew. Chem.* **2001**, 113, 3965; *Angew. Chem. Int. Ed. Engl.* **2001**, 40, 3846.
- [39] M. M. Labes, P. Love, L. F. Nichols, *Chem. Rev.* **1979**, 79, 1.
- [40] R. Fleischer, Thesis, Universität Würzburg **1997**.
- [41] a) R. Mews, P. J. Watson, E. Lork, *Coord. Chem. Rev.* **1996**, 158, 233; b) R. Fleischer, D. Stalke, *Coord. Chem. Rev.* **1998**, 176, 431; c) D. Stalke, *Proc. Indian Acad. Sci.* **2000**, 112, 155.
- [42] B. Walfort, Thesis, Universität Würzburg **2001**.
- [43] R. Fleischer, B. Walfort, A. Gburek, P. Scholz, W. Kiefer, D. Stalke, *Chem. Eur. J.* **1998**, 4, 2259.
- [44] B. Walfort, A. P. Leedham, C. A. Russell, D. Stalke, *Inorg. Chem.* **2001**, 40, 5668.
- [45] M. Goehring, G. Weis, *Angew. Chem.* **1956**, 68, 678.
- [46] O. Glemser, J. Wegener, *Angew. Chem.* **1970**, 82, 324; *Angew. Chem. Int. Ed. Engl.* **1970**, 9, 309.

- [47] M. Herberhold, S. Gerstmann, W. Milius, B. Wrackmeyer, H. Borrmann, *Phosphorus, Sulfur, Silicon, Relat. Elem.* **1996**, *112*, 261.
- [48] S. Pohl, B. Krebs, U. Seyer, G. Henkel, *Chem. Ber.* **1979**, *112*, 1751.
- [49] I. Mayer, *J. Mol. Struct. (Theochem.)* **1987**, *149*, 81.
- [50] a) W. Kutzelnigg, *Angew. Chem.* **1984**, *96*, 262; *Angew. Chem. Int. Ed. Engl.* **1984**, *23*, 272; b) A. E. Reed, F. Weinhold, *J. Am. Chem. Soc.* **1986**, *108*, 3586; c) D. A. Bors, A. Streitwieser, *J. Am. Chem. Soc.* **1986**, *108*, 1397; d) A. E. Reed, P. v. R. Schleyer, *J. Am. Chem. Soc.* **1990**, *112*, 1434; e) U. Salzner, P. v. R. Schleyer, *J. Am. Chem. Soc.* **1993**, *115*, 10231; f) T. Stefan, R. Janoschek, *J. Mol. Model.* **2000**, *6*, 282.
- [51] D. W. J. Cruickshank, M. Eisenstein, *J. Mol. Struct.* **1985**, *130*, 143.
- [52] D. W. J. Cruickshank, *J. Mol. Struct.* **1985**, *130*, 177.
- [53] J. Cioslowski, P. R. Surján, *J. Mol. Struct.* **1992**, *255*, 9.
- [54] a) R. E. Rundle, *J. Am. Chem. Soc.* **1947**, *69*, 1327; b) R. E. Rundle, *J. Chem. Phys.* **1949**, *17*, 671; c) R. E. Rundle, *J. Phys. Chem.* **1957**, *61*, 45.
- [55] T.H. Tang, R. F. W. Bader, P. J. MacDougall, *Inorg. Chem.* **1985**, *24*, 2047.
- [56] D. Leusser, B. Walfort, D. Stalke, *Angew. Chem.* **2002**, *114*, 2183; *Angew. Chem. Int. Ed. Engl.* **2002**, *41*, 2079.
- [57] R. Rudman, *Low Temperature X-ray Diffraction: Apparatus and Techniques*, Plenum Press, New York **1976**.
- [58] M. Veith, W. Frank, *Chem. Rev.* **1988**, *88*, 81.
- [59] P. Luger, *S. Afr. J. Chem.* **1989**, *42*, 127.
- [60] D. Stalke, *Chem. Soc. Rev.* **1998**, *27*, 171.
- [61] T. Kottke, R. J. Lagow, D. Stalke, *J. Appl. Cryst.* **1996**, *29*, 465.
- [62] A. P. Perov, *Prib. Tekh. Eksp.* **1984**, *3*, 226.
- [63] D. Zobel, P. Luger, W. Dreißig, T. Koritsanszky, *Acta Crystallogr.* **1992**, *B48*, 837.
- [64] T. Kottke, D. Stalke, *J. Appl. Cryst.* **1993**, *26*, 615.

- [65] A. Heine, D. Stalke, *Angew. Chem.* **1992**, *104*, 941; *Angew. Chem. Int. Ed. Engl.* **1992**, *31*, 854.
- [66] A. Heine, D. Stalke, *Angew. Chem.* **1993**, *105*, 90; *Angew. Chem. Int. Ed. Engl.* **1993**, *32*, 121.
- [67] R. Fleischer, S. Freitag, F. Pauer, D. Stalke, *Angew. Chem.* **1996**, *108*, 208; *Angew. Chem. Int. Ed. Engl.* **1996**, *35*, 204.
- [68] T. Koritsánszky, R. Flaig, D. Zobel, H.-G. Krane, W. Morgenroth, P. Luger, *Science* **1998**, *279*, 356.
- [69] R. Flaig, T. Koritsánszky, R. Soyka, L. Häming, P. Luger, *Angew. Chem.* **2001**, *135*, 368; *Angew. Chem. Int. Ed. Engl.* **2001**, *40*, 355.
- [70] R. Flaig, T. Koritsánszky, B. Dittrich, A. Wagner, P. Luger, *J. Am. Chem. Soc.* **2002**, *124*, 3407.
- [71] H. Hope, *Experimental Organometallic Chemistry*, ACS Symposium Series No. 357, Washington, DC: American Chemical Society.
- [72] H. Hope, *Acta Crystallogr.* **1987**, *B44*, 22.
- [73] Ultra-Kryomat, Control Panel: RUL 80, MGW, Lauda.
- [74] M. Born, *Z. Physik* **1926**, *38*, 803.
- [75] C. A. Coulson, M. W. Thomas, *Acta Crystallogr.* **1971**, *B27*, 1354.
- [76] C.K. Johnson, H. A. Levy, *International Tables for X-Ray Crystallography, Vol. 4*, Kynoch Press, Birmingham **1974**.
- [77] G. A. Jeffrey, D. W. J. Cruickshank, *Quart. Rev. Chem. Soc. London*, **1953**, *7*, 335.
- [78] a) P. Coppens, M. S. Lehmann, *Acta Cryst.* **1976**, *B32*, 1777; b) M. S. Lehmann, P. Coppens, *Acta Chem. Scand.* **1977**, *A31*, 530.
- [79] R. F. Stewart, *Israel J. Chem.* **1977**, *16*, 124.
- [80] J. D. Dunitz, W.B. Schweizer, P. Seiler, *Helv. Chim. Acta* **1983**, *66*, 123.
- [81] S. Dahaoui, V. Pichon-Pesme, J. A. K. Howard, C. Lecomte, *J. Phys. Chem.* **1999**, *A103*, 6240.
- [82] V. G. Tsirelson, P. F. Zou, T. H. Tang, R. F. W. Bader, *Acta Crystallogr.* **1995**, *A51*, 143.

- [83] K. L. Geisinger, M. A. Spackman, G. V. Gibbs, *J. Phys. Chem.* **1987**, *91*, 3237.
- [84] J. W. Downs, *J. Phys. Chem.* **1995**, *99*, 6849.
- [85] G. M. Sheldrick, private communication.
- [86] Bruker Nonius Inc., *SAINT-NT: Program for Integration of Diffraction Data from Area Detectors*, Madison WI **2000**.
- [87] W. Kabsch, *J. Appl. Cryst.* **1988**, *21*, 916.
- [88] Bruker Nonius Inc., *SMART-NT: Program for Diffractometer Controlling*, Madison WI **2000**.
- [89] D. Leusser, *Diplomarbeit*, Universität Würzburg, **1997**.
- [90] A. L. Spek, *Acta Crystallogr.* **1990**, *A46*, C-34.
- [91] B. Blessing, *Acta Crystallogr.* **1995**, *A51*, 33.
- [92] Bruker Nonius Inc., *SHELXTL-97*, Madison, WI, **1997**.
- [93] D. Leusser, *BATCH - Program for Batch Number Assignment*, Universität Würzburg, **2000**.
- [94] G. M. Sheldrick, *Acta Crystallogr.* **1990**, *A46*, 467.
- [95] G. M. Sheldrick, *SHELXL-97 – Program for Structure Refinement*, Universität Göttingen, **1997**.
- [96] P. Coppens, in *Neutron Diffraction*, H. Dachs (ed.), *Top. Curr. Phys.* **6**, Springer Verlag, Berlin, **1978**.
- [97] F. A. Allen, *Acta Crystallogr.* **1986**, *B42*, 515.
- [98] P. Rademacher, *Strukturen organischer Moleküle*, VCH, Weinheim / New York, **1987**.
- [99] Cambridge Structural Database, Version 5.23, April **2002**.
- [100] J. Emsley, *The Elements*, de Gruyter, New York, **1994**.
- [101] M. Björgvinsson, H. W. Roesky, F. Pauer, D. Stalke, G. M. Sheldrick, *Inorg. Chem.* **1990**, *26*, 5140.
- [102] F. L. Hirshfeld, *Acta Crystallogr.* **1976**, *A32*, 239.

- [103] a) J. Emsley, *Chem. Soc. Rev.* **1980**, 9, 91; b) G. R. Desiraju, T. Steiner, *The Weak Hydrogen Bond*, Oxford University Press, Oxford, **2001**. c) T. Steiner, *Angew. Chem.* **2002**, 114, 50; *Angew. Chem. Int. Ed. Engl.* **2002**, 41, 48.
- [104] R. Fleischer, B. Walfort, A. Gbureck, P. Scholz, W. Kiefer, D. Stalke, *Chem. Eur. J.* **1998**, 4, 2266.
- [105] U. Salzner, P. v. R. Schleyer, *J. Am. Chem. Soc.* **1993**, 115, 10231.
- [106] N. K. Hansen, P. Coppens, *Acta Crystallogr.* **1978**, A34, 909.
- [107] E. Espinosa, E. Molins, C. Lecomte, *Phys. Rev.* **1997**, B56, 1820.
- [108] S. Pillet, M. Souhassou, Y. Pontillon, A. Caneschi, D. Gatteschi, C. Lecomte, *New J. Chem.* **2001**, 25, 131.
- [109] E. Clementi, C. Roetti, *At. Data Nucl. Data Tables* **1974**, 14, 177.
- [110] A. Volkov, Y. A. Abramov, P. Coppens, *Acta Crystallogr.* **2000**, A57, 272.
- [111] E. Espinosa, C. Lecomte, E. Molins, S. Ventemillas, A. Cousson, W. Paulus, *Acta Crystallogr.* **1996**, B52, 519.
- [112] R. F. Stewart, *The Application of Charge Density Research to Chemistry and Drug Design*, G. A. Jeffrey, F. F. Piniella (eds.), *Nato ASI Series B* 250, Plenum Press, New York and London, **1990**.
- [113] R. Flaig, T. Koritsanszky, D. Zobel, P. Luger, *J. Am. Chem. Soc.* **1998**, 120, 2227.
- [114] R. Flaig, T. Koritsanszky, B. Dittrich, A. Wagner, P. Luger, *J. Am. Chem. Soc.* **2002**, 124, 3407.
- [115] C. Gatti, R. Bianchi, R. Destro, F. Merati, *J. Mol. Struct. (Theochem.)* **1992**, 255, 409.
- [116] C. Flensburg, S. Larsen, R. F. Stewart, *J. Phys. Chem.* **1995**, 99, 10130.
- [117] A. S. Brown, V.H. Smith Jr., *J. Chem. Phys.* **1993**, 99, 1837.
- [118] K. L. McCormack, P. R. Mallinson, B. C. Webster, D. S. Yufit, *J. Chem. Soc. Faraday Trans.* **1996**, 92, 1709.
- [119] T.-H. Tang, R. F. W. Bader, P. J. MacDougall, *Inorg. Chem.* **1985**, 24, 2047.
- [120] M. L. DeLucia, P. Coppens, *Inorg. Chem.* **1978**, 17, 2336.

- [121] S. Pillet, M. Souhassou, Y. Pontillon, A. Caneschi, D. Gatteschi, C. Lecomte, *New J. Chem.* **2001**, 25, 131.
- [122] P. Coppens, *Acta Crystallogr.* **1998**, A54, 779.
- [123] R. F. W. Bader, H. Essen, *J. Chem. Phys.* **1984**, 80, 1943.
- [124] E. Espinosa, M. Souhassou, H. Lachekar, C. Lecomte, *Acta Crystallogr.* **1999**, B55, 563.
- [125] a) R. S. Gopalan, G. U. Kulkarni, E. Subramanian, S. Renganayaki, *J. Mol. Struct.* **2000**, 534, 169; b) G. U. Kulkarni, R. S. Gopalan, C. N. R. Rao, *J. Mol. Struct. (Theochem.)* **2000**, 500, 339.
- [126] A. W. Marsman, C. A. van Walree, R. W. A. Havenith, L. W. Jenneskens, M. Lutz, A. L. Spek, E. T. G. Lutz, J. H. van der Maas, *J. Chem. Soc. Perkin Trans. 2* **2000**, 501.
- [127] M. J. Almond, G. A. Forsyth, D. A. Rice, A. J. Downs, T. L. Jeffery, K. Hagen, *Polyhedron* **1989**, 8, 2631.
- [128] M. A. Robb, J. R. Cheeseman, V. G. Zakrzewski, J. A. Montgomery, Jr., R. E. Stratmann, J. C. Burant, S. Dapprich, J. M. Millam, A. D. Daniels, K. N. Kudin, M. C. Strain, O. Farkas, J. Tomasi, V. Barone, M. Cossi, R. Cammi, B. Mennucci, C. Pomelli, C. Adamo, S. Clifford, J. Ochterski, G. A. Petersson, P. Y. Ayala, Q. Cui, K. Morokuma, D. K. Malick, A. D. Rabuck, K. Raghavachari, J. B. Foresman, J. Cioslowski, J. V. Ortiz, A. G. Baboul, B. B. Stefanov, G. Liu, A. Liashenko, P. Piskorz, I. Komaromi, R. Gomperts, R. L. Martin, D. J. Fox, T. Keith, M. A. Al-Laham, C. Y. Peng, A. Nanayakkara, C. Gonzalez, M. Challacombe, P. M. W. Gill, B. Johnson, W. Chen, M. W. Wong, J. L. Andres, C. Gonzalez, M. Head-Gordon, E. S. Replogle, and J. A. Pople, *GAUSSIAN 98*, Gaussian Inc., Pittsburgh PA, **1998**.
- [129] a) E.D. Glendening, F. Weinhold, *J. Comput. Chem.* **1998**, 19, 593; b) E.D. ^[1] Glendening, F. Weinhold, *J. Comput. Chem.* **1998**, 19, 610; c) E.D. Glendening, J. K. Badenhoop, F. Weinhold, *J. Comput. Chem.* **1998**, 19, 628.
- [130] D. Ilge, private communication.

Publikationen

1. H. Ihmels, D. Leusser, M. Pfeiffer, D. Stalke, „Regioselective Photodimerization of 9-Substituted Acridizinium Salts in the Solid State“, *J. Org. Chem.* **1999**, *64*, 5715.
2. M. Pfeiffer, F. Baier, T. Stey, D. Leusser, D. Stalke, B. Engels, D. Moigno, W. Kiefer, „Di(2-pyridyl)-Amides and -Phosphides: Syntheses, Reactivity, Structures, Raman-Experiments and Calculations“, *J. Mol. Model.* **2000**, *6*, 299.
3. H. Ihmels, M. Pfeiffer, D. Leusser, D. Stalke, „Solid-State Photolysis of Anthracene-Linked Ammonium Salts: The Search for Topochemical Anthracene Photodimerizations“, *Tetrahedron* **2000**, *56*, 6867.
4. A. Steiner, G. T. Lawson, B. Walfort, D. Leusser, D. Stalke, „[(THF)₆Ba₆(dmpz)₈{(OSiMe₂)₂O}₂] (dmpz = 3,5-dimethylpyrazolate): A Molecule with Six Barium Cations in a Plane Capped by Two Siloxane Dianions and Framed by Eight dmpz Anions“, *J. Chem. Soc. Dalton Trans.* **2001**, *3*, 219.
5. H. Ihmels, D. Leusser, M. Pfeiffer, D. Stalke, „Solid-State Photodimerization of 9-Substituted Acridizinium Salts - Selectivity by Directional π -Stacking“, *Mol. Cryst. and Liq. Cryst.* **2001**, *356*, 433.
6. W. Adam, S. G. Bosio, B. Fröhling, D. Leusser, D. Stalke, „Unusual Sulfur Chemistry in the Thermal Reaction of Sultene and Thiophene Endoperoxide Sulfur Donors with Cyclic Alkynes: Reversible Formation of a Persistent Thiirenium Ion and Trapping of a Thiirene by [4+ 2] Cycloaddition“, *J. Am. Chem. Soc.* **2002**, *124*, 8316.
7. D. Leusser, B. Walfort, D. Stalke, „Charge-Density Study of Methane Di(triimido)sulfonic Acid H₂C{S(N^tBu)₂(NH^tBu)}₂ – the NR Analogue of H₂C{S(O)₂(OH)}₂“, *Angew. Chem.* **2002**, *114*, 2183; *Angew. Chem. Int. Ed.* **2002**, *41*, 2079.
8. H. Ihmels, C. J. Mohrschladt, A. Schmitt, M. Bressanini, D. Leusser, D. Stalke, „Highly Regioselective Solid-State Photodimerization of Naphtoquinolizinium Salts“, *Eur. J. Org. Chem.* **2002**, 2624.

Posterpräsentationen

1. D. Leusser, D. Stalke, „S=N vs. S⁺–N[–]: Charge Density Distribution in S(N^tBu)₃ from Low-T CCD Diffraction Experiments – Data Dependent Results“, 19th ECM **2000**, Nancy, Fr.
2. K. Strohfeld, D. Leusser, D. Schildbach, D. Stalke, C. Strohmam, „Crystal Structure of a Mixed Aggregate of Four Different Lithiated Compounds“, AGICHEM Symposium **2002**, LMU München.

Lebenslauf

Persönliche Daten:

Name: Dirk Leußer
Geburtsdatum: 21. März 1966
Geburtsort: Würzburg
Familienstand: ledig

Schulbildung:

1972 – 1973 Grundschule Coburg
1973 – 1977 Grund- und Hauptschule Veitshöchheim
1977 – 1987 Siebold-Gymnasium Würzburg, Abschluss: Abitur

Studium:

10/87 – 10/89 Studium der Volkswirtschaftslehre (Diplom), Universität Würzburg
10/89 – 11/97 Studium der Physik (Diplom), Universität Würzburg
09/96 – 09/97 Diplomarbeit im Arbeitskreis von Prof. Dr. D. Stalke am Institut für Anorganische Chemie der Universität Würzburg mit dem Titel:
Vergleichende Elektronendichteuntersuchungen an [2,2]-Paracyclophan durch hochauflösende Röntgenbeugung bei tiefen Temperaturen.
Betreuer innerhalb des Instituts für Physik und Astronomie: Prof. Dr. W. Steinrück, Experimentelle Physik
11/97 Studienabschluss: Diplom, Gesamtnote: „sehr gut“
seit 01/98 Arbeiten an der Dissertation mit dem Titel:
S=N *versus* S⁺-N⁻ – An Experimental Charge Density Study im Arbeitskreis von Prof. Dr. D. Stalke am Institut für Anorganische Chemie der Universität Würzburg

